Università degli Studi di Pavia

Dipartimento di Scienze della Terra e dell'Ambiente

SCUOLA DI ALTA FORMAZIONE DOTTORALE

MACRO-AREA SCIENZE E TECNOLOGIE

DOTTORATO DI RICERCA IN SCIENZE DELLA TERRA E DELL'AMBIENTE

Lorenzo Scandolo

Thermal expansion of mantle mineral inclusions in diamonds

Anno Accademico 2015-2016

Ciclo XXIX

Coordinatore

Prof. Annamaria Picco

Tutore:

Prof. M. Chiara Domeneghetti

Co-tutore:

Dr. Matteo Alvaro

Alla mia famiglia che mi è stata sempre vicina

Table of Contents

Preface

The aim of this PhD thesis is to provide new constraints on the thermoelastic behavior (e.g. compressibility and thermal expansion) of some minerals phases frequently occurring as inclusions in diamonds (e.g. pyroxenes and garnets, see Stachel and Harris 2008 for a review). Knowledge of the thermoelastic properties of minerals is a fundamental requirement to enable the estimate of the entrapment pressures (i.e. depth of formation) for host-inclusion pairs using elastic geobarometry (Angel et al., 2014a,b; 2015). As it will be shown in the present study precision and accuracy in determining the thermoelastic coefficients can strongly affect the results in terms of calculated entrapment pressures. However, even if measurements at simultaneous high-P and T are nowadays routine experiments, their agreement with independent P and T determination is still poor, mostly because of the uncertainties arising from the lack of suitable standard for simultaneous calibrations at high-P,T. The new measurements performed on pyroxenes and garnets will be used here also to illustrate the importance of using consistent and homogeneous compressibility and thermal expansion dataset determined using the same measurements protocols on a single sample. This approach allows us to obtain a complete set of thermoelastic coefficients to reliably describe the behavior of a crystalline phase at high-P and T.

This PhD thesis is organized into six chapters and one appendix that are briefly described here below.

Chapter 1. Introduces the readers to the basic topics discussed in the thesis with the aim of giving the fundamental concepts for understanding the discussion contained in the following four chapters that correspond to four scientific articles published, accepted for publication or submitted to international peer-reviewed journals. In the Introduction section, the objectives of the present Ph.D thesis are illustrated with particular attention to the description of their general context pointing out at the broad implications connected to the results. The crucial questions regarding the provenance and the mechanism of formation of diamonds are still under debate in the scientific community. Key questions such as "what is the pressure and temperature of formation for diamond? What is the mechanism/process of formation for diamond?" are still seeking for an answer. In this thesis I will use mineral phases frequently occurring as inclusions in diamonds as an example to show the reader how their investigation can provide clues to address the abovementioned key questions. I will describe the basis of the new elastic thermobarometry approach, comparing advantages and the limitations with respect to the classic 'chemical' thermobarometric approach. Then I will focus on theoretical development of the elastic geobarometry and the consequent need for thermoelastic properties to be measured in a consistent, accurate and precise manner. Afterward,

I will describe technique that allows us to extrapolate information from these minerals using a non-destructive approach that is currently still under intense development immediately followed by the detailed explanation of the results of the recent improvement of thermal expansion measurements and their use for elastic geobarometry.

Chapter 2 (manuscript #1). Is a paper entitled: *"A new micro-furnace for in situ high temperature single crystal diffraction measurements"* by M. Alvaro, R. J. Angel, C. Marciano, S. Milani, L. Scandolo, M. L. Mazzucchelli, G. Zaffiro, G. Rustioni, M. Briccola, M. C. Domeneghetti and F. Nestola. The manuscript contains a description of a new micro-furnace developed by our research group here at the Department of Earth and Environmental Sciences at the University of Pavia. The furnace is equipped with an H-shaped resistance heater and a cooling system that allows to perform in situ single-crystal X-ray diffraction experiments at high temperature up to 1200K. The combined use of a K-type small diameter thermocouple together with mineral phases with well characterized lattice expansion (e.g. pure Si and SiO_2 quartz) allowed us to determine a very accurate temperature calibration (σ of about 5K) from room temperature to about 1273 K. Furthermore, we could evaluate thermal gradients and stability while performing a simulated experiment. The main advantages, limitations and important considerations for the use of this micro-furnace to perform in situ high-temperature diffraction measurements are discussed. The paper was submitted to the international peer-reviewed journal "*Journal of Applied Crystallography"* and published on December 2015.

Chapter 3 (manuscript #2). Is the paper titled: "*Thermal expansion behavior of orthopyroxenes: the role of the Fe-Mn substitution", by* L. Scandolo, M. L. Mazzucchelli, M. Alvaro, F. Nestola, F. Pandolfo and M. C. Domeneghetti. It is a comparison between the thermal expansion behavior from room T to 1073 K of two *Pbca* orthopyroxene samples, donpeacorite ($Mn_{0.54}Ca_{0.03}Mg_{1.43}Si_2O_6$, DP N.1) and enstatite ($Fe_{0.54}Ca_{0.03}Mg_{1.43}Si_2O_6$, B22 N.60). The investigation has been performed by single-crystal X-ray diffraction. Data demonstrated that there is no difference in the volume thermal expansion coefficient as a function of composition. For what concerns the lattice parameters, the expansion along the *b* direction is nearly identical for both samples whereas slight differences have been found along *a* and *c* lattice directions. The negligible effect of the Fe-Mn substitution on the bulk thermal expansion allows a strong simplification when elastic geobarometry is applied to orthopyroxenes. In fact, even though the compressibility effect is still not known, it is certain that the nearly identical thermal expansion coefficients will not affect the calculated entrapment pressure (P_e). This paper was submitted to the international peer-reviewed journal "*Mineralogical Magazine"* and published on February 2015.

Chapter 4 (manuscript #3). Is the paper with title: "*Elasticity of grossular garnet at high-pressure and temperature"* by S. Milani, R.J. Angel, L. Scandolo, M.L. Mazzucchelli, T. Boffa-Ballaran, S. Klemme, M.C. Domeneghetti, R. Miletich, K. Scheidl, M. Derzsi1, K. Tokár, M. Prencipe, M. Alvaro, F. Nestola. In the manuscript the elastic behaviour of synthetic single crystals of grossular garnet ($Ca_3Al_2Si_3O_{12}$) has been studied *in situ* as a function of pressure and temperature separately. The same data collection protocol has been adopted to collect both the pressure-volume (*P*-*V*) and temperature-volume (*T*-*V*) datasets in order to make the measurements consistent with one another. The consistency between the two datasets allows simultaneous fitting to a single pressure-volume-temperature equation of state (EoS). Validation of the results has been carried out with a new fitting utility implemented in the latest version of the program EoSFit7c. The new utility performs fully weighted *simultaneous* fits of the *P*-*V*-*T and P*-*K*-*T* data using a thermal pressure Equation of State combined with any PV EoS. Simultaneous refinement of our *P*-*V*-*T* data combined with that of K^T as a function of *T* allowed us to produce a single *P*-*V*-*T*-K^T equation of state with the following coefficients: V_0 = 1664.46(5) $Å^3$, K_{T0} = 166.57(17) GPa and $K`$ = 4.96(7), $\alpha_{(300K,\ 1bar)} = 2.09(2)*10^{-5}\ K^{-1}$ with a refined Einstein temperature (θ_E) of 512K for a Holland-Powell-type thermal pressure model and a Tait 3rd-order EoS. Additionally, thermodynamic properties of grossular have been for the first time calculated from crystal Helmholtz and Gibbs energies, including the contribution from phonons, using density functional theory within the framework of the quasi-harmonic approximation. This paper was submitted to the international peer-reviewed journal *"American Mineralogist*" on February 2016 and is currently accepted with minor revisions.

Chapter 5 (manuscript #4). Is the paper with title: "*Thermal expansion of natural almandine garnet under controlled oxygen fugacity conditions"* by Scandolo L., Milani S., Di Prima M., McCammon C., Heidelbach F., Nestola F., Domeneghetti M.C., Alvaro M.. The manuscript provides an evaluation of the possible role of iron oxidation on the lattice parameters thermal expansion for Fe-rich aluminosilicate garnets. The oxidation state of the two garnets recovered after the high-T (up to 1110K) single crystal X-ray diffraction experiments performed under different fO_2 conditions has been evaluated using single-crystal Mössbauer spectroscopy. Mössbauer data confirmed that no oxidation occurs for the Fe-rich garnets up to at least about 1100 K neither for the "no buffer" nor for the "iron-wustite" buffered sample. The thermal expansion data nearly identical (within 2 e.s.d.'s) one to another indicates that there is no evident effect of the different fO_2 conditions in the vial on the thermal expansion behavior. This paper is in preparation and will be submitted by the end of 2016 to the international peer-reviewed journal "*American Mineralogist*".

The conclusions of this PhD thesis are reported in **Chapter 6**. **Appendix I:** Data obtained on eclogitic garnet.

Introduction

1.1. Diamonds

In the course of human history, diamonds, among all gemstone have always gathered great interest, not only because of their relevance from an economic point of view, but also for their implications in several scientific fields. Diamonds are mentioned in Indian manuscripts dating back to more than 2000 years ago. Until the 18th century, India was the only significant source of this gemstone (Levinson, 1998). Since their first discovery, an incredible number of studies have been focused on diamonds, not only because of their valuable use as gemstones (Koivula and Fryer, 1984, Boyajian, 1988, Fritsch and Shigley, 1993, Breeding et al., 2009) or the wide variety of industrial applications related to their outstanding properties (Newton, 1704, Tennant, 1797, Guyton 1799, Gassiot 1850) but also because, diamonds can provide several direct and indirect information about the interior of our planet, despite their rarity (part per-billion in most diamondiferous rocks). This kind of information could not otherwise be retrieved (e.g. transfer of material along the transition zone, timing of fluids ingress to the continental lithosphere, preserved carbonatic fluids, redox state of the mantle, primordial noble gases composition).

In fact, since the Newtonian theories in the early 18th century (Newton, 1704), diamond optical properties and several other ones such as elastic properties have been discussed and investigated by many scientists (e.g. Tennant, 1797). In the 18th century most of the scientific manuscripts were focused on understanding diamond properties in order to constrain the possible formation processes and environments suitable for diamond retrieval (Nature, 1870, Diller, 1886, Lewis, 1886, Derby 1887). A relevant contribution in this field came from those diamonds found in meteorites (Nature, 1887, Kunz, 1888, Huntigton, 1892). During the late 1800, the scientific attention was focused on the possible methods for diamond artificial production (Hannay, 1880). In fact, at the end of the 18th century, scientists started quantifying diamonds elastic properties (Guyton 1799) in order to bracket the temperature and pressure ranges suitable for their synthesis and in turn for their retrieval in nature.

Improvements in the technology and techniques (Electron Probe Micro-Analyzer, Transmission Electron Microscope, Scanning Electron Microscopy) in the last few decades has allowed us to better understand the nature of diamonds.

Nowadays, we know that diamonds crystallize in the earth mantle at a depth of more than 150 km which means about 5 GPa and 1400°C, assuming only pure lithostatic stresses and a cold

geothermal gradient typical of cratonic areas (e.g. Stachel et al. 2005) (Fig.1). Diamonds represent one of the several stable natural carbon mineral stable in the Earth mantle (other examples of widely known stable carbon phases are lonsdaleite, graphite), that also have been retrieved in several carbonaceous meteorites. Isotope dating on diamonds (earth mantle diamonds together with those occurring in carbonaceous chondrites) has confirmed their ancient provenance (e.g. 3.5 to 1 billion years) making them a fundamental phase that can record mantle conditions over a planetary evolution timescale (e.g. from the time of their growth; see Pearson and Shirey (1998) for more details).

Several processes of formation involving metasomatic C-H-O-Si-rich fluids with slightly different compositions permeating mantle rocks by promoting reactions that crystallize diamonds (Haggerty, 1999, Stachel et al., 2005, Shirey et al. 2013) have been proposed (Fig. 1). However, no definite evidence for the actual formation process of diamonds-as for others-, has been provided.

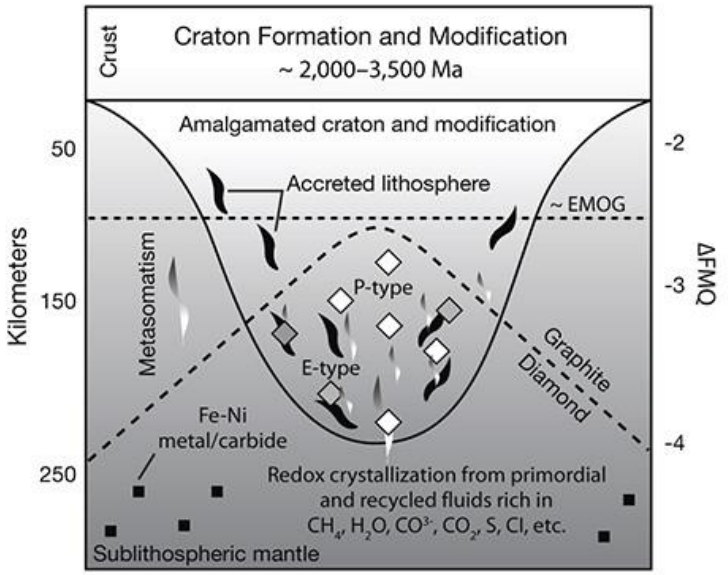

Fig. 1 Schematic representation of an ancient croatonic area, where because of the oxidation condition (ΔFMQ) metasomatic fluids reacts with the surrounding rocks in the cratonic roots, allowing the formation of diamonds (after Shirey et al., 2013).

The vast majority of the mined diamonds are called lithospheric diamonds or cratonic diamonds. These minerals come from cratonic areas (Fig. 2) which are characterized by exceptionally deep-reaching mantle keels that were largely originated in the Archean aeon. These regions are in the shallower upper mantle where the crust thickness guarantees lower temperatures if compared with the hotter convecting mantle at the same depth. This is mainly because there is only heat conduction, and the typical rocks forming mantle keels are depleted as far as heat producing elements (radioactive elements) are concerned. Only a low percentage of diamonds are actually assumed to come from the lower mantle or the deep mantle on the basis of the fact that

ultra-high pressure phases contained as inclusions have been found in those diamonds, but it is not clear which process has been involved in the formation of these phases.

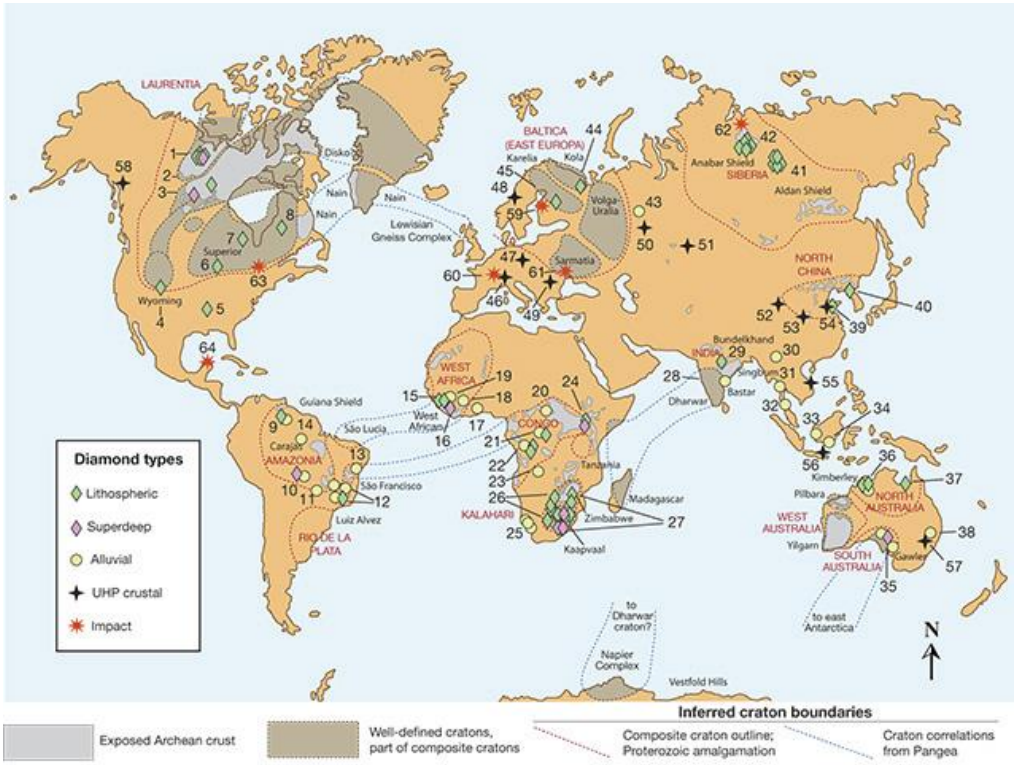

Fig. 2 Location of diamonds in relation to Archean cratons and their classification on the basis of their origin (after Shirey et al. 2013).

Focusing only on cratonic diamonds it is possible to realize that this phase could be found as xenocrystal only in very rare deposits. These host rocks are mostly made of rare type of magmas: kimberlite, amproite and lamprophyre (e.g. Gurney et al., 2010). These types of magma have peculiar characteristic: i) they are derived from melting deep to depth near the mantle; ii) they are relatively enriched by volatile elements (H_2O, CO_2, F or Cl); iii) they erupt rapidly; iv) they are not oxidized.

Within mantle keels, the main parental diamonds rocks are peridotitic and eclogitic rocks, and therefore are the minerals forming these rocks that typically were found as xenoliths along with diamonds or in the form of inclusions in diamonds themselves.

The simple structure and chemistry of diamonds makes it difficult to obtain information from these minerals as such.

The trace elements that can be found in diamonds structure are largely constituted by nitrogen, actually allowing us to estimate temperature of diamond formation (Taylor et al., 2009). However, only the xenoliths and phase inclusions in diamonds can provide constrain about the depth and therefore the environment in which diamonds have been formed, giving all the information briefly reported in this chapter. Xenoliths are more prone to a variety of alteration

processes near-surface; in detail, eclogitic xenoliths are resistant to weathering processes that in any case produce alteration phases forming at different pressure compared to diamonds (e.g., Misra et al., 2004; Howarth et al., 2015), while eclogitic peridotites easily disrupted, mainly because of the high content of olivine that is easily transformed into serpentines during hydrous alterations.

Therefore, in many cases diamond inclusions represent the unique unaltered samples providing indirect information that has enabled the discovery of some of the diamonds features, which have been previously summarized here.

1.2. Mineral inclusions

Mineral inclusions in cratonic diamonds measure typically less than 200 microns and have been found only in 1% of the total diamond population (Stechel et al., 2008). Indeed, diamond inclusions provide a unique unaffected sample coming from Earth's upper mantle and can give us peculiar information about the Earth's interior and its active geodynamics: i) providing the definition about the initiation of subduction processes (Shirey and Richardson, 2011), ii) tracking material transfer through the mantle transition zone (Stachel et al., 2005; Walter et al., 2011), iii) recording the timing of fluids ingress into the continental lithosphere (Richardson et al., 1984; Pearson et al., 1998; Shirey et al., 2004), iv) preserving carbonatitic fluid that trigger deep mantle melting (e.g. Schrauder and Navon, 1994; Kopylova et al., 2010), v) capturing the redox state of the mantle (e.g. Rohrbach and Schmidt, 2011), and vi) providing samples of primordial noble gases (e.g. Ozima and Igarashi 2000).

Stechel and Luth (2015) and Stachel and Harris (2008) have made nearly 5000 analyses on phase inclusions in diamonds. Based on their work, the inclusions can be subdivided in order of abundance: garnet (38%), olivine (19%), clinopyroxene (16%), orthopyroxene (8%), Mg-chromite and sulphides (19%) with a few sample of rutile and coesite (Fig. 3). The great importance of garnet and orthopyroxene, which together represent more than 46% of the total inclusions found so far, is clear.

The vast majority of these inclusions are believed to be syngenethic (Meyer, 1987; and Stechel and Harris, 2008) although an approved scientific method to distinguish syngenesis from protogenesis does not exist. Nowadays the growth relationship between a diamond and its inclusion is still a subject widely debated (Nestola et al., 2015 for a detailed discussion).

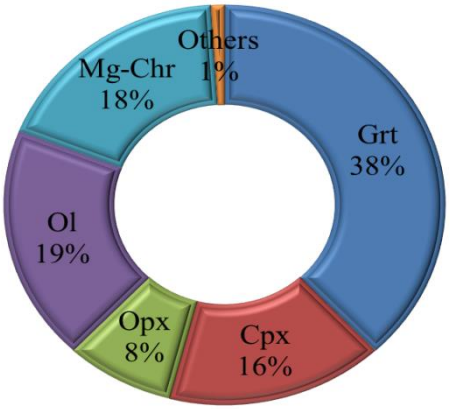

Fig. 3 Relative abundance of phases retrieved as inclusions in diamonds (after Stachel and Harris, 2008).

Chemical analysis carried out through microprobe analysis (EMPA) on mineral inclusions has allowed to recognize the host rocks containing diamonds in the mantle, based on inclusions chemical composition (Mayer, 1987; Shirey et al., 2013; Satchel and Harris, 2008). Unfortunately, EMPA analysis requires cutting the diamonds in order to expose the inclusion, with the consequent loss of information. Another nondestructive approach firstly conceived by Mitchel and Giardini in 1953 employs the use of X-ray diffraction to identify the mineral inclusions in a non-destructive way. This pioneer work was then followed by a lot of studies on diamonds from Russia (Orlov, 1977) and South Africa (Harris et al., 1967).

Lithospheric diamonds can be subdivided into different paragenesis based exclusively on the chemical composition of the inclusions (Fig. 4): peridotitic (which comprises: hazburgitic 56%, lherzolitic 8%, wherlitic 0.7%), eclogitic (33%), and websteritic suites (2%).

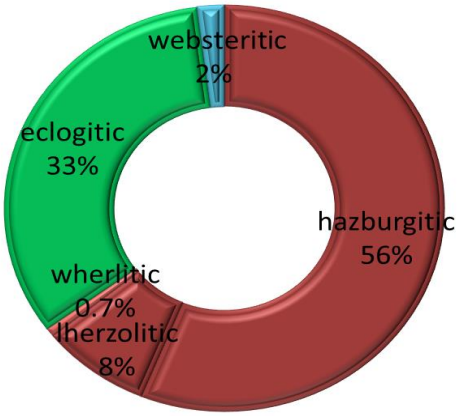

Fig. 4 Paragenesis of diamonds and relative percentages (after Stachel and Harris, 2008). Database includes 2844 inclusions in diamonds.

Microscope analysis (Fig. 5) with the identification of mineral color can be considered an expeditious analysis but can lead to erroneous interpretation, as demonstrated by Nestola et al., (2016).

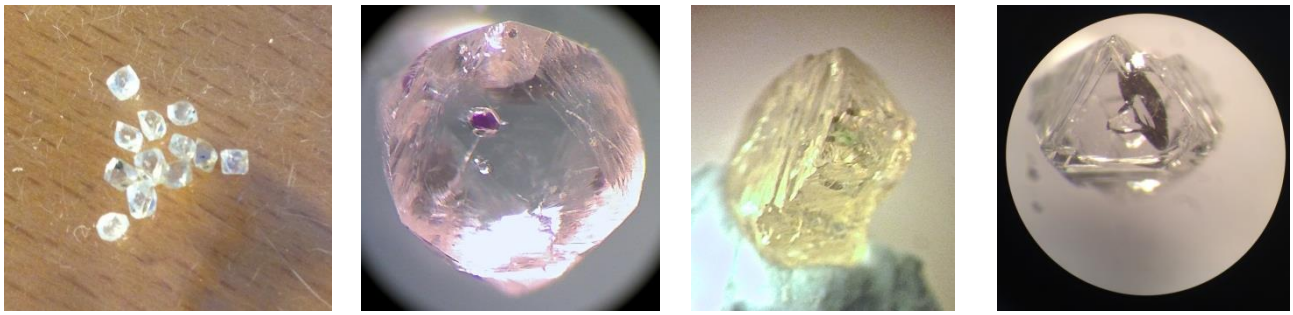

Fig. 5 Natural inclusions in diamonds observed at the optical microscope. From left: group of 12 diamonds with inclusions of purple garnet; pale green clinopyroxene; colourless olivine.

Hazburgitic and eclogitic suites can be recognized on the basis of the garnets inclusions composition (i.e. Microprobe conventional analysis): peridotitic garnets, which have hue ranges from pale pink to purple due to the thickness of the inclusion, are Cr-pyropes with high Mg, with typical low Ti content (<0.04%wt); while eclogitic garnets, which color are typically orange, have much lower Cr concentration (Meyer, 1987), and are higher on Ca content with more Mg variability.

Therefore, the boundary between eclogitic (lower in Cr) and peridotitic garnets is set arbitrarily at 1 wt% Cr_2O_3 (largely discussed in Gurney, 1984). Eclogitic garnets generally having <0.4 wt% of Cr_2O_3 content; however, if the Cr_2O_3 wt% is higher distinguishing eclogitic from websteritic suites based on correlation between Ca and Mg content becomes challenging.

Orthopyroxene inclusions, which are generally colourless or yellow/greenish, have been retrieved only in perioditic and websteritic suites.

Peridotitic orthopyroxene have typically higher magnesium content (95%) and between them the paragenesis could be recognize from the coexistence with garnet or clinopiroxene; among these, lherzolitic orthopyroxenes have Mg < 94.5 and CaO > 0.37 wt %. For garnet-orthopyroxene inclusions the Al_2O_3 content increases for orthopyroxene within the border, and is necessary realize as the amount may change due to garnet exsolution that may occur during equilibration while diamonds-host pair it is brought towards the surface.

Peridotite clinopyroxene can be distinguished from eclogitic clinopyroxene on the basis of Cr-Al ratio, indeed the latter are low in Cr_2O_3 and usually contain several Al_2O_3 wt%. As with garnet also for clinopyroxene a simple compositional definition of websteritic suite is lacking and the assignment is usually based on coexisting inclusions (i.e. garnet and orthopyroxene) (Stachel and Harris, 2008).

Lithospheric olivine, both lherzolitic and hazburgitic, generally have very high Mg content (>88 wt%). The high Cr content was explained by the incorporation of Cr^{2+} related to crystallization at low fO_2 and high temperature (Li et al., 1995). A coexisting garnet or clinopyroxene allows to

assign olivine inclusions to hazburgitic or lerzholitic paragenesis, basically using the distribution of Mg and Ca elements between the two minerals (Kohler and Brey, 1990).

Spinel inclusions in diamonds relate to high Cr/Al in cratonic peridotites that stabilizes Cr-rich spinel deep into garnet stability field (Weeb and Wood, 1986). Paragenesis of spinel remains unclear, mainly because these inclusions are rarely observed together with garnets. Mg chromite inclusions show a large range of Mg content (between 60 and 80 wt%) reflecting both a difference in source composition and temperature crystallization (Fe/Mg partitioning with olivine). Iron contents also show high variability with generally high percentage (up to 45%) of ferric iron (Stachel and Harris, 2008).

Sulphide inclusions, predominantly containing Fe-Ni-S, show intense sub-solidus exsolution into various low temperature phases which are supposed to have been formed during different stages of cooling while they were trapped within diamonds (Guo et al., 1999).

The chemical composition of the different minerals phases can be determined by EMPA analysis if it is possible to cut the diamond and expose the inclusions. Avoiding the breakup of the diamond is possible by using non-destructive methods: X-ray diffraction (Nestola et al., 2011, 2012.), Micro-Raman spectroscopy (Barron et al., 2008 and references therein), transmission X-ray diffraction (Smith et al., 2011). Single-crystal X-ray diffraction allows to combine unit-cell parameters and crystal structure information, and represent the main advantage of this technique. However, the application of this technique requires to center the inclusion in the X-ray beam (e.g., Kunz et al., 2002) which is an experimental problem. The centering problem can be solved as demonstrated in Nestola et al. (2012), using X-ray computed micro-tomography which provides three dimensional maps with a spatial resolution of a few micrometers, in a non-invasive manner, within the diamond-inclusion pair.

Furthermore, the complexity of the crystallographic structure of inclusions influences the level of difficulty through which it is possible to determine the exact composition of inclusions still trapped in diamonds, thanks to X-ray structure refinement. The in situ determination of the composition for inclusions that show limited cation substitution (olivine, orthopyroxene and ringwoodite) is relatively easy to achieve (Nestola et al., 2011). However, as recently demonstrated by Nestola et al. (2016), combining structural refinement details: unit-cell parameters, mean atomic number analysis and bond lengths, obtained from data collected by in situ single-crystal synchrotron X-ray diffraction using a new experimental setup, it is possible to obtain significant indications of composition even for monoclinic structures (i.e. clinopyroxene or garnet) still trapped in diamonds.

1.3. Diamond pressure and temperature of formation, the classical thermobarometry approach

Constraints in the growth environment and the conditions of diamonds formation are essential to determine the pressure, and thus the depth at which these phases have been formed. In order to retrieve this information, there are basically two complementary approaches: i) either the classical thermobarometry method, which is based on chemical partitioning between two adjacent phases in chemical equilibrium contained in the diamonds (O'Neil and Wodd, 1979; Harley, 1984; Brey and Kohler, 1990), or in considering one phase assumed to be in equilibrium with the corresponding missing phase capable of buffering its composition under certain P and T (e.g. Ryan et al., 1996; Nimis and Taylor, 2000; Grütter et al., 2006; Simakov, 2008; Creighton, 2009); ii) the recently developed elastic thermobarometry method, based on the measurement of residual pressure (P_{inc}) of the inclusion still trapped in the diamond at room conditions (e.g. Izraeli et al., 1999; Angel et al., 2014a,b).

The classical thermobarometry method, which requires routine chemical microprobe analysis (EMPA), is not always applicable for diamonds-inclusions pairs for several reasons: i) only in rare cases non-touching mineralogical phases needed to apply classical barometry, subsist in the same diamonds; ii) equilibration between phases could take place slowly and thus recording pressure and temperature different from that occurring at the time of diamond and inclusions formation for touching inclusions; iii) classical thermobarometry methods is not yet available for several type of common inclusions in diamonds (such as for eclogitic mineral assemblages); iv) the inclusions need to be exposed for microprobe analysis, involving the break-up of the diamond, which is not always permitted by diamond owners.

In addition, thermobarometry for a single inclusion (Zn-in spinal: Ryan et al., 1996; clynopyroxene: TNT and PNT, Nimis and Taylor, 2000) needs to assume the composition and the chemical equilibrium of the missing phase, leading to bring forth very large uncertainties (e.g. from 0.5 GPa for the most reliable to several GPa for the others), and consequently for specific inclusions population may mask a possible heterogeneity in the vertical distribution of the diamonds. Furthermore, due to the break-up of the single crystal inclusion the crystal structure can be modified in any case mainly through the release of the remnant pressure.

However, the garnet and pyroxene mineral families have been widely used in the classical thermobarometry method, particularly those based on: Fe-Mg exchange reactions (Brey and Kohler, 1990); or the tschermakitic ($MgCrAlSiO_6$) component (e.g. Harley, 1984; Nickel and Green, 1984; Bertrand and Marcier, 1985; Mac Gregor 1986; Nickel 1989; Brey and Köhler, 1990; Taylor and Nimis, 1998).

The accuracy of the Opx-Grt barometers at P > 5 GPa and for Orthopyroxene with excess of Na over Cr +Ti has not been estimated sufficiently (Carswell et al., 1991; Nimis and Gutter, 2012).

Partitioning between olivine and clinopyroxene (Brey and Kohler, 1990) is problematic for the low Ca content in natural olivine and the strong temperature dependency of the Ca exchange reaction.

Aluminum exchange between clinopyroxene and garnet may be used as a geobarometer (Brey et al., 1986, Mukhopadhyay 1991), but the non-ideal behaviour of both clinopyroxene and garnet solid-solutions make the applicability of this system usable only for a restricted system (CMAS, CaO-MgO-Al_2O_3-SiO_3), and it therefore gives only qualitative results (e.g. Nimis 1998).

Marcier (1980) formulated a single orthopyroxene or clinopyroxene geobarometer, but as established by Finnerty and Boyd (1984), these barometers could give grossly erroneous results.

Brey et al. (1990) showed that the Cr content of clynopyroxene in equilibrium with a garnet is pressure dependent and demonstrated that for lherzolitic compositions Cr is more soluble in clinopyroxene than in orthopyroxene; therefore, Nimis et al. (2000) formulated a geobarometric expression based on the Cr-exchange reaction between clinopyroxene and a garnet providing a reliable estimate of pressure conditions (σ_P=2-3 Kbar) of equilibration of natural garnet lherzolites.

The widely used thermometers for mantle peridotites may diverge by over 200°C for equilibrated sample, therefore the choice and appropriate scheme combining different thermometers results fundamental as described by Nimis and Grütter, (2010).

Thermobarometry for eclogitic inclusions are not yet available and Fe-Mg thermometry of Grt-Cpx pairs is affected by large uncertainties (±100°C), owing to Fe^{3+} that produce a broadening of the pyroxene miscibility gap (Krogh Ravna and Paquin, 2003). Majorite-rich garnet inclusions are potentially linked to rare super deep diamonds (Stachel et al., 2005; Tappert et al., 2009; Walter et al., 2011), allow the minimum pressure of formation to be estimated from the fraction of the majoritic component (Collerson et al., 2010).

For a more detailed explanation on P-T estimate and for a review of the data available on single- and two-mineral thermobarometry see Stachel and Harris (2008) paper.

The limitations of classical barometry have favored the development of an alternative approach based on the elastic behavior of the diamond-host and inclusion, which can be applied to any host-inclusions system, considering the base assumptions of the method, as described by Angel et al. (2014a,b).

1.4. Elastic geobarometry

Elastic barometry just takes into account the difference between the elastic properties (expansivity and compressibility) of inclusion and the diamond-host that give rises to inclusion pressure (P_{inc}), regardless of the *P-T-t* path taken upon exhumation. Therefore, P_{inc} is the pressure exerted by the diamond on the inclusion when the diamond-inclusion pair is at room P-T ("the sample is in our hands").

Conceptually, at the time of growth the diamond-host and inclusion phases are subject to the same temperature-pressure conditions; therefore, the inclusion is perfectly joined within the diamond cavity in which it is contained in ($V_{host\ cavity} = V_{inclusion}$), without any empty space. Subsequently, the phase is completely enclosed by the diamond, and the system becomes elastically closed. The inclusion is always softer than diamonds (characterized by very low compressibility, and expansibility). Therefore, when the host-inlcusion pair is brought up to the surface, it occurs that the inclusion pushes against the walls of the diamond cavity (Fig. 6).

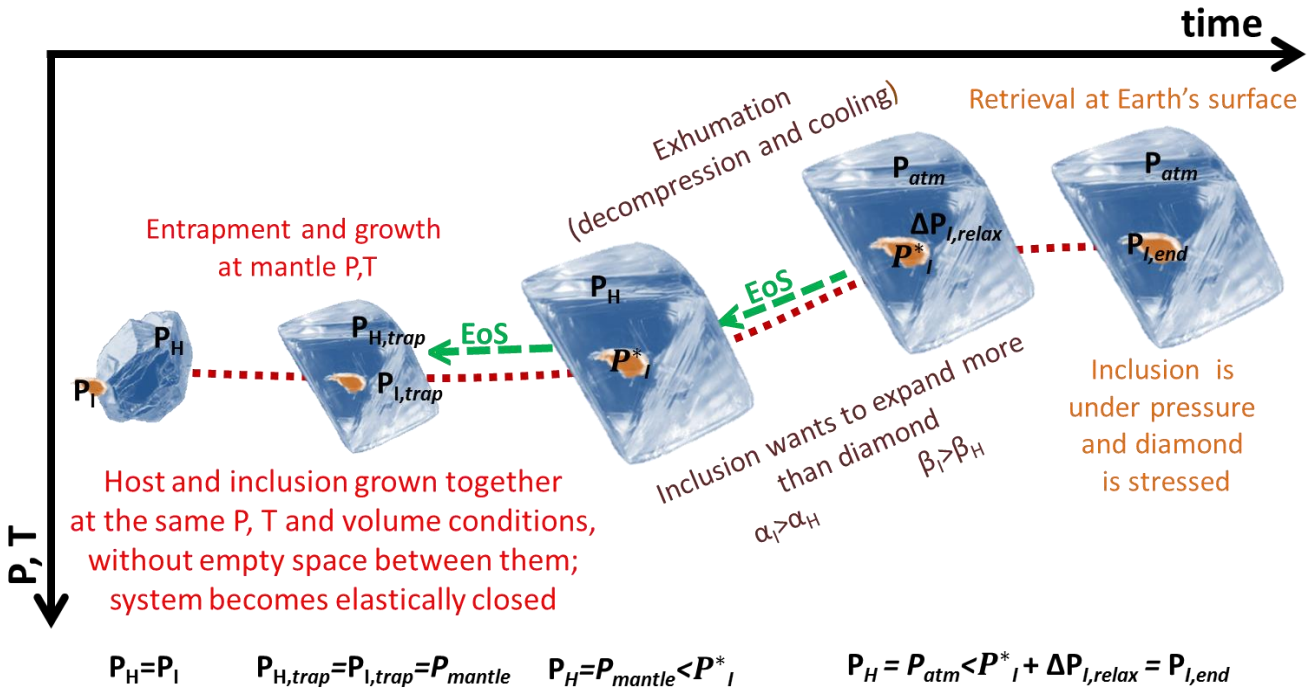

Fig. 6 P-T history of diamond (blue) and its inclusion (orange). See text for further details.

The result is that the inclusion is under pressure, and it is called remnant pressure ($P_{inc} = P_{I,end}$) that can be determined by X-ray diffraction (Harris et al., 1970; Nestola et al., 2011), micro-Raman spectroscopy (Nasdala et al., 2003; Barron et al., 2008) or birefringence analysis (Howell et al., 2010) which are all non-destructive techniques. However this remnant pressure ($P_{I,end}$) does not match the one (P_I^*) calculated by the EoS (i.e. Equation of State) for both the phases, which is generally lower due to a relaxation (slight deformation) that results around the cavity walls

containing the inclusion. Therefore, as described by Angel et al. (2014a) remnant pressure can be described as the sum of two components:

$$P_{I,end} = P_I^* + \Delta P_{I,relax}$$

Where $\Delta P_{I,relax}$ represents relaxation term already described in literature (Zhang, 1998; Izraeli et al., 1999, Howell et al., 2012). Angel et al. (2014a) improved their estimation of the relaxation term, taking into account that elastic properties of both phases are not linear but change as functions of pressure and temperature. Relaxation term usually appear very small for inclusions in diamonds (0.1-0.2 GPa); however, for some metamorphic inclusion pairs the relaxation can exceed the difference between the unrelaxed inclusion pressure P^* by up to 50% and the external pressure and thus can strongly affect calculation of formation depth.

The diamond-inclusion system used in this method is being considered completely elastic and the P-T path followed by phases doesn't affect stress and strain in the host and inclusion pair. Stress and strain arise only from different elastic properties (thermal expansion and compressibility) of diamond-hosts and inclusions; therefore, it could be stated that final pressure ($P_{I,end}$) is the same for any P-T path.

From the residual pressure (P_I^*) knowing the thermoelastic properties of the inclusions and the host (considering the EoS of the two phases) it is possible to back calculate the pressure of diamond-inclusion formation (P_e, Angel, 2014a,b; Angel, 2015) following a two-step path (Fig. 7):

1) Considering: P_{inc}, relaxation term and elastic parameters (compressibility) of the host and the inclusion, the system will be moving along an isothermal path until the volume of the cavity of the diamond matches the volume of the inclusion perfectly, thus eliminating the residual stress that was present;

2) Moving the system through a path in P-T space, which is called Isomeke, along which: fractional volume change of the cavity in the host ($\partial V_H/V_H$) and of the inclusion ($\partial V_I/V_I$) are the same (Angel et al., 2015). As described in Angel et al. (2015), the fractional volume change of an unconstrained phase is defined as:

$$\frac{\partial V_H}{V_H} = \alpha_H \partial T - \beta_H \partial P$$

where α_H is the volume thermal expansion and β_H is the volume compressibility, characteristic of the host. The same equation can be used to calculate the fractional volume change of the inclusion. Through these two equations we can constrain the changes in the P-T space as:

$$\frac{\partial P}{\partial T} = \frac{\alpha_I - \alpha_H}{\beta_I - \beta_H}$$

As stated by Angel et al. (2015), the isomeke is not a straight line in P-T space, because the variation of α and β in the closed system will evolve differently. As defined in Rosenfeld and Chase

(1961), the only absolute constraint on the slope of the isomeke is $\frac{\partial P}{\partial T} = 0$ at absolute zero, because at this temperature α is equal to zero.

However, it must be noticed that this approach is based on some assumptions already reported by Zhang (1998), which can be considered reliable for most of the inclusions in diamonds:

- Inclusion and host are concentric spheres
- The inclusion is infinitely smaller compared to the host
- Both phases are elastically isotropic
- The outer surface of the host crystal is under uniform isotropic stress
- The temperature of the inclusion is expected to be always the same as that of the host
- The host deforms elastically, and no plastic or brittle deformation takes place during transportation to the surface.

For this reason (i.e., the inclusion is not isolated, the host and the inclusion are not elastically isotropic) the entrapment pressure cannot be evaluated algebraically, but every case has to be considered individually by finite-element numerical modeling or use of approximations (Angel et al., 2015), that will not be discussed here.

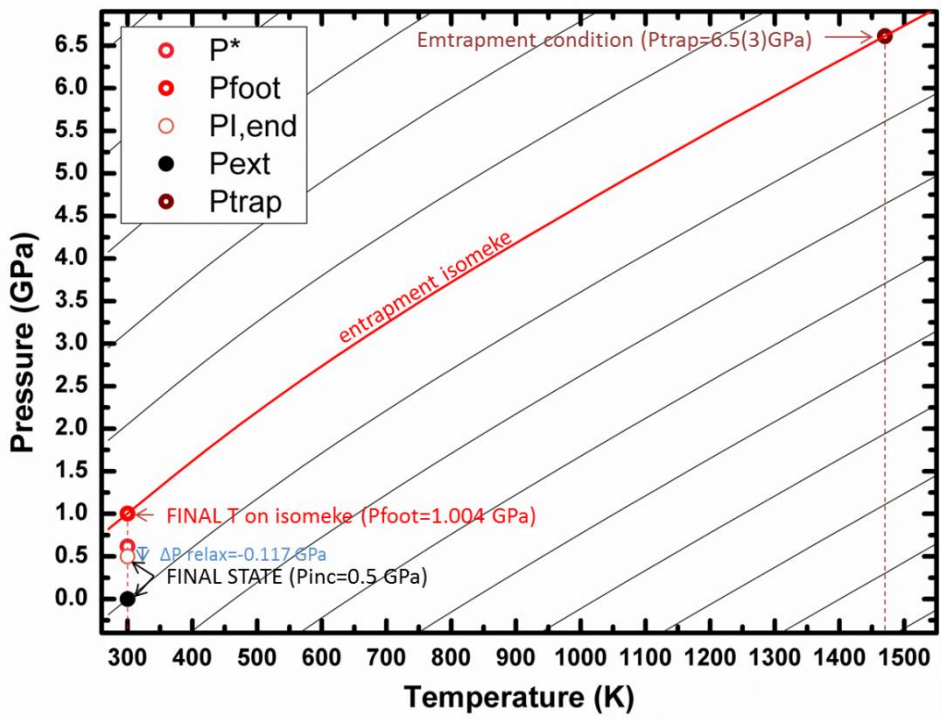

Fig. 7 Isomeke paths for an ideally pure almandine inclusion entrapped in diamond. The various black curves have been obtained assuming different $P_{I,end}$ (i.e. P_{inc}). The red line represents the P,T isomeke path for $P_{I,end}$ = 0.5 GPa, which is the typical inclusion pressure determined from X-ray diffraction experiments on garnet inclusions. For further details see text.

The thermoelastic parameters of diamonds have already been determined in literature (Angel et al., 2014a) to a precision that yields negligible uncertainties in the entrapment pressure (Pe) values back calculated from Pinc. The thermoelastic properties of other mineral phases with various compositions frequently occurring as inclusions in diamonds have been determined to the required precision in very few literature studies, and in some cases have never been estimated.

Elastic barometry provides a complementary and non-destructive alternative for the evaluation of the formation pressure for a diamond containing a monomineralic inclusion compared to classical barometry. However, in order to apply this method, the knowledge of the thermoelastic properties (i.e α and β), which need to be measured with a sufficient degree of consistency, accuracy and precision for each end-member phase belonging to the mineral family of the single inclusion phase, is required.

1.5. Thermoelastic parameters determination

The accuracy and precision in the determination of EoS (thermal expansion and compressibility) for both the diamond and the inclusion, play a crucial role in calculating a realistic entrapment pressure value (P_e), as has been already mentioned. The thermal equations of state for diamond have been thoroughly analyzed and all the parameters are well known (e.g. Angel et al., 2014a for a review), but this is still missing for various inclusions phases.

The thermoelastic behaviour (EoS) of phases can be measured using different approaches.

Simultaneous pressure-volume and temperature experiments (P-V-T) allow the direct measurement of bulk modulus variations as a function of the temperature ($\partial K/\partial T$): that is the only parameter which correlates high temperature with high pressure behavior of mineral phases, using the classical EoS. These experiments (Brillouin scattering and Resonance Ultrasound Spectroscopy) require very expensive instrumentation, difficult to develop and design, but the greatest disadvantage regards the necessarily simultaneous calibration of temperature and pressure required by these approaches, which is always very challenging (Fei and Wang, 2000; Miletich et al., 2009).

An alternative is provided by "thermal pressure" EoS (Anderson, 1995; Holland and Powell, 2011), implemented in EoS-fit software by Angel (2104b):

$$P(V,T)= P(V,T_{ref})+ P_{th}(T)$$

This equation allows to distinguish pressure contribution in to two terms: 1) the isothermal equation of state at reference temperature $P(V,T_{ref})$; 2) the contribution given by temperature which creates pressure while its increasing at constant volume and at room pressure $P_{th}(T)$. Therefore, this equation permits to combine two different EoS, obtained by performing high pressure experiments separately from high temperature ones. Realistic thermal behavior must be obtained performing low temperature experiments on the same sample analyzed at high temperature; the two data sets must

be comparable in order to combine them in the same thermal EoS (thermal pressure in the model used at ambient pressure gives the same values as in Kroll et al., 2012).

The great advantage of this approach is that it is possible to control temperature calibration separately from pressure calibration, obtaining much more reliable parameters.

Thermal pressure EoS requires that sets of measured data are consistent with one other, which implies that: high pressure and high temperature data must show comparable precision, accuracy, and that experiments must be performed on the same sample with a well-known composition. Therefore, this approach is much more time consuming if compared with the simultaneous P-V-T measurements, but produces much more reliable results at P-T ranges typical of the Earth's mantle.

1.6. References

Anderson, O.L., Masuda, K., and Isaak, D.G. (1995) A new thermodynamic approach for high-pressure physics. Physics of the Earth and Planetary Interiors, 91(1), 3-16.

Angel RJ, Mazzucchelli M, Alvaro M, Nimis P, Nestola F (2014a) Geobarometry from host-inclusion systems: the role of elastic relaxation. Am Mineral 99, 2146-2149.

Angel, R.J., Gonzalez-Platas, J., Alvaro, M., (2014b). EosFit-7c and a Fortran module (library) for equation of state calculations. Zeit Kristall 229, 405-419.

Angel, R., Alvaro, M., Nestola, F., and Mazzucchelli, M. (2015) Diamond thermoelastic properties and implications for determining the pressure of formation of diamond-inclusion systems. Russian Geology and Geophysics, 56(1), 211-220.

Barron LM, Mernagh TP, Barron BJ (2008) Using strain birefringence in diamond to estimate the remnant pressure on an inclusion. Aust J Earth Sci 55:159-165.

Breeding, C.M., and Shigley, J.E. (2009) The "type" classification system of diamonds and its importance in gemology. Gems & Gemology, 45(2), 96-111.

Bertrand, P., and Mercier, J.-C.C. (1985) The mutual solubility of coexisting ortho-and clinopyroxene: toward an absolute geothermometer for the natural system? Earth and Planetary Science Letters, 76(1-2), 109-122.

Boyajian, W. (1988) An economic review of the past decade in diamonds. Gems & Gemology, 24(3), 134-153.

Brey, G., Nickel, K., and Kogarko, L. (1986) Garnet-pyroxene equilibria in the system CaO-MgO-Al2O3-SiO2 (CMAS): prospects for simplified ('T-independent') lherzolite barometry and an eclogite-barometer. Contributions to Mineralogy and Petrology, 92(4), 448-455.

Brey, G., and Köhler, T. (1990) Geothermobarometry in four-phase lherzolites II. New thermobarometers, and practical assessment of existing thermobarometers. Journal of Petrology, 31(6), 1353-1378.

Carswell, D. (1991) The garnet-orthopyroxene A1 barometer: problematic application to natural garnet lherzolite assemblages. Mineralogical Magazine, 55, 19-31.

Collerson, K.D., Williams, Q., Kamber, B.S., Omori, S., Arai, H., and Ohtani, E. (2010) Majoritic garnet: A new approach to pressure estimation of shock events in meteorites and the encapsulation of sub-lithospheric inclusions in diamond. Geochimica et Cosmochimica Acta, 74(20), 5939-5957.

Creighton S, Stachel T, Matveev S, Höfer HE, McCammon C, Luth RW (2009) Oxidation of the Kaapvaal lithospheric mantle driven by metasomatism. Contrib Mineral Petrol 157, 491–504.

Derby, O.A. (1887) The Genesis of the Diamond. Science, 9(207), 57-58.

Diller, J.S. (1886) The Genesis of the Diamond. Science, 8(195), 392.

Fei, Y., and Wang, Y. (2000) High-Pressure and High-Temperature Powder Diffraction. Reviews in Mineralogy and Geochemistry, 41(1), 521-557.

Finnerty, A., and Boyd, F. (1984) Evaluation of thermobarometers for garnet peridotites. Geochimica et Cosmochimica Acta, 48(1), 15-27.

Fritsch, E., and Shigley, J. (1993) The separation of natural from synthetic gem-quality diamonds on the basis of crystal growth criteria. Journal of Crystal Growth, 128(1), 425-428.

Gassiot, S.P. (1850) On a peculiar form produced in a diamond when under the influence of the Voltaic Arc. Journal of the Franklin Institute, 50(6), 398-399.

Grütter, H., Latti, D., and Menzies, A. (2006) Cr-saturation arrays in concentrate garnet compositions from kimberlite and their use in mantle barometry. Journal of Petrology, 47(4), 801-820.

Guo, J., Griffin, W.L., and O'Reilly, S.Y. (1999) Geochemistry and origin of sulphide minerals in mantle xenoliths: Qilin, Southeastern China. Journal of Petrology, 40(7), 1125-1149.

Gurney JJ, Harris JW, Rickard RS (1984) Minerals associated with diamonds from the Roberts Victor MineIn: KimberlitesII:The mantle and crust-mantle relationships. Kornprobst J (ed) Elsevier., Amsterdam, Netherlands (NLD), p 25-32.

Gurney JJ, Helmstaedt HH, Richardson SH, Shirey SB (2010) Diamonds through time. Econ Geol 105:689-712.

Guyton, C. (1799) XII. Extract from the report respecting experiments made at the Polytechnic School in the years V. and VI. on the combustion of the diamond. Philosophical Magazine Series 1, 5(17), 55-61.

Haggerty, S.E. (1999) Diamond formation and kimberlite clan magmatism. Geochem Soc Spec Publ, 6, 105-123.

Hannay, J.B. (1880) On the artificial formation of the diamond. Journal of the Franklin Institute, 110(2), 123-135.

Harley, S.L. (1984) An experimental study of the partitioning of Fe and Mg between garnet and orthopyroxene. Contributions to Mineralogy and Petrology, 86(4), 359-373.

Harris JW, Henrique R, Meyer HOA (1967) Orientation of silicate mineral inclusions in diamonds. Crystal Growth 7, 118–123

Harris JW, Milledge HJ, Barron THK, Munn RW (1970) Thermal expansion of garnets included in diamond. J Geophys Res 75:5775-5792.

Holland, T.J.B., and Powell, R. (2011) An improved and extended internally consistent thermodynamic dataset for phases of petrological interest, involving a new equation of state for solids. Journal of Metamorphic Geology, 29(3), 333-383.

Howarth, G.H., Sobolev, N.V., Pernet-Fisher, J.F., Ketcham, R.A., Maisano, J.A., Pokhilenko, L.N., Taylor, D., and Taylor, L.A. (2015) 3-D X-ray tomography of diamondiferous mantle eclogite xenoliths, Siberia: A review. Journal of Asian Earth Sciences, 101, 39-67.

Howell D, Wood IG, Dobson DP, Jones AP, Nasdala L, Harris JW (2010) Quantifying strain birefringence halos around inclusions in diamond. Contrib Mineral Petrol 160, 705-717.

Howell D, Wood IG, Nestola F, Nimis P, Nasdala L (2012) Inclusions under remnant pressure in diamond: A multi-technique approach. Eur J Mineral 24, 563-573.

Huntington, O.W. (1892) Diamonds in Meteorites. Science, 20(492), 15.

Izraeli ES, Harris JW, Navon O (1999) Raman barometry of diamond formation. Earth Planet Sci Lett 173: 351–360.

Levinson, A.A. (1998) Diamond sources and their discovery. The nature of diamonds, 72-104.

Lewis, H.C. (1886) The Genesis of the Diamond. Science, 8(193), 345-347.

Li, J.-P., O'Neil, H.S.C., and Seifert, F. (1995) Subsolidus Phase Relations in the System MgO-SiO2-Gr-O in Equilibrium with Metallic Cr, and their Significance for the Petrochemistry of Chromium. Journal of Petrology, 36(1), 107-132.

Köhler, T., and Brey, G. (1990) Calcium exchange between olivine and clinopyroxene calibrated as a geothermobarometer for natural peridotites from 2 to 60 kb with applications. Geochimica et Cosmochimica Acta, 54(9), 2375-2388

Koivula, J.I., and Fryer, C.W. (1984) Identifying gem-quality synthetic diamonds: an update. Gems and Gemology, 20(3), 146-158.

Kopylova M, Navon O, Dubrovinsky L, Khachatryan G (2010) Carbonatitic mineralogy of natural diamond forming fluids. Earth Planet Sci Lett 291, 126-137.

Kroll, H., Kirfel, A., Heinemann, R., and Barbier, B. (2012) Volume thermal expansion and related thermophysical parameters in the Mg, Fe olivine solid-solution series. European Journal of Mineralogy, 24(6), 935-956.

Kunz, G.F. (1888) Diamonds in Meteorites. Science, ns-11(266), 118-119.

Kunz, M., Gillet, P., Fiquet, G., Sautter, V., Graafsma, H., Conrad, P., and Harris, J. (2002) Combined in situ X-ray diffraction and Raman spectroscopy on majoritic garnet inclusions in diamonds. Earth and Planetary Science Letters, 198(3-4), 485-493.

MacGregor, I.D., and Manton, W.I. (1986) Roberts Victor eclogites: ancient oceanic crust. Journal of Geophysical Research: Solid Earth, 91(B14), 14063-14079.

Mercier, J.-C.C. (1980) Single-pyroxene thermobarometry. Tectonophysics, 70(1), 1-37.

Meyer HOA (1987) Inclusions in diamond. In: Nixon, P.H. (Ed.), Mantle xenoliths. John Wiley & Sons Ltd., Chichester, 501–522.

Miletich, R., Cinato, D., and Johänntgen, S. (2009) An internally heated composite gasket for diamond-anvil cells using the pressure-chamber wall as the heating element. High Pressure Research, 29(2), 290-305.

Misra, K.C., Anand, M., Taylor, L.A., and Sobolev, N.V. (2004) Multi-stage metasomatism of diamondiferous eclogite xenoliths from the Udachnaya kimberlite pipe, Yakutia, Siberia. Contributions to Mineralogy and Petrology, 146(6), 696-714.

Mitchell RS, Giardini AA (1953) Oriented olivine inclusions in diamond. Am Mineral 38: 136–138.

Mukhopadhyay, B. (1991) Garnet-clinopyroxene geobarometry; the problems, a prospect, and an approximate solution with some applications. American Mineralogist, 76(3-4), 512-529.

Nature, e.c.-. (1870) The geology of the diamond fields of South Africa. Nature, 3(53), 2-3.

Nature, e.c.-. (1887) Discovery of diamonds in a meteoric stone. Nature, 37(944), 110-111.

Nasdala, L., E. Brenker, F., Glinnemann, J., Hofmeister, W., Gasparik, T., W. Harris J., Stachel T., Reese, I. (2003) Spectroscopic 2D-tomography, European Journal of Mineralogy, 15 (6) 931-935; DOI: 10.1127/0935-1221/2003/0015-0931

Nestola, F., Nimis, P., Ziberna, L., Longo, M., Marzoli, A., Harris, J.W., Manghnani, M.H., Fedortchouk, Y., (2011). First crystal-structure determination of olivine in diamond: Composition and implications for provenance in the Earth's mantle. Earth and Planetary Science Letters 305, 249-255.

Nestola F, Merli M, Nimis P, Parisatto M, Kopylova M, De Stefano A, Longo M, Ziberna L, Manghnani M (2012) In situ analysis of garnet inclusion in diamond using single-crystal X-ray diffraction and X-ray micro-tomography. Eur J Mineral 24, 599-606.

Nestola, F., Nimis, P., Angel, R.J., Milani, S., Bruno, M., Prencipe, M., Harris, J.W. (2014) Olivine with diamond-imposed morphology included in diamond. Syngenesis or protogenesis? Int. Geol. Rev., 56, 1658–1667

Nestola F., Alvaro M., Casati M.N., Wilhelm H., Kleppe A.K., Jephcoat A.P., Domeneghetti M.C., Harris J.W. (2016) Source assemblage types for cratonic diamonds from X-ray Synchrotron diffraction. Lithos, in press.

Newton, I. (1704) Opticks. Courier Dover Publications.

Nickel, K., and Green, D. (1984) The nature of the upper-most mantle beneath Victoria, Australia as deduced from ultramafic xenoliths. Kimberlites II: the mantle and crust–mantle relationships. Elsevier, Amsterdam, 161-178.

Nickel, K. (1989) Garnet-pyroxene equilibria in the system SMACCR (SiO2–MgO–Al2O3–CaO–Cr2O3): the Cr-geobarometer. Kimberlites and related rocks, 2, 901-912.

Nimis, P., Ulmer, P., (1998) Clinopyroxene geobarometry of magmatic rocks. Part 1: An expanded structural geobarometer for anhydrous and hydrous, basic and ultrabasic systems, Contributions to Mineralogy and Petrology, 133 (1-2), 122-135.

Nimis P, Taylor WR (2000) Single clinopyroxene thermobarometry for garnet peridotites. Part I. Calibration and testing of a Cr-in-Cpx barometer and an enstatite-in-Cpx thermometer. Contribution to Mineralogy and Petrology 139, 541-554.

Nimis, P., and Grütter, H. (2010) Internally consistent geothermometers for garnet peridotites and pyroxenites. Contributions to Mineralogy and Petrology, 159(3), 411-427.

Nimis, P., and Grütter, H. (2012) Discussion of "The applicability of garnet–orthopyroxene geobarometry in mantle xenoliths", by Wu C.-M. and Zhao G. Lithos, 142, 285-287.

Nimis, P., Nestola, F., Angel, R.J., Milani, S., Alvaro, M., Anzolini, C., Schiazza, M., Bruno, M., Prencipe, M., and Harris, J.W. (2015) Crystallographic relationships between diamond and its inclusions. EGU General Assembly Conference Abstracts, 17, p. 13240.

O'Neill, H.S.C., and Wood, B. (1979) An experimental study of Fe-Mg partitioning between garnet and olivine and its calibration as a geothermometer. Contributions to Mineralogy and Petrology, 70(1), 59-70.

Orlov YL (1977) The mineralogy of the diamond. John Wiley and Sons, NewYork. 235 pp.

Ozima M, Igarashi G (2000) The primordial noble gases in the Earth; a key constraint on Earth evolution models. Earth Planet Sci Lett 176, 219-232.

Pearson DG, Shirey SB, Harris JW, Carlson RW (1998) Sulphide inclusions in diamonds from the Koffiefontein kimberlite, S Africa; constraints on diamond ages and mantle Re-Os systematics. Earth Planet Sci Lett 160, 311-326.

Ravna, E.K., and Paquin, J. (2003) Thermobarometric methodologies applicable to eclogites and garnet ultrabasites. EMU notes in mineralogy, 5(8), 229-259.

Richardson SH, Gurney JJ, Erlank AJ, Harris JW (1984) Origin of diamonds in old enriched mantle. Nature 310, 198-202.

Rohrbach A, Schmidt MW (2011) Redox freezing and melting in the Earth's deep mantle resulting from carbonironredox coupling. Nature 472, 209-214.

Rosenfeld JL, Chase AB (1961) Pressure and temperature of crystallization from elastic effects

around solid inclusions in minerals?. Am J Sci 259, 519-541.

Ryan CG, Griffin WL, Pearson NJ (1996) Garnet geotherms: pressure temperature data from Cr-pyrope garnet xenocrysts in volcanic rocks. J Geophy Res 101, 5611-5626.

Schrauder M, Navon O (1994) Hydrous and carbonatitic mantle fluids in fibrous diamonds from Jwaneng, Botswana. Geochim Cosmochim Acta 58, 761-771.

Shirey, S.B., Richardson, S.H., Harris, J.W., (2004) Integrated models of diamond formation and craton evolution. Lithos 77, 923-944.

Shirey, S.B., Richardson, S.H., (2011) Start of the Wilson cycle at 3 Ga shown by diamonds from subcontinental mantle. Science 333, 434-436.

Shirey SB, Cartigny P, Frost DJ, Keshav S, Nestola F, Nimis P, Pearson DG, Sobolev Nv, Walter MJ (2013) Diamonds and the geology of mantle carbon. Rev Mineral Geochem 75:355-421.

Simakov SK (2008) Garnet–clinopyroxene and clinopyroxene geothermobarometry of deep mantle and crust eclogites and peridotites. Lithos 106:125–136.

Smith, E., Kopylova, M., Dubrovinsky, L., Navon, O., Ryder, J., and Tomlinson, E. (2011) Transmission X-ray diffraction as a new tool for diamond fluid inclusion studies. Mineralogical Magazine, 75(5), 2657-2675.

Stachel T, Brey GP, Harris JW (2005) Inclusions in sub-lithospheric diamonds; glimpses of deep earth. Elements 1:73-87.

Stachel T, Harris JW (2008) The origin of cratonic diamonds - constraints from mineral inclusions. Ore Geol Rev 34:5-32.

Stachel, T., and Luth, R. (2015) Diamond formation—Where, when and how? Lithos, 220, 200-220.

Tappert, R., Foden, J., Stachel, T., Muehlenbachs, K., Tappert, M., and Wills, K. (2009) Deep mantle diamonds from South Australia: A record of Pacific subduction at the Gondwanan margin. Geology, 37(1), 43-46.

Taylor, W., and Nimis, P. (1998) A single-pyroxene thermobarometer for lherzolitic Cr-diopside and its application in diamond exploration. 7th International Kimberlite Conference, Extended Abstracts. Cape Town: University of Cape Town.

Taylor, L., and Liu, Y. (2009) Sulfide inclusions in diamonds: not monosulfide solid solution. Russian Geology and Geophysics, 50(12), 1201-1211

Tennant, S. (1797) On the nature of the diamond. By Smithson Tennant, Esq. FRS. Philosophical Transactions of the Royal Society of London, 87, 123-127.

Walter MJ, Kohn SC, Araujo D, Bulanova GP, Smith CB, Gaillou E, Wang J, Steele A, Shirey SB (2011) Deep mantle cycling of oceanic crust; evidence from diamonds and their mineral inclusions. Science 334, 54-57.

Webb, S.A.C., and Wood, B.J. (1986) Spinel-pyroxene-garnet relationships and their dependence on Cr/Al ratio. Contributions to Mineralogy and Petrology, 92(4), 471-480.

Zhang Y (1998) Mechanical and phase equilibria in inclusion-host system. Earth Planet Sci Lett 157, 209-222.

2. A new micro-furnace for in situ high-temperature single-crystal X-ray diffraction measurements

M. Alvaro,[a*] R. J. Angel,[b] C. Marciano,[a] S. Milani,[b] L. Scandolo,[a] M. L. Mazzucchelli,[a] G. Zaffiro,[a] G. Rustioni,[a] M. Briccola,[c] M. C. Domeneghettia and F. Nestola[b]

[a]Department of Earth and Environmental Sciences, University of Pavia, Pavia, Italy,

[b]Department of Geosciences, University of Padua, Padua, Italy

[c]Department of Design, Polytechnic University of Milan, Milan, Italy.

In Journal of Applied Crystallography (2015), vol. 48., p.p. 1192-1200

ABSTRACT

A new micro-furnace equipped with an H-shaped resistance heater has been developed to conduct in situ single-crystal X-ray diffraction experiments at high temperature. The compact design of the furnace does not restrict access to reciprocal space out to $2\theta = 60\ \theta$. Therefore, unit-cell parameters and intensity data can be determined to a resolution of 0.71 A ° with Mo radiation. The combined use of mineral phases with well characterized lattice expansion (e.g. pure Si and SiO2 quartz) and a small-diameter (0.025 mm) K-type thermocouple allowed accurate temperature calibration from room temperature to about 1273 K and consequent evaluation of thermal gradients and stability. The new furnace design allows temperatures up to about 1273 K to be reached with a

thermal stability better than ±5 K even at the highest temperatures. Measurements of the lattice thermal expansion of pure silicon (Si), pure synthetic grossular garnet ($Ca_3Al_2Si_3O_{12}$) and quartz (SiO_2) are presented to demonstrate the performance of the device. Its main advantages and limitations and important considerations for using it to perform high-temperature diffraction measurements are discussed.

INTRODUCTION

Elastic properties reflect the nature of atomic bonding and allow the retrieval of crucial information about the physical, chemical and mechanical behaviour of materials. This explains the strong and increasing interest in quantifying elastic properties of materials in several scientific fields, including materials sciences, solid-state physics, chemistry and geosciences. High-temperature and high-pressure experiments also provide fundamental constraints for understanding and modelling the Earth's interior through the investigation of the physical properties of minerals. However, quantifying these physical properties (e.g. compressibility, thermal expansion etc.) even for common mineral phases remains quite challenging, mostly because of the many experimental limitations. In this work we consider high-temperature apparatus used in combination with single-crystal X-ray diffraction. It seems obvious that high-temperature devices for in situ measurements should provide the most controlled isothermal environment possible across the entire sample. It is also intuitive that, in general, thermal gradients across the sample will increase as the temperature increases. Even if the small isothermal volume required for single-crystal X-ray diffraction experiments makes such phenomena almost negligible, the furnace should also be designed to reduce thermal gradients by including a large thermal mass that encloses the sample. In the quest for these goals, several high-temperature devices

have been developed and have undergone significant developments in the past half century (e.g. Goldschmidt, 1964; Nukui et al., 1972; Viswamitra et al., 1974; Yamanaka, 1983; Hazen & Finger, 1982; Lorenz et al., 1993; Scheufler et al., 1997; Peterson, 1992; Estermann et al., 1999; Molin et al., 2001; Resel et al., 2003; Kruger & Breil, 2009). So far, several heating systems that make use of different physical heat transfer pathways (e.g. conduction, radiation, convection etc.) have been built, including conventional resistance heaters (e.g. Hazen & Finger, 1982; Brown et al., 1973; Swanson & Prewitt, 1986), mirror heating (Lorenz et al., 1993) and gas flow furnaces (Nukui et al., 1972; Smyth, 1972; Tuinstra & Storm, 1978; Yamanaka, 1983; Tsukimura et al., 1989; Scheufler et al., 1997; Peterson, 1992). Because of the progress made in the development of lasers and X-ray, neutron and magnetic sources it is now at least feasible to perform experiments in situ at high temperature (HT), high pressure (HP) and HT–HP on samples of millimetre or micrometre size [crystals, glasses and liquids; see Shen and Wang, (2014), Neuville et al., (2014) for reviews].

However, these solutions often lead to complex furnace designs that result in restricted access to reciprocal space or significant attenuation of the incident or diffracted beam intensity (with consequent reduction of the accuracy and/or precision in the lattice parameter determination), a decrease of the thermal stability while performing the measurements, and a lack of accuracy and/or precision in the temperature determination. At very high temperatures (higher than 1273 K)

these issues combine to make it difficult to use conventional furnaces. Indeed, it is still extremely challenging to achieve even temperatures of the order of 1273 K without compromising either the thermal stability and/or the accuracy and precision in the lattice and structure determination (e.g. Redhammer et al., 2010; Alvaro et al., 2011; Gatta et al., 2014; Ferrari et al., 2014; Pandolfo et al., 2014; Arletti et al., 2013; Scandolo et al., 2015). Here we present a newly developed H-shaped Pt Pt/Rh resistance micro-furnace for in situ hightemperature single-crystal X-ray diffraction measurements that is designed to perform high-temperature measurements up to 1273 K. The furnace has been built starting from the design proposed by Brown et al. (1973) and modified to work in combination with the eight-position centring protocol available in the SINGLE diffractometer control software (Angel & Finger, 2011) without restricting access to reciprocal space, attenuating the incident or diffracted beam over a reasonable range of 2θ, or compromising thermal stability and ccuracy and precision in lattice parameter determination.

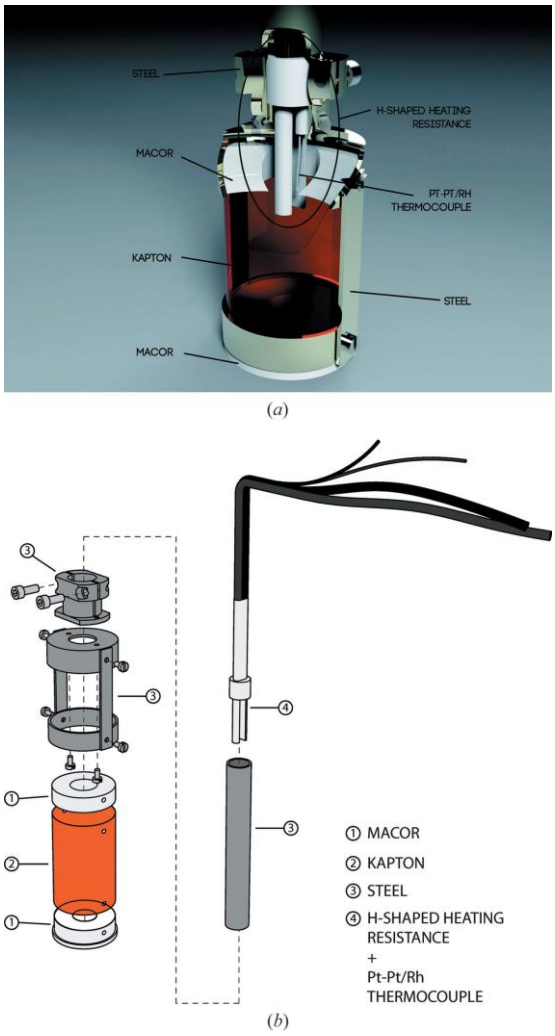

Fig. 1 Overview of the furnace with the main components identified. (a) Three dimensional rendering and (b) exploded view.

DESIGN AND CALIBRATION

The newly designed furnace is composed of four main units as shown in Fig. 1: the heaters, the mounting plates, the thermal radiation enclosure and the water cooling system, which will be described in detail below. Each of these units is independent of one another so that they can be easily replaced or modified to accommodate experimental needs.

Heaters

The furnace has been designed to be used with four-circle Eulerian geometry diffractometers as it can be easily mounted on the ’-axis counter-bearing (see Fig. 2a). In our particular case, the micro-furnace with its mounting system has been installed on a Huber model 424/511.1 four-circle diffractometer. The heater itself has been formed from a Pt–Rh spiral wire resistance arranged in an H shape and enclosed in an alumina half-tube to decrease the heat loss towards the outer part of the furnace (see Fig. 3). The resistance is held in place inside the half-tube using alumina cement as shown in Fig. 3. A Pt– Pt/Rh thermocouple is placed in between the two heating elements as close as possible to the furnace hot spot. The heaters are controlled with a Eurotherm power unit which uses the thermocouple output to control power supplied to the furnace elements.

Mounting system

As the sample-to-heater distance is one of the largest causes of differences between the reading of the furnace thermocouple and the actual temperature experienced by the crystal during the experiment, the mounting system is a crucial part of our new furnace. It must provide mechanical stability while minimizing heat conduction away from the furnace. Our mounting system holds the entire heating system on the goniometer by attaching to the χ counter-bearing. It consists of a circular steel plate attached to a lower steel plate that allows micrometric adjustments of the heaters along the diffractometer Cartesian axes X and Z, labelled according to Busing & Levy (1967) (see Fig. 2). These movements, checked by visual observation with the optical microscope of the diffractometer (i.e. the same microscope used for crystal centering), allow fine tuning of the resistance–sample distance in the two directions. Such micrometric control of the resistance position (and therefore also the thermocouple position), together with accurate centering of the crystal (see below), guarantees extremely high reproducibility of the calibrated temperature.

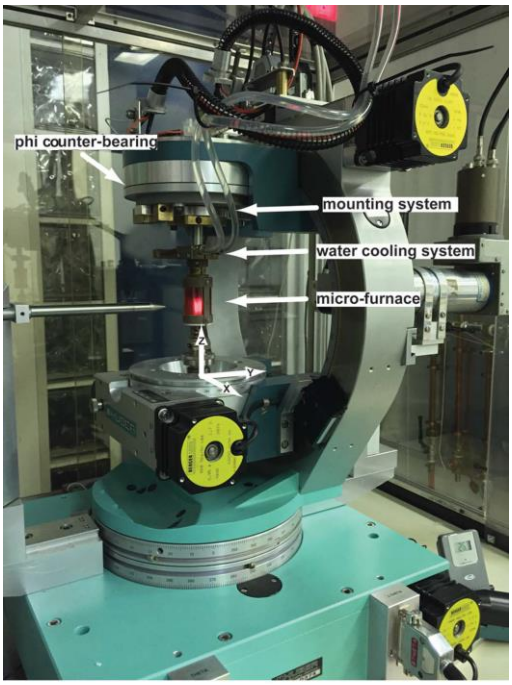

(*a*)

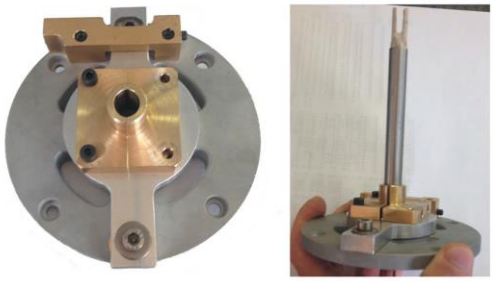

(*b*)

Fig. 2 (a) Diffractometer with micro-furnace installed on the φ counter-bearing. The water cooling system and water tubes are installed at their working positions. Arrows labelled as X, Y, Z represent both the diffractometer Cartesian system according to Busing & Levy (1967) and the furnace centring adjustments as explained in the text. (b) Furnace mounting system (left) viewed from the bottom and (right) from the side.

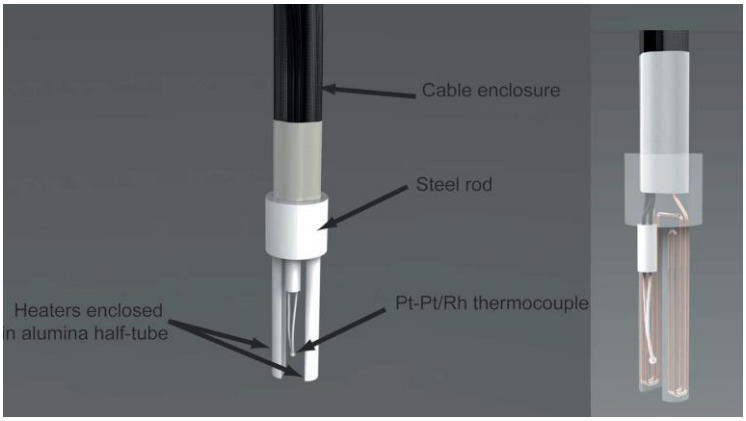

Fig. 3 Heater close-up view. Thermocouple length has been exaggerated for the purposes of illustration. The magnified open view illustrates the placement of the resistance inside the alumina half-tube. The heaters have been built using a Pt/Rh 10% resistive heater with a diameter of 0.02"(0.508 mm) and length of 100 mm. RT resistance 0.1 θ.

Enclosure

A steel cylindrical cage, 8 cm diameter, filled at the top and bottom with two machinable discs of ceramic material (Macor) and closed at the side with a thin (0.025 mm thick) Kapton film is used to prevent heat loss towards the outside of the furnace (see Fig. 4). The Kapton film, stable up to 673 K, significantly reduces the heat loss through radiation and convection without adding significant uncertainties to the lattice parameter determination (e.g. Svensson, 1983). The water cooling system, described in more detail below, guarantees that the Kapton film never reaches 673 K even at the highest temperatures of 1273 K achieved during our test experiments. The Macor discs reduce heat transfer to the φ counter-bearing (at the top) and to the goniometer head (at the bottom). Two holes have been drilled into the ceramic discs, as shown in Fig. 4, to allow fitting of the heater cables at the top and the insertion of the sample crystal from the bottom.

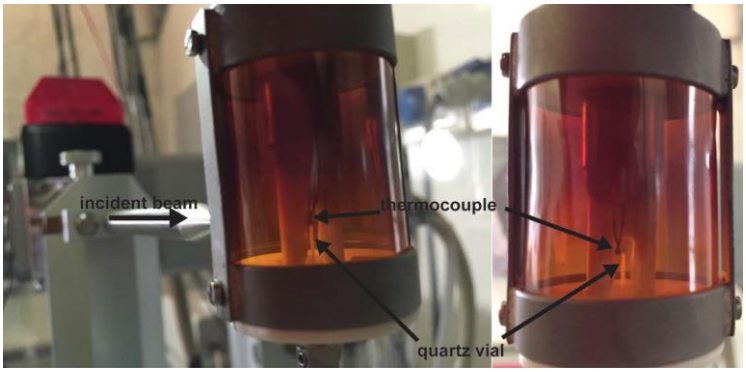

Fig. 4 Furnace close view with vial aligned with the beam and close-up view of the furnace along the beam direction showing the vial containing the crystal and thermocouple aligned.

Water cooling system

A water cooling system (with a water flow of about 1 l min^{-1}) has been added to the design in order to prevent heat transfer through the steel cylinder containing the heater cables (see Fig. 5). The cooling system further prevents heat transfer to the φ counter-bearing. It is also in contact with the steel cage, which is therefore also cooled, thereby increasing the thermal gradient at the interface between the inside and outside of the cage. The result is a very high thermal gradient from 1273 K inside the furnace at the hot spot to 373 K in the outer part of the steel cage. The concentration of the greatest thermal gradient at the interface between the inner and outer part of the furnace, but not inside the heater, contributes to the temperature stability at the hot spot.

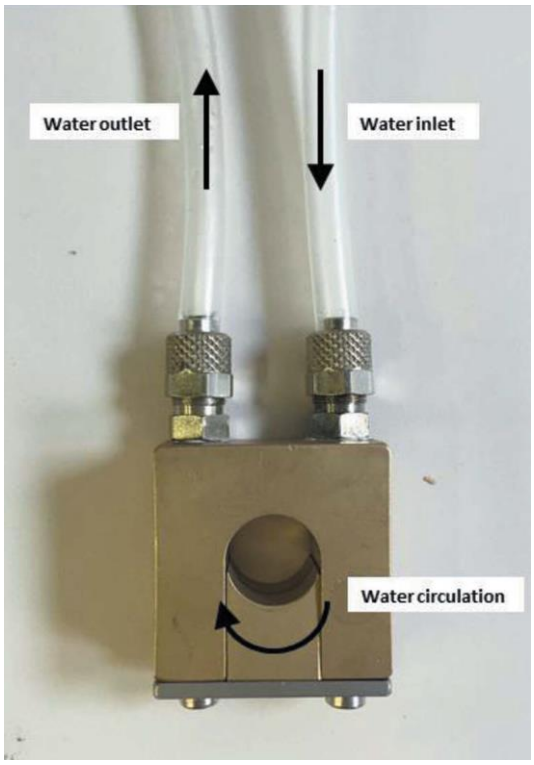

Fig. 5 Water cooling system with inlet and outlet water tubes and circulating ring.

Sample mounting

The single crystal is usually mounted inside a quartz vial with a size of typically 0.3–0.7 mm inner diameter and 24–28 mm long, which is closed at the top using an oxy-methane flame. In order to avoid any mechanical stress, the crystal is kept in position within the vial using quartz wool (see Fig. 6). In the case of samples containing elements that can oxidize with temperature (in earth sciences, typically iron-rich samples), a small piece of an iron or other metal wire can be loaded inside the vial about 1.5 mm below the crystal. This scavenges any free oxygen in the vial and prevents oxidation of the Fe^{2+} in the crystal during heating. The vial containing the sample is then alternately washed with Ar flux and evacuated [at about 4×10^{-2} mbar (1 mbar = 100 Pa)] before final sealing. The vial is subsequently mounted into a standard short metal goniometer head (see Fig. 6).

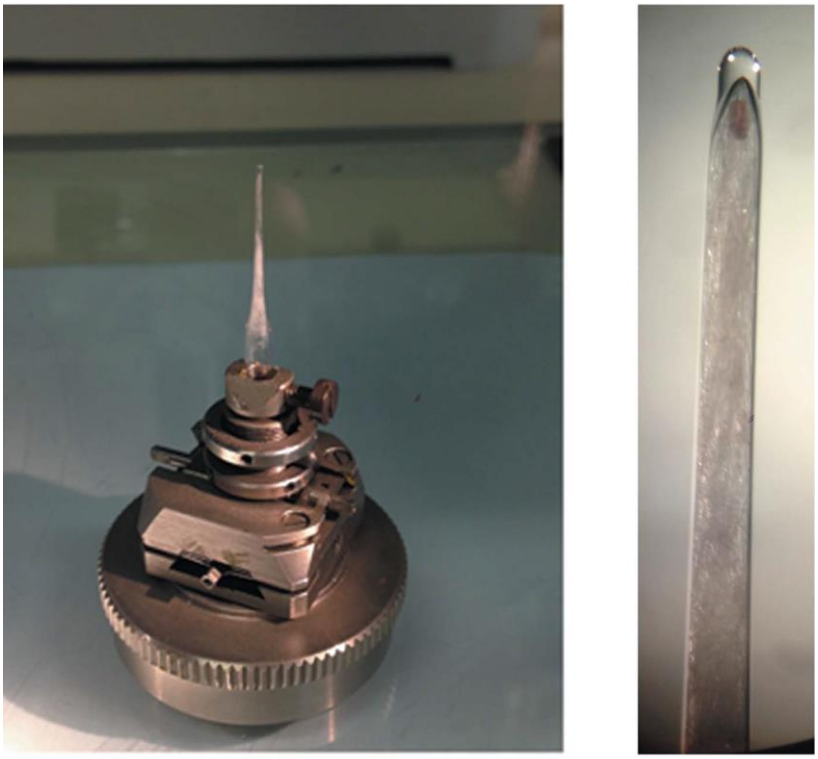

(*a*) (*b*)

Fig.6 (a) Vial mounted on the goniometer head; (b) sample mounted in the vial and held in position with quartz wool.

DIFFRACTOMETER OPERATIONS

The compact design of the furnace together with the long collimator–sample–detector distance allows diffraction measurements to be made up to 2 θ = 60 θ (i.e. resolution up to 0.71 Å with Mo radiation) with no further restrictions on any diffractometer angular movements or reciprocal-space access, with the diffractometer operated in the normal 'bisecting' mode. Above 2θ = 60° the furnace heater elements start to restrict access to reciprocal space, and increased access can be achieved if the ω circle is moved from the bisecting position. In principle, the furnace can be operated over the full range of rotation of the χ circle, which would allow eight-position centering to be used to eliminate the effects of crystal offsets and diffractometer aberrations from the refined peak positions (e.g. King & Finger, 1979). However, the furnace becomes inverted at χ > 90° and the convective air flow through the furnace assembly is consequently reversed, leading to degradation of the temperature stability. This, in combination with a desire to minimize the possibility of entanglement of the electrical cables and cooling-water pipes during diffractometer motions, has led us to restrict the χ-circle movements to between -90 and +90°. This allows us to only access four of the eight equivalent positions of one reflection with a point detector diffractometer. This would normally result in a decrease in the precision of the cell parameter measurements (see e.g. Angel et al., 2000). However, since the operation of mounting and dismounting the furnace does not require the crystal sample to be removed, we first measure the crystal at room temperature and pressure conditions without the furnace, and use the crystal offsets determined from a full eight-position centering (King & Finger, 1979) to move the crystal to the diffraction center of the goniometer. Only afterwards is the furnace mounted and centered at the pre-calibrated distance from the sample crystal. One last improvement in stability is achieved by either minimizing the number of large movements of the goniometer χ circle (by optimizing the order in which reflections are measured), or by imposing a waiting time before diffraction measurements are restarted after large χ movements. We have found that a pause of no more than 60 s after changes in χ of more than 45° is sufficient to ensure a temperature stability of ±5 K.

TEMPERATURE CALIBRATION METHOD

The temperature calibration has been undertaken by combining iterative measurements performed with a standard small diameter (i.e. 0.25 mm) thermocouple mounted in the same conditions as the sample, together with determination of the lattice parameters for materials with known thermal expansion behaviour. This procedure has the main advantage that the temperature calibration can be obtained with a large number of measurements over the large operating range of the furnace to 1273 K, and also allows the waiting time for the χ movements to be calibrated as a function of temperature. At first, in order to obtain a preliminary temperature correction, a small thermocouple was mounted in a quartz vial in the same conditions as those used for the crystal (i.e. mounted on a standard metal goniometer head, inside a 0.5 mm inner diameter quartz vial, optically centered on the X-ray beam at the crystal position). Fig. 7 shows the limitation in such a temperature calibration method. Above 573 K the secondary thermocouple data (Tfurnace) are obviously wrong as the temperature reading is clearly affected by thermal conduction (see open symbol in Fig. 7). Therefore, only the data below 573 K could be used for a first temperature correction. Linear fitting of the observed Tdisplay (i.e. temperature reading on the power controller) against Tfurnace (i.e. temperature reading on the secondary thermocouple) yielded the following equation:

$$T_{display} = 2.58(76) + 0.768\ (6)\ T_{furnace}\ (R^2 = 0.9995). \quad (1)$$

For the purposes of this preliminary fitting only a restricted range of temperature has been used. However, we believe that this calibration method represents a great improvement with respect to previously used methods such as using known melting points of pure salts. Measuring the melting points of pure salts often leads to large uncertainties because of three major issues: (i) measurements are strongly dependent on the experimental judgement that the very first drop of melt has been produced; (ii) melting points of salts are strongly dependent on their hydrous content which is extremely difficult

to control; (iii) because of the thermal gradient, the temperature experienced by the powdered salt, which occupies several millimeters inside the vial far from the hot spot, may not be accurate. Our preliminary calibration has been further constrained using the phase transition of quartz [as determined by Carpenter et al., (1998)] and the unit-cell volume variation of pure silicon [as determined by several authors and reassessed by Keppler (1988)], as explained in detail in the following section.

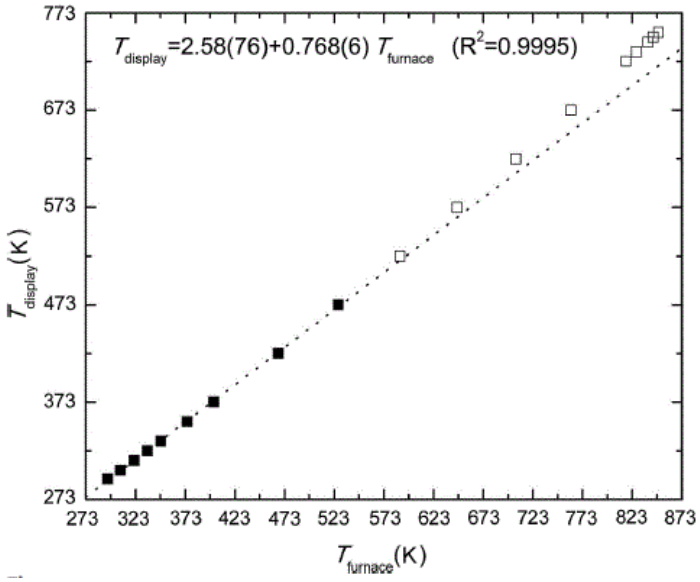

Fig. 7 Furnace calibration ($T_{display}$ against $T_{furnace}$) performed using the secondary thermocouple mounted in the vial at the sample position. Filled black squares represent data included in the linear fit. Open black squares represent data not considered for fitting purposes because they are affected by thermocouple heat conduction effects (see text for further details).

EXAMPLES

The example measurements reported here have been performed using a Huber model 424/511.1 four-circle Eulerian cradle diffractometer (Fig. 2a) equipped with a point detector. The X-ray source is a conventional sealed tube with an Mo target operated at 40 kV and 30 mA to produce Mo Kα radiation. There are no filters, monochromators or other optics in the beam path to ensure a clean and homogeneous intensity profile of the beam as a function of wavelength, and hence reproducible diffraction rocking curves which are essential for precise unit-cell parameter measurements (e.g. Angel et al., 2000). The diffractometer is controlled with the SINGLE software (Angel & Finger, 2011) which has been modified to implement the measurement procedures of restricted χ motion, optimized reflection measurement order and pauses after large χ motions, required to optimize the precision (see chapter 2.6). SINGLE determines the Bragg angles of diffraction from the crystal by full-profile fitting of the rocking curves of the crystal in four or eight positions (cf. King & Finger, 1979) and fitting the corrected angles by full-matrix vector least squares (Ralph & Finger, 1982). For each of the experiments described below, a preliminary optical centering of the crystal has been followed by a complete measurement of no less than 20 reflections using the eightposition centering method. Then the crystal position has been adjusted to the diffraction center of the goniometer by using the crystal offsets determined during the eight-position measurements. Only afterwards has the furnace been mounted and centered at the calibrated distance from the sample crystal.

Quartz

Quartz has been extensively investigated at both high pressures and high temperatures and extremely reliable HP and HT data have been published so far (e.g. Le Chatelier, 1889; Bachheimer, 1980; Salje et al., 1992; Angel et al., 1997; Carpenter et al., 1998; Raz et al., 2002; Calderon et al., 2007). Moreover, the quartz α–β phase transition at high temperature and ambient pressure means it has very high thermal expansion below 846 K and it provides a fixed point at this transition temperature. Therefore, in order to better constrain and evaluate our preliminary calibration of the furnace, the unit-cell volume of quartz was measured up to the α–β phase transition. A single crystal of quartz (SiO2) was selected because of its sharp diffraction profile and absence of twinning. The selected crystal was ground with the apparatus described by Cámara et al. (2012) and reduced to a spherical shape of about 200 mm radius and then mounted in the quartz

vial as described above. Lattice parameters were determined by measuring the positions of not less than 20 reflections at seven temperatures up to the trigonal ! hexagonal phase transition. The measured lattice parameters and volume are reported in Table 1. This procedure allowed us to check the reliability of the calibration undertaken with just the secondary thermocouple by monitoring the unit-cell volume of SiO2 across the phase transition. Small discrepancies between our current data and those reported by Carpenter et al. (1998) can be observed mostly at the phase transition temperature (see Fig. 8). As a matter of fact, we could reliably bracket the transition at 823 K (Tfurnace) against the 846 K reported by Carpenter et al. (1998). Across the phase transition from P_{6422} (or P_{6222}) to P_{3121} (or P_{3221}), the intensity change of reflections such as 111 was constantly monitored (i.e. keeping the shutter open while changing the temperature).

The intensity change of such reflections was evaluated during both heating and cooling in order to reliably bracket the phase transition, avoiding the 1.5 K region where experimental work by Bachheimer (1980) has shown the existence of an intermediate phase between α and β quartz. The discrepancy between the observed and the actual phase transition temperature, clearly caused by an offset in our preliminary calibration, has been taken into account by including these new data into our fitting, therefore adding another strong constraint. A linear fit of the entire data set, including the new phase transition data points (see Fig. 9), yielded the following equation:

$$T_{display} = 3.03(57) + 0.763(2)\, T_{furnace}\ (R^2 = 0.99989). \quad (2)$$

Table 1 Quartz unit-cell volume measured upon heating.

$T_{display}$ (K)	$T_{furnace}$ (K)	Volume (Å^3)
292	294	113.05 (2)
405	442	113.74 (2)
515	585	114.59 (2)
668	784	116.52 (2)
692	815	117.40 (2)
713	842	118.04 (2)
736	872	118.09 (2)
692	815	117.40 (2)
713	842	118.04 (2)
736	872	118.09 (2)

Note: standard deviations are given in parentheses.

.

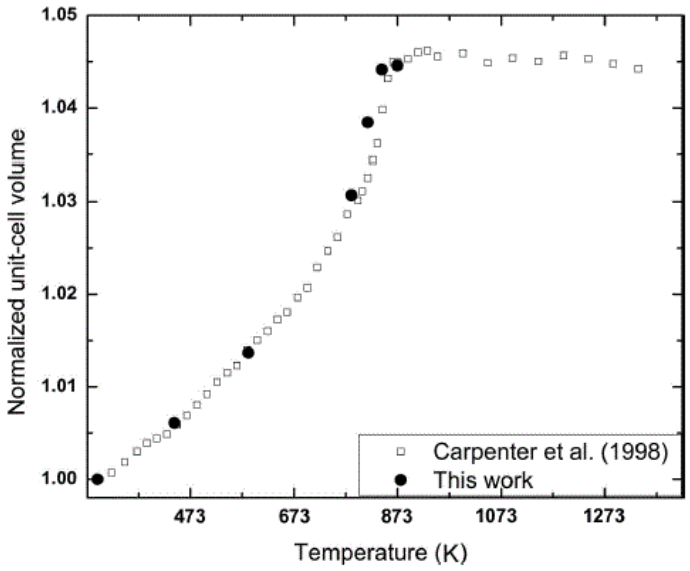

Fig. 8 Quartz unit-cell volume as a function of temperature. The temperature was obtained by linear fit and extrapolation of the data obtained with a secondary thermocouple.

Silicon

The thermal expansion of silicon has been extensively measured (e.g. Lyon et al., 1977; Okada & Tokumaru, 1984; Keppler, 1988; Bergamin et al., 1997; Watanabe et al., 2004; Magunov et al., 2014), mainly because it is of great interest for the semiconductor industry. After Keppler's reassessment of the available silicon thermal expansion data which turned out to be in excellent agreement with the calculated values (Keppler, 1988), Si was also widely adopted as a standard for temperature calibrations (e.g. Benna et al., 2000; Resel et al., 2003). Certainly, the high symmetry (cubic), the simple composition (pure Si) and the high-temperature melting point (1687 K) make silicon a good candidate as a reference standard for thermal expansion experiments (Keppler, 1988). Therefore, after the previous temperature calibrations the unit-cell volume of silicon was measured

at ten different temperatures from room temperature up to about 1073 K (see Figs. 9, 10 and Table 2). These measurements allowed the further constraint of the T calibration as:

$$T_{display} = 2.45(72) + 0.769\ (2)\ T_{furnace}\ (R^2 = 0.9999). \quad (1)$$

It is clear that within fitting errors the three equations are indistinguishable from one another. The largest differences are in the intercept, which however would produce constant offsets smaller than 0.5 K that are still within estimated uncertainties in the temperature values (i.e. 5 K).

Table 2 Silicon lattice parameters as a function of temperature.

$T_{display}$	$T_{furnace}$	*a* (Å)	Volume (Å^3)
294	297	5.4303 (4)	160.127 (35)
297	301	5.4309 (5)	160.185 (44)
313	322	5.4312 (5)	160.210 (41)
333	348	5.4316 (4)	160.247 (33)
413	453	5.4337 (4)	160.433 (36)
493	557	5.4359 (4)	160.627 (39)
573	662	5.4381 (4)	160.822 (33)
653	767	5.4403 (4)	161.019 (32)
732	871	5.4424 (5)	161.203 (45)
812	976	5.4446 (7)	161.393 (63)
892	1080	5.4469 (9)	161.601 (76)
1011	1236	5.4509 (8)	161.962 (70)

Note: standard deviations are given in parentheses. Furnace temperatures (T_f) have been calculated from the unit-cell volumes measured in this study using the thermoelastic coefficients [$\alpha_{0,300} = 1.02\times10^{-5}$ K^{-1} with $\alpha_0 = 0.92\ (3)\times10^{-5}$ K^{-1}, $\alpha_1 = 0.34\ (4) \times 10^{-8}$ K^{-2} and α_2 fixed to 0 K] obtained from the data of Keppler (1988) fit to a Fei-type EoS.

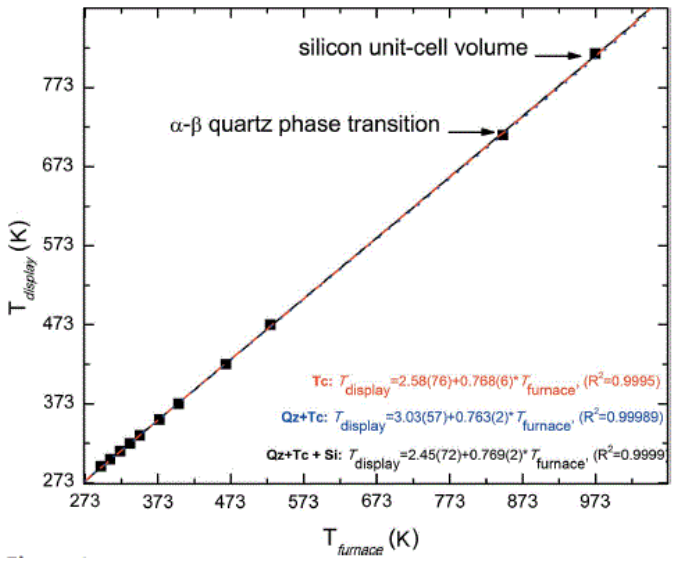

Fig. 9 Temperature calibration (Tdisplay agaist Tfurnace). The three curves represent the fits obtained only with the secondary thermocouple (Tc, red solid line), adding the quartz phase transition (Qz + Tc, blue dotted line) and adding the silicon unit-cell volume for one single temperature (Qz + Tc + Si, black dashed line).

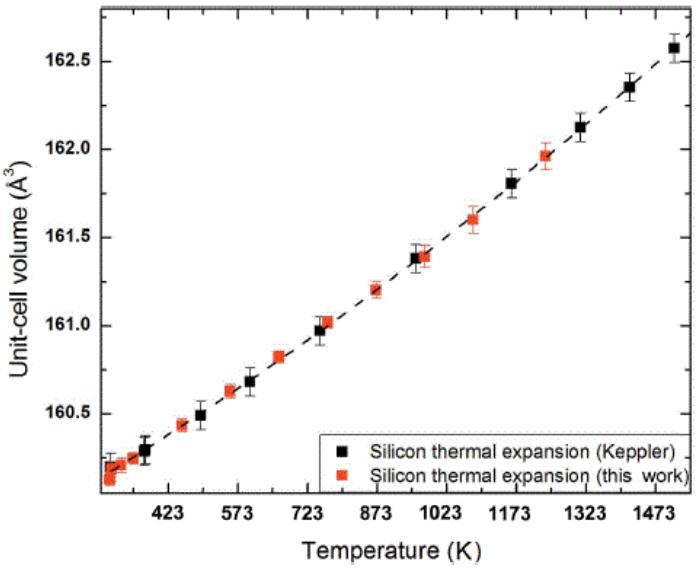

Fig. 10 Silicon unit-cell volume against temperature measured in the range 300– 1100 K. Filled red squares represent our data and filled black squares are literature data (Keppler, 1988) that allowed us to obtain the actual temperature for each measured unit-cell volume. Even when using the temperature calibration obtained only using the secondary thermocouple and refined by adding the quartz phase transition, our high temperature data points agree extremely well with those published by Keppler (1988).

Grossular

The first complete experiment not devoted to calibration purposes was performed on a synthetic pure grossular garnet ($Ca_3Al_2Si_3O_{12}$) crystal synthesized at the Bayerisches Geoinstitut in a multi-anvil apparatus as described by Milani et al., 2015).

Determination of the equations of state (EoS) for grossular along with those available for the other aluminosilicate garnet end-members (e.g. pyrope, almandine; see Milani et al., 2015 for a review) is fundamental for a correct estimate of the thermoelastic properties for intermediate composition such as those typically occurring for garnet inclusions trapped in diamonds. These thermal EoS can then be used together with those determined at high pressure in order to estimate the entrapment pressure for garnet inclusions in diamonds using the recently developed 'elastic geobarometer' (Angel, Mazzucchelli et al., 2014; Angel, Alvaro et al., 2015; Angel, Nimis et al., 2015).

The thermal expansion behaviour of grossular has been investigated by determining the lattice parameters from measurements of not less than 25 reflections at 18 different temperatures from room temperature up to 1073 K with steps of 50 and 100 K upon heating and cooling, respectively. The unit-cell volume expands linearly with temperature (see Fig. 11a and Table 3). The high reliability of the measured data is evident from the good reproducibility of the measurements upon increasing and decreasing the temperature (see Fig. 11a) and is further confirmed when our data are compared with several other data sets (e.g. Thieblot et al., 1998; Skinner, 1956), including some very recent ones (e.g. Du et al., 2015). The very good agreement between our room-temperature unit-cell volume and that reported by Bosenick & Geiger (1997) for the low-temperature regime down to 40 K for a pure end-member grossular garnet allowed the combination of the two data sets in order to fit thermal pressure EoS (for further details, see Angel, Gonzalez-Platas & Alvaro, 2014). The room-temperature thermal expansion coefficient ($\alpha_{0,303K}$) has been determined as 2.55×10^{-5} K^{-1} for $K_0 = 5$ (as determined by Milani et al., 2015) with a θ_E of 500 K, and its behaviour with temperature is reported in Fig. 11(c).

Table 3 Pure synthetic grossular unit-cell volume and a lattice data measured upon heating and cooling.

T (K)	*a* (Å)	Volume (Å^3)
293	11.8499 (5)	1663.98 (20)
303	11.8503 (6)	1664.15 (23)
323	11.8525 (6)	1665.04 (25)
373	11.8570 (6)	1666.95 (24)
423	11.8627 (7)	1669.36 (28)
473	11.8673 (7)	1671.31 (31)
523	11.8716 (12)	1673.12 (49)
573	11.8776 (6)	1675.65 (26)
623	11.8826 (5)	1677.78 (22)
673	11.8880 (5)	1680.08 (22)
723	11.8934 (5)	1682.37 (23)
773	11.8984 (5)	1684.47 (23)
823	11.9041 (6)	1686.92 (23)
873	11.9088 (6)	1688.90 (25)
923	11.9139 (5)	1691.08 (23)
973	11.9193 (5)	1693.38 (22)
1023	11.9248 (5)	1695.71 (22)
1073	11.9297 (5)	1697.81 (22)
998	11.9224 (5)	1694.69 (21)
898	11.9114 (5)	1690.01 (22)
798	11.9009 (5)	1685.53 (22)
698	11.8905 (5)	1681.14 (21)
523	11.8726 (5)	1673.55 (21)
448	11.8648 (5)	1670.26 (22)
348	11.8548 (5)	1666.02 (21)
303	11.8505 (5)	1664.20 (20)

Note: standard deviations are given in parentheses.

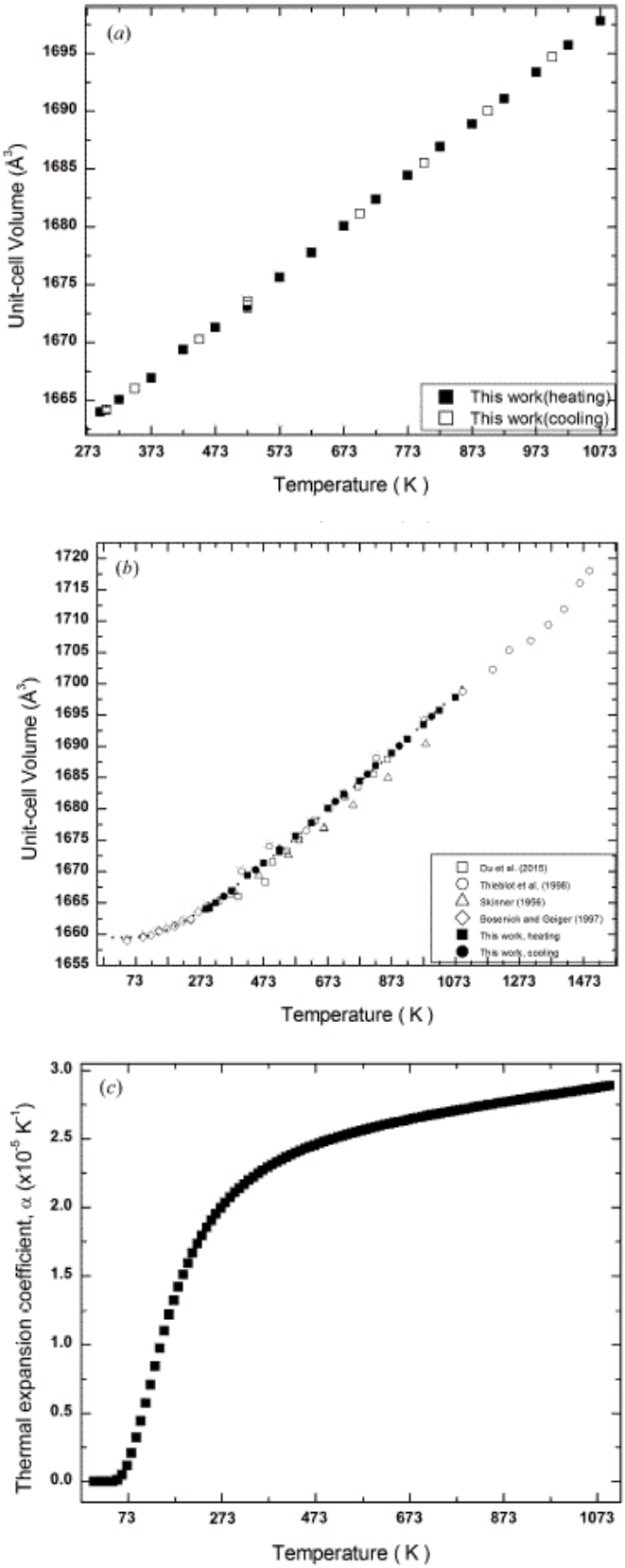

Fig. 11 Grossular garnet thermal expansion. (a) Unit-cell volume evolution with T as measured in this work during heating (filled squares) and cooling (open squares). (b) Unit-cell volume obtained in this work (filled symbols) compared with values from the literature (open triangle: Skinner, 1956; open diamond: Bosenick & Geiger, 1997; open circle: Thieblot et al., 1998; open square: Du et al., 2015). (c) Calculated thermal expansion coefficient (α) as a function of temperature.

CONCLUSIONS

The new furnace for high-temperature single-crystal X-ray diffraction experiments developed for combined use with the new version of the SINGLE diffractometer control software (Angel & Finger, 2011) allows the measurement protocols (i.e. the eight-position centering procedure) for high-pressure diffraction experiments to be applied to high-temperature experiments without compromising the furnace performance.

These protocols allow the determination of individual unit-cell edges of good-quality single crystals to 1 part in 30 000, corresponding to a precision in unit-cell volumes of 1 part in 10 000, identical to that achieved for high-pressure measurements. The relatively low operating and manufacturing costs, improved performance (i.e. high thermal stability and wide reciprocal-space access) and modular design make this furnace design easily customizable and it can therefore be easily adapted to different instruments and experimental needs.

ACKNOWLEDGEMENTS

The authors wish to thank K. Chapman and two anonymous reviewers for their fruitful comments and suggestions. This work has been supported by an ERC starting grant 307322 to F. Nestola (project INDIMEDEA). We thank I. G. Wood (University College London) for the long-term loan of the Huber diffractometer that enabled us to make these developments. We thank V. Tazzoli for his constant help and fruitful suggestions. Claudio Scagliotti from the INFN unit of Pavia and Pietro Zandalazini from the Chemistry Department of the University of Pavia are kindly acknowledged for their crucial suggestions and technical support.

References

Alvaro, M., Cámara, F., Domeneghetti, M., Nestola, F., and Tazzoli, V. (2011) H*T* $P2_1/c$–$C2/c$ phase transition and kinetics of Fe^{2+}–Mg order–disorder of an Fe-poor pigeonite: implications for the cooling history of ureilites. Contributions to Mineralogy and Petrology, 162(3), 599-613.

Angel, R.J., Allan, D.R., Milletich, R., and Finger, L.W. (1997) The use of quartz as an internal pressure standard in high-pressure crystallography. Journal of Applied Crystallography, 30, 461-466.

Angel, R., Alvaro, M., Nestola, F., and Mazzucchelli, M. (2015) Diamond thermoelastic properties and implications for determining the pressure of formation of diamond-inclusion systems. Russian Geology and Geophysics, 56(1-2), 211-220.

Angel, R., Downs, R., and Finger, L. (2000) High-temperature–high-pressure diffractometry. Reviews in Mineralogy and Geochemistry, 41(1), 559-597.

Angel, R.J., and Finger, L.W. (2011) SINGLE: a program to control single-crystal diffractometers. Journal of Applied Crystallography, 44(1), 247-251.

Angel, R.J., Alvaro, M., and Gonzalez-Platas, J. (2014) EosFit7c and a Fortran module (library) for equation of state calculations. Zeitschrift für Kristallographie-Crystalline Materials, 229(5), 405-419.

Angel, R.J., Mazzucchelli, M.L., Alvaro, M., Nimis, P., and Nestola, F. (2014) Letter. Geobarometry from host-inclusion systems: The role of elastic relaxation.

Angel, R., Nimis, P., Mazzucchelli, M., Alvaro, M., and Nestola, F. (2015) How large are departures from lithostatic pressure? Constraints from host–inclusion elasticity. Journal of Metamorphic Geology.

Arletti, R., Vezzalini, G., Quartieri, S., Cámara, F., and Alvaro, M. (2013) A new framework topology in the dehydrated form of zeolite levyne. American Mineralogist, 98(11-12), 2063-2074.

Bachheimer, J. (1980) An anomaly in the β phase near the α-β transition of quartz. Journal de Physique Lettres, 41(23), 559-561.

Benna, P., Tribaudino, M., and Bruno, E. (2000) $I\bar{1}$-I2/c ferroelastic phase transition in the Ca0. 2Pb0. 8Al2Si2O8 feldspar as a function of temperature. Mineralogical Magazine, 64(2), 285-290.

Bergamin, A., Cavagnero, G., Mana, G., and Zosi, G. (1997) Lattice parameter and thermal expansion of monocrystalline silicon. Journal of Applied Physics, 82(11), 5396-5400.

Brown, G., and Wechsler, B. (1973) Crystallography of pigeonites from basaltic vitrophyre 15597. Lunar and Planetary Science Conference Proceedings, 4, p. 887.

Busing, W.R., Levy, H.A. (1967) Angle calculations for 3- and 4-circle X-ray and neutron diffractometers. Acta Crystallographica, 22(4), 457-464.

Calderon, E., Gauthier, M., Decremps, F., Hamel, G., Syfosse, G., and Polian, A. (2007) Complete determination of the elastic moduli of α-quartz under hydrostatic pressure up to 1 GPa: an ultrasonic study. Journal of Physics: Condensed Matter, 19(43), 436228.

Cámara, F., Gatta, G.D., Meven, M., Pasqual, D. (2012) Thermal expansion and high temperature structure evolution of zoisite by single-crystal X-ray and neutron diffraction. Physics and Chemistry of Minerals, 1-19 .

Carpenter, M.A,, Salje, E.K.H., Graeme-Barber, A., Wruck, B., Dove, M.T., Knight, K.S. (1998) Calibration of excess thermodynamic properties and elastic constant variations associated with the alpha <->beta phase transition in quartz. American Mineralogist, 83(1-2), 2-22.

Du, W., Clark, S.M., and Walker, D. (2015) Thermo-compression of pyrope-grossular garnet solid solutions: Non-linear compositional dependence. American Mineralogist, 100(1), 215-222.

Estermann, M., Reifler, H., Steurer, W., Filser, F., Kocher, P., Gauckler, L.J. (1999) A high-temperature furnace for X-ray diffraction with directly machined [alpha]-Al2O3 ceramic parts. Journal of Applied Crystallography, 32(4), 833-836.

Ferrari, S., Nestola, F., Massironi, M., Maturilli, A., Helbert, J., Alvaro, M., Domeneghetti, M.C., and Zorzi, F. (2014) In-situ high-temperature emissivity spectra and thermal expansion of C2/c pyroxenes: Implications for the surface of Mercury. American Mineralogist, 99(4), 786-792.

Gatta, G., Comboni, D., Alvaro, M., Lotti, P., Cámara, F., and Domeneghetti, M. (2014) Thermoelastic behavior and dehydration process of cancrinite. Physics and Chemistry of Minerals, 41(5), 373-386.

Goldschmidt, H.J. (1964) High-temperature x-ray diffraction techniques. International union of crystallography.

Hazen, R.M., Finger, L.W. (1982) High-temperature and high-pressure crystal chemistry. High-Pressure Researches in Geoscience, 151-176.

Keppler, U. (1988) Thermal expansion of silicon. Zeitschrift für Metallkunde 79(3):157-158.

King, H.E., Finger, L.W. (1979) Diffracted Beam Crystal Centering and Its Application to High-Pressure Crystallography. Journal of Applied Crystallography, 12(Aug), 374-378.

Krueger, H., and Breil, L. (2009) Computer-controlled high-temperature single-crystal X-ray diffraction experiments and temperature calibration. Journal of Applied Crystallography, 42(1), 140-142.

Le Chatelier, H. (1889) Sur la dilatation du quartz. Comptes Rendus, 108, 1046.

Lorenz, G., Neder, R., Marxreiter, J., Frey, F., Schneider, J. (1993) A mirror furnace for neutron diffraction up to 2300 K. Journal of Applied Crystallography, 26(5), 632-635.

Lyon, K., Salinger, G., Swenson, C., and White, G. (1977) Linear thermal expansion measurements on silicon from 6 to 340 K. Journal of Applied Physics, 48(3), 865-868.

Magunov, A., Zakharov, A., and Lapshinov, B. (2014) Measuring temperature of silicon monocrystals using spectral pyrometry. Russian Microelectronics, 43(3), 201-206.

Milani, S., Nestola, F., Alvaro, M., Pasqual, D., Mazzucchelli, M., Domeneghetti, M., and Geiger, C. (2015) Diamond–garnet geobarometry: The role of garnet compressibility and expansivity. Lithos, 227, 140-147.

Molin, G., Martignago, F., and Dal Negro, A. (2001) A new radiative microfurnace for X-ray single-crystal diffractometry. European Journal of Mineralogy, 13(3), 557-564.

Neuville, D.R., Hennet, L., Florian, P., and de Ligny, D. (2014) In situ high-temperature experiments. Reviews in Mineralogy and Geochemistry, 78(1), 779-800.

Nukui, A., Iwai, Si., Tagai, H. (1972) Gas Flame Heating Equipment Providing up to 2300° C for an X-Ray Diffractometer. Review of Scientific Instruments, 43(9),1299-1301.

Okada, Y., and Tokumaru, Y. (1984) Precise determination of lattice parameter and thermal expansion coefficient of silicon between 300 and 1500 K. Journal of Applied Physics, 56(2), 314-320.

Pandolfo, F., Cámara, F., Domeneghetti, M.C., Alvaro, M., Nestola, F., Karato, S.-I., and Amulele, G. (2015) Volume thermal expansion along the jadeite–diopside join. Physics and Chemistry of Minerals, 42(1), 1-14.

Peterson, R. (1992) A flame-heated gas-flow furnace for single-crystal X-ray diffraction. Journal of Applied Crystallography 25(5),545-548.

Ralph, R.L., and Finger, L.W. (1982) A Computer-Program for Refinement of Crystal Orientation Matrix and Lattice-Constants from Diffractometer Data with Lattice Symmetry Constraints. Journal of Applied Crystallography, 15(Oct), 537-539.

Raz, U., Girsperger, S., and Thompson, A.B. (2002) Thermal expansion, compressibility and volumetric changes of quartz obtained by single crystal dilatometry to 700 C and 3.5 kilobars (0.35 GPa). Eidgenössische Technische Hochschule (Zürich) Departement für Erdwissenschaften.

Redhammer, G.J., Cámara, F., Alvaro, M., Nestola, F., Tippelt, G., Prinz, S., Simons, J., Roth, G., and Amthauer, G. (2010) Thermal expansion and high-temperature $P2_1/c$–$C2/c$ phase transition in clinopyroxene-type $LiFeGe_2O_6$ and comparison to $NaFe(Si,Ge)_2O_6$. Physics and Chemistry of Minerals, 37(10), 685-704.

Resel, R., Tamas, E., Sonderegger, B., Hofbauer, P., and Keckes, J. (2003) A heating stage up to 1173 K for X-ray diffraction studies in the whole orientation space. Journal of Applied Crystallography, 36(1), 80-85.

Salje, E., Ridgwell, A., Guttler, B., Wruck, B., Dove, M., and Dolino, G. (1992) On the displacive character of the phase transition in quartz: a hard-mode spectroscopy study. Journal of Physics: Condensed Matter, 4(2), 571.

Scandolo, L., Mazzucchelli, M., Alvaro, M., Nestola, F., Pandolfo, F., and Domeneghetti, M. (2015) Thermal expansion behaviour of orthopyroxenes: the role of the Fe-Mn substitution. Mineralogical Magazine, 79(1), 71-87.

Scheufler, C., Engel, K., Kirfel, A. (1997) An improved gas-stream heating device for a single-crystal diffractometer. Journal of Applied Crystallography, 30(3),411-412.

Shen, G., and Wang, Y., (2014). Spectroscopic Methods in Mineralogy and Materials Sciences. Reviews in Mineralogy and Geochemistry, 78, 745–777.

Skinner, B.J. (1956) Physical properties of end-members of the garnet group. American Mineralogist, 41, 428-436.

Smyth, J. (1972) Simple heating stage for single-crystal diffraction studies up to 1000°C. American Mineralogist, 57, 1305-1309.

Svensson, C. (1983) Error in 2 from single-crystal diffractometers due to sample absorption in a divergent primary beam. Journal of Applied Crystallography, 16(5),573-575.

Swanson, D.K., Prewitt, C.T. (1986) A new radiative single-crystal diffractometer microfurnace incorporating MgO as a high-temperature cement and internal temperature calibrant. Journal of Applied Crystallography, 19(1).1-6.

Thiéblot, L., Roux, J., and Richet, P. (1998) High-temperature thermal expansion and decomposition of garnets. European Journal of Mineralogy, 7-16.

Tsukimura, K., Sato-Sorensen, Y., Ghose, S. (1989) A gas-flow furnace for X-ray crystallography. Journal of Applied Crystallography, 22(5), 401-405.

Tuinstra, Ft., Fraase Storm, G. (1978) A universal high-temperature device for single-crystal diffraction. Journal of Applied Crystallography, 11(4), 257-259.

Viswamitra, M., Shaikh, A., and Ramanuja, K.J. (2013) High temperature X-ray crystallography: devices for single crystal analysis. Journal of the Indian Institute of Science, 57(1), 1.

Watanabe, H., Yamada, N., and Okaji, M. (2004) Linear thermal expansion coefficient of silicon from 293 to 1000 K. International Journal of Thermophysics, 25(1), 221-236.

Yamanaka, T., (1983) Gas-flame heating system for single-crystal X-ray diffraction studies and temperature measurement. Journal of the Mineralogical Society of Japan 16(Special), 21-26.

3. Thermal expansion behavior of orthopyroxenes: the role of the Fe-Mn substitution

Scandolo L[1]., Mazzucchelli M.L.[1], Alvaro M.[2], Nestola F.[2], Pandolfo F., Domeneghetti M.C.[1]

[1]Dipartimento di Scienze della Terra e dell'Ambiente, Università degli Studi di Pavia, Italy

[2]Dipartimento di Geoscienze, Università degli Studi di Padova, Italy

In Mineralogical Magazine, vol. 79(1), pp. 71-87

[*Received 30 March 2014; Accepted 6 July 2014; Associate editor: W. Crichton*]

ABSTRACT

Two Pbca orthopyroxene samples, donpeacorite (DP N.1) and enstatite (B22 N.60) with chemical formulae $Mn_{0.54}Ca_{0.03}Mg_{1.43}Si_2O_6$ (X_{Mn} = 0.27) and $Fe_{0.54}Ca_{0.03}Mg_{1.43}Si_2O_6$ (X_{Fe} = 0.27), respectively, were investigated by single-crystal X-ray diffraction at high-temperature conditions. The nearly identical X_{Fe} and X_{Mn} make the two samples the perfect candidates to investigate the effect of the compositional change at the M2 site (i.e. Fe-Mn substitution) on the thermal expansion behaviour of orthopyroxenes.

Therefore, the unit-cell parameter thermal expansion behaviour of both samples has been investigated in the temperature range between room T and 1073 K. No evidence for phase transitions was found over that range. The two samples have been previously disordered with an ex situ annealing at ~1273 K.

The unit-cell parameters and volume thermal expansion data, collected on the disordered samples, have been fitted to a Fei Equation of State (EoS) and the following coefficients obtained: V_0 = 853.35(4) Å^3, $\alpha_{V,303K}$ = 2.31(24)10^{-5} K^{-1} and V_0 = 845.40(6) Å^3, $\alpha_{V,303K} = 2.51(25)\times10^{-5}$ K^{-1} for DP N.1 and B22 N.60, respectively.

While there is no difference in the volume thermal expansion coefficient as a function of composition and the expansion along the b direction is nearly identical for both samples, slight differences have been found along a and c lattice directions. The thermal expansion along the a direction is counterbalanced by that along c being responsible for the changes in lattice expansion scheme from $\alpha_b > \alpha_c > \alpha_a$ at room T, to $\alpha_c > \alpha_b > \alpha_a$ at high T. Therefore, as a result of the different behaviour along a and c, the unit-cell volume thermal expansion for both samples is identical within estimated standard deviations. The negligible effect of the Fe-Mn substitution on the bulk thermal expansion can be applied when dealing with geothermobarometry based on the elastic host-inclusion approach (e.g. Nestola et al., 2011; Howell et al., 2010; Angel et al., 2014a,b, 2015). In fact, though the compressibility effect is still not known, the nearly identical thermal expansion coefficients will not affect the entrapment pressure (P_e).

Keywords: orthopyroxene, thermal expansion, single crystal X-ray diffraction, order-disorder.

INTRODUCTION

Orthopyroxene (OPX) is a major component in the crust and in mineralogical models of the Earth's upper mantle to a depth of ~ 350 km (e.g., Ringwood, 1975; Bass and Anderson 1984), where it transforms to a high-pressure monoclinic polymorph (e.g., Pacalo and Gasparik 1990; Kanzaki 1991). Several mineralogical (e.g. Howell et al. 2010, Nestola et al. 2011, Angel et al., 2014a,b, 2015) and geophysical (e.g. e.g. Panning and Romanowicz, 2006; Kustowski et al., 2008) investigations have focused on the extremely complex geodynamic processes occurring at that depth. In recent decades, several studies have focused on the behaviour of orthopyroxenes with different compositions under extreme conditions of pressure and temperature and using a wide spread of experimental and computational techniques (e.g. Frisillo and Buljan, 1972; Frisillo and Barsch, 1972; Yang and Ghose, 1994; Hugh- Jones, 1997; Angel and Jackson, 2002; Miyake et al., 2004; Nestola et al., 2006; Perrillat et al., 2007; Gatta et al., 2007a,b). The large number of investigations on orthopyroxene is probably due to the very wide range of geological environments inwhich this mineral occurs, from magmatic to metamorphic rocks and meteorites, and to the wide range of composition found in nature. Investigation of the elastic properties of host minerals and their inclusions devoted to the determination of the entrapment pressures (Pe) has been demonstrated recently to be an extremely useful tool for understanding mantle-mineral stability fields (Howell et al., 2012; Nestola et al., 2011; Angel et al., 2014a,b, 2015; Nestola, 2015; Milani et al., 2015). However, the use of OPX elastic properties applied to the inclusionhost systems elastic methods requires very accurate and precise knowledge of their thermoelastic behaviour as a function of composition. With regard to the high-temperature behaviour of orthopyroxene, X-ray and neutron diffraction studies (single crystal and powder) on thermoelastic and structural behaviour have been performed on the $(Fe,Mg)SiO_3$ series to investigate the relationship between Fe-Mg substitution and thermal expansion behaviour (e.g. Frisillo and Barsch, 1972; Yang and Ghose, 1994; Gatta et al., 2007a,b). More recently, the thermal expansion behaviour as a function of more complex compositions (i.e. natural crystals) including Al, Ca, Mg and Fe has been studied at high-T and high-P conditions (e.g. Nestola et al., 2006; Gatta et al., 2007b and references therein). Among the OPX compositions found in nature, Mn/Mg-pyroxene, isostructural with ortho-enstatite (OEN), was described first by Petersen et al. (1984) and referred to historically as donpeacorite in siliceous marble units from Balmat, New York (Brown et al., 1980). Moreover, as shown by Stimpfl (2005), Mn-rich Fe-free orthopyroxenes undergo an exchange reaction with increasing temperature similar to that of Fe-Mg OPX already investigated by several authors in the past few decades (e.g. Saxena et al. 1989; Ganguly and Domeneghetti, 1996; Domeneghetti et al., 1995; Stimpfl et al., 1999). Stimpfl (2005) demonstrated clearly that preferential occupancy of the M2 site

as Mn >> Fe^{2+} > Mg implies that the assignment of Fe^{2+} + Mn = Fe* as one species, typically implemented to determine the quenched-site occupancies in Fe-rich/Mn-poor orthopyroxene, should be abandoned and that Mn should be considered to be completely ordered at M2. While it is then clear that Fe-rich and Mn-rich Mg-OPX have different partitioning behaviour, it is not known how the Fe-Mn substitution affects the thermoelastic properties of these mineral phases. Therefore, the aim of this present work was to investigate the high-temperature behaviour of two Mg-OPX with contrasting M2 site compositions (Mn-rich, DP N.1 and Fe-rich, B22 N.60) for a closer comparison of their thermal behaviour thus clarifying the effect of Fe-Mg-Mn substitution on the thermoelastic properties of OPX.

EXPERIMENTAL METHODS

Samples

Two *Pbca* orthopyroxene single crystals named DP N.1 and B22 N.60 were used for this study. Sample DP N.1 is a donpeacorite crystal [$Mn_{0.54}Ca_{0.03}Mg_{1.43}Si_2O_6$, X_{Mn}=0.27, size 150 x 100 x 80 μm] selected from a small sample from Balmat marbles, N.Y provided by E.U. Petersen. Sample B22 N.60 is a bronzite crystal [$Fe_{0.54}Ca_{0.03}Mg_{1.43}Si_2O_6$; X_{Fe}=0.27, size 200 x 190 x 90 μm] picked up from the granulite sample B22, Wilson Terrane, North Victoria Land, Antarctica, already studied by Tarantino et al. (2002). The two single crystals were selected for the high-*T* single crystal X-ray diffraction (SC-XRD) experiments on the basis of optical sharp extinction and diffraction peaks profiles (not more than 0.14° FWHM, Full Width at Half Maximum).

Room-temperature single-crystal X-ray diffraction

The X-ray intensity data of the two selected crystals DP N.1 and B22 N.60 were collected on a three-circle Bruker AXS SMART APEX diffractometer, equipped with a CCD detector (graphite-monochromatized MoKα radiation, λ= 0.71073 Å, 40 kV, 30 mA). A 0.3 mm MonoCap collimator was used to collect the data on the crystals. The Bruker SMART software (Bruker-AXS ©) package was used. A total of 9000 frames (frame resolution 5126512 pixels) were collected with ten different goniometer settings using the o-scan mode (scan width: 0.2° ω; exposure time: 10-20 s per frame depending on size of the crystals; detector–sample distance: 5.02 cm). About 13,900 reflections were collected for each crystal. A completeness of ~99% on the measured data was achieved up to y = 55°. The Bruker SAINT+ software v6.45A (Bruker-AXS ©) was used for data reduction, which included intensity integration, and background and Lorentz-polarization corrections. The semiempirical absorption correction of Blessing (1995), based on the determination of transmission factors for equivalent reflections, was applied using the program

SADABS (Sheldrick, 1996). The unit-cell parameters (see Table 1) were obtained by a least-squares procedure that refines the position of ~7000 reflections in the range 6-110°2θ, together with the sample– detector distance and aberration (i.e. X, Y, centre, pitch, roll and yaw). In the same table, the value of the discrepancy factor Rint calculated from the average of the $[Fo]^2$ values of equivalent pairs in *mmm* Laue symmetry is also reported. The observed Fo^2 values were then treated with a full-matrix least-squares refinement in the Pbca space group using SHELX-97 (Sheldrick, 2008) starting from the atomic coordinates reported by Stimpfl (2005) for donpeacorite sample DP1 and for sample B22 by Tarantino et al. (2002). Individual weights and the weighting scheme suggested by the program were used. The extinction correction was applied with the procedures of program SHELX-97.

The atomic scattering curves were taken from the *International Tables for X-ray Crystallography* (Ibers and Hamilton, 1970). Neutral vs. ionized scattering factors were refined in all sites that are not involved in chemical substitutions (Hawthorne et al., 1995) and complete ionization was assumed for Mg, Fe and Mn in M1 and M2 sites. Table 1 also reports the mean atomic numbers (m.a.n.) in electrons per formula unit (e.p.f.u.) at the M1 and M2 sites obtained when the structure refinement reached convergence, without introducing the chemical constraints. The relevant structural information (bond distances and angle, polyhedra volumes and distortions) are reported in Table 2.

Full-matrix least-squares with chemical constraints were then carried out to obtain the site partitioning for both crystals. For the donpeacorite sample, the microprobe analysis by Stimpfl (2005) was adopted while for the bronzite sample that provided by Tarantino et al. (2002) for sample B22 was used. The site distribution of M1 and M2 was obtained as in Domeneghetti et al. (2007) but accounting for the stronger preference for the M2 site of Mn compared to Fe^{2+} as observed by Stimpfl (2005). The Fe^{2+}/Mg and Mn/ Mg order degrees were estimated using the intracrystalline distribution coefficient k_D expressed as: $k_D = X_{Mn}^{M1}[1 - X_{Mn}^{M2}]/X_{Mn}^{M2}[1 - X_{Mn}^{M1}]$ for donpeacorite where $X_{Mn}^{M1} = (Mn)_{M1}/(Mn + Mg)_{M1}$ and $X_{Mn}^{M2} = (Mn)_{M2}/(Mn + Mg)_{M2}$ and $k_D = X_{Fe}^{M1}[1 - X_{Fe}^{M2}]/X_{Fe}^{M2}[1 - X_{Fe}^{M1}]$ for bronzite where $X_{Fe}^{M1} = (Fe)_{M1}/(Mn + Fe)_{M1}$ and $X_{Fe}^{M2} = (Fe)_{M2}/(Fe + Mg)_{M2}$. The k_D values are reported in Table 3 together with the site populations for both samples. The positional and atomic displacement parameters are reported in electronic Tables 4 and 5 and have been deposited with the Principal Editor of Mineralogical Magazine. They are available from www.minersoc.org/pages/e_journals/dep_mat_mm.html.

Room-temperature single-crystal X-ray diffraction

The X-ray intensity data of the two selected crystals DP N.1 and B22 N.60 were collected and the structure refinements performed in order to obtain the site populations and the Mn/Mg and Fe/Mg degree of order respectively. Intensity data were collected on a three-circle Bruker AXS SMART APEX diffractometer, equipped with a CCD detector (graphite-monochromatized Mo*K*α radiation, λ= 0.71073 Å, 40 kV, 30 mA). A 0.3 MonoCap collimator was used to collect the data on the crystals. The Bruker SMART software (Bruker-AXS ©) package was used. A total of 9000 frames (frame resolution 512 x 512 pixels) were collected with ten different goniometer settings using the w-scan mode (scan width: 0.2° w; exposure time: 10-20 s×frame^{-1} depending on size of the crystals; detector-sample distance: 5.02 cm). About 13900 reflections were collected for each crystal. A completeness of ~ 99% on the measured data was achieved up to θ = 55°. The Bruker SAINT+ software v6.45A (Bruker-AXS ©) was used for data reduction, including intensity integration and background and Lorentz-polarization corrections. The semi-empirical absorption correction of Blessing (1995), based on the determination of transmission factors for equivalent reflections, was applied using the program SADABS (Sheldrick 1996) and the orthorombic Laue group *mmm*. The unit-cell parameters were obtained by a least-squares procedure that refines the position of about 7000 reflections in the range 6 – 110° 2θ, and are reported in Table 1. This table also reports the mean atomic numbers (m.a.n.) in electrons per formula unit (e.p.f.u.) at the *M*1 and *M*2 sites obtained when the structure refinement reached convergence, without introducing the chemical constraints. In the same table the value of the discrepancy factor R_{int} calculated from the average of the $[F_o]^2$ values of equivalent pairs in *mmm* Laue symmetry is also reported. The observed F_o^2 values were then treated with a full-matrix least-squares refinement in the P_{bca} space group by SHELX-97 (Sheldrick 2008) starting from the atomic coordinates reported by Stimpfl (2005) for donpeacorite sample DP1 and for sample B22 by Tarantino et al. (2002). Individual weights and the weighting scheme suggested by the program were used. The extinction correction was applied with the procedures of program SHELX-97.

The atomic scattering curves were taken from the *International Tables for X-ray Crystallography* (Ibers and Hamilton (1970). Neutral vs. ionized scattering factors were refined in all sites that are not involved in chemical substitutions (Hawthorne et al. 1995) and complete ionization was assumed for Mg, Fe and Mn in *M*1 and *M*2 sites. The relevant structural information (bond distances and angle, polyhedra volumes and distortions) are reported in Table 2.

Full-matrix least-squares with chemical constraints were then carried out to obtain the site partitioning for both crystals. For donpeacorite sample the microprobe analysis by Stimpfl (2005)

was adopted while for bronzite sample that provided by Tarantino et al. (2002) for sample B22 was used. The site distribution of M1 and M2 was obtained as in Domeneghetti et al. (2007) by considering Mn fully ordered at M2 site according with the stronger preference for the M2 site of Mn compared to Fe^{2+} as observed by Stimpfl (2005). The Fe^{2+}/Mg and Mn/Mg order degrees were estimated using the intracrystalline distribution coefficient k_D expressed as: $k_D = X_{Mn}^{M1} [1- X_{Mn}^{M2}] / X_{Mn}^{M2} [1- X_{Mn}^{M1}]$ for donpeacorite where X_{Mn}^{M1} = $(Mn)_{M1/} (Mn+ Mg)_{M1}$ and X_{Mn}^{M2} = $(Mn)_{M2}/ (Mn+ Mg)_{M2}$, and $k_D = X_{Fe}^{M1} [1- X_{Fe}^{M2}] / X_{Fe}^{M2} [1- X_{Fe}^{M1}]$ for bronzite where X_{Fe}^{M1} = $(Fe)_{M1}/ (Fe + Mg)_{M1}$ and X_{Fe}^{M2} = $(Fe)_{M2}/ (Fe + Mg)_{M2}$. The k_D values are reported in Table 3 together with the site populations for both samples.

Table 4 and Table 5 report the positional and atomic displacement parameters and the lists of observed and calculated structure factors respectively, are available as deposited items.

E*x-situ annealing experiments*

As a consequence of the Mn-Mg and Fe-Mg exchange reactions occurring in orthopyroxenes, the extent of ordering decreases with increasing temperature. However, even though the effect of the disorder taking place during the heating experiment should be negligible (see Tarantino et al., 2002), the selected crystals of donpeacorite and bronzite have been annealed previously at high T 'ex situ' and then quenched following the protocol described by Alvaro et al. (2011), Pandolfo et al. (2015), Alvaro et al. (2015) and Domeneghetti et al. (2013) in order to prevent any unexpected contribution to the thermal expansion. Therefore, the thermal expansion was measured on the two samples with a disordered distribution of Mn-Mg and Fe-Mg, respectively. Following the geothermometer calibration given by Stimpfl (2005), the crystal in this study was annealed at 1273 K for 48 h to obtain a fully disordered distribution of Mn-Mg in donpeacorite. The same procedure (i.e. annealing temperature and time) was adopted for the B22 crystal. After each annealing experiment, intensity data collection and structural refinements were performed on the heat-treated crystals (see Tables 2 and 3 and deposited Tables 4 and 5) following the same procedure as reported in the section ''Room temperature X-ray diffraction'' (see also Fioretti et al. 2007; Alvaro et al., 2011; Domeneghetti et al., 2013; and Alvaro et al. 2015 for further details). It is clear that both crystals show a more disordered distribution of Mn-Mg and Fe-Mg, respectively compared to the untreated ones. It is also evident that, at the same T and in the same annealing time, bronzite disordered more than donpeacorite as expected by the different partitioning behaviour of Fe compared to Mn (Stimpfl, 2005).

Table 1.a Unit-cell parameters and information on data collection and structure refinement for donpeacorite crystal (DP N1): untreated, annealed ex-situ at 1273K and after the high temperature *in situ* experiment.

	Untreated	Annealed for 48h, 1273 K	After HT in situ experiment
a (Å)	18.3550 (8)	18.3561 (9)	18.3790(2)
b (Å)	8.8789 (7)	8.8803 (6)	8.8817 (10)
c (Å)	5.2359 (5)	5.2357 (4)	5.2383 (6)
V (Å^3)	853.31 (11)	853.46 (10)	855.06 (17)
I_{ind}	2240	2252	2242
R_I	3.87	3.85	4.01
wR^2	8.26	7.72	8.14
S	1.145	1.127	1.135
m.a.n. M1	12.08(6)	13.20(6)	12.77(6)
m.a.n. M2	19.73(8)	18.78(6)	19.21(8)
m.a.n. M1+M2	31.81(10)	31.98(8)	31.98(10)

Note: $R1 = \sum||F_{obs}| - |F_{calc}||/\sum|F_{obs}|$; $wR_2 = \{S[w(F^2_{obs} - F^2_{calc})^2]/\sum[w(F^2_{obs})^2]\}^{0.5}$, $w = 1/[\sigma^2(F^2_{obs}) + (0.01\cdot P)^2]$, $P = [Max(F^2_{obs},0) + 2\cdot F^2_{calc}]/3$.
m.a.n. = mean atomic number.

Table 1.b Unit-cell parameters and information on data collection and structure refinement for bronzite crystal (B22 N60): untreated, annealed ex situ at 1273K and after the high temperature in situ experiment.

	Untreated	Annealed for 48h, 1273 K	After HT in situ experiment
a (Å)	18.2864 (6)	18.2877 (6)	18.2843 (5)
b (Å)	8.8782(4)	8.8778 (4)	8.8763 (4)
c (Å)	5.2057 (3)	5.2069 (3)	5.2070 (3)
V (Å^3)	845.15 (7)	845.36(7)	845.08 (7)
I_{ind}	2245	2238	2246
R_I	2.40	3.28	3.20
wR^2	5.48	7.19	6.90
S	1.084	1.120	1.111
m.a.n. M1	12.39(5)	14.18(7)	13.61(6)
m.a.n. M2	20.01(5)	18.23(7)	18.85(6)
m.a.n. M1+M2	32.40(7)	32.41(10)	32.46(9)

Note: Note: $R1 = \sum||F_{obs}| - |F_{calc}||/\sum|F_{obs}|$; $wR_2 = \{S[w(F^2_{obs} - F^2_{calc})^2]/\sum[w(F^2_{obs})^2]\}^{0.5}$, $w = 1/[\sigma^2(F^2_{obs}) + (0.01\cdot P)^2]$, $P = [Max(F^2_{obs},0) + 2\cdot F^2_{calc}]/3$.
m.a.n. = mean atomic number.

High-temperature single-crystal X-ray diffraction

The high-temperature SC-XRD experiment has been performed on the previously heat-treated crystals DP N.1 and BR N.60 with a Philips PW1100 operated with FEBO software (control software developed locally) equipped with a micro-furnace controlled by a Eurotherm control unit at the Department of Earth and Environmentm Sciences, University of Pavia, Italy.

Each crystal was mounted inside quartz vials (0.3 mm inner diameter and 26 mm long) together with a small iron wire to prevent Fe^{2+} oxidation using the same procedure as described by Pandolfo et al. (2015) and was held in place by means of quartz wool.

The vial was mounted on a metal goniometer head on the diffractometer operating with MoKa radiation at 30 mA/55 kV and using a 0.5 mm short collimator. The microfurnace with a H-shaped Pt-Rh resistance heater and a Pt:Pt-Rh thermocouple inside a steel cylindrical cage 2.5 cm wide, closed with a Kapton film, was placed on top of the goniometer head. The device, calibrated before the experiment following the procedure described by Pandolfo et al. (2015), allows the collection of diffraction data up to θ max = 34º and T_{max} = 1473 K.

Accurate and precise unit-cell parameters were collected for the sample upon heating from 298 K to 1073 K with steps of 50 K. At each temperature step the unit-cell parameters were calculated by least-squares fitting on a group of 60 selected reflections following the LAT procedure described by Pandolfo et al. (2015). The results of the aforementioned procedure for the unit-cell parameter measurements are reported in Table 6 and Fig. 1. Diffraction-peak profiles were collected for each temperature step on the same 60 reflections used for the LAT procedure to constantly evaluate the quality of the crystal (i.e. FWHM, position, background and the crystal offsets).

To check whether any ordering in Mn/Mg and Fe^{2+}/Mg may have taken place during the high-T experiment, further intensity data collections were performed on each of the two recovered crystals DP N.1 and B22 N.60 (following the same procedure as in the ‘‘Room-temperature single crystal X-ray diffraction’’ section). The results are reported in Tables 1, 2 and 3 for easier comparison with those obtained after the first ex situ annealing. On the basis of the results of the structure refinements with chemical constraints and the k_D values, it appears that some ordering occurred for both samples.

Table 2. Structure refinement results: bond distances (Å) and angles (°), polyhedra volumes (Å^3) and distortions.

	DP N.1[1]	DP N.1[2]	DP N.1[3]	B22 N.60[1]	B22 N.60[2]	B22 N.60[3]
M1-						
O2A	2.0267	2.0286	2.0294	2.0274	2.0282	2.0283
O1A	2.0424	2.0461	2.0457	2.0279	2.0353	2.0332
O2B	2.0473	2.0504	2.0505	2.0592	2.0609	2.0596
O1B	2.0672	2.0701	2.0697	2.0607	2.069	2.0651
O1A	2.1477	2.1566	2.1542	2.1484	2.1552	2.1526
O1B	2.1796	2.1835	2.1834	2.1684	2.1713	2.1705
VM1	11.966(10)	12.032(10)	12.028(13)	11.901(15)	11.977(30)	11.948(41)
Distortion*	0.008	0.0085	0.0081	0.0094	0.0098	0.0096
<M1-O>	2.085	2.089	2.089	2.082	2.087	2.085
M2-						
O2B	2.0418	2.0303	2.0374	1.995	1.9929	1.994
O2A	2.1068	2.0956	2.1014	2.0512	2.049	2.0494
01B	2.1338	2.1224	2.1278	2.1062	2.0954	2.0991
O1A	2.16	2.1509	2.1563	2.1482	2.1371	2.1409
O3A	2.3275	2.3289	2.3302	2.341	2.3347	2.3359
O3B	2.536	2.5525	2.5489	2.4878	2.486	2.4871
VM2	13.374(10)	13.319(10)	13.376(13)	12.939(31)	12.870(46)	12.891(36)
Distortion*	0.0852	0.084	0.0846	0.0778	0.0756	0.0765
<M2-O>	2.218	2.213	2.217	2.187	2.182	2.184
O3A – O3A – O3A	164.01 (0.07)	163.74 (0.07)	163.88 (0.07)	163.38 (0.06)	162.59 (0.07)	162.81 (0.07)
O3B – O3B – O3B	145.55 (0.07)	145.40 (0.07)	145.51 (0.07)	142.09 (0.05)	141.56 (0.07)	141.71 (0.06)
SiA-						
O2A	1.5920(9)	1.5917(8)	1.5921(8)	1.5966(6)	1.5959(8)	1.5955(8)
O1A	1.6115(9)	1.6109(8)	1.6135(9)	1.6108(6)	1.6106(8)	1.6100(8)
O3A	1.6460(9)	1.6438(8)	1.6449(9)	1.6409(6)	1.6403(8)	1.6410(8)
O3A	1.6685(9)	1.6672(8)	1.6689(9)	1.6599(6)	1.6611(8)	1.6605(8)
SiB-						
O2B	1.5943(9)	1.5928(8)	1.5935(9)	1.5982(6)	1.5962(8)	1.5964(8)
O1B	1.6156(9)	1.6166(8)	1.6183(9)	1.6204(6)	1.6201(8)	1.6197(8)
O3B	1.6710(9)	1.6687(8)	1.6697(9)	1.6686(7)	1.6705(8)	1.6696(8)
O3B	1.6752(9)	1.6726(8)	1.6745(9)	1.6738(6)	1.6746(8)	1.6751(8)

Data collected on: [1]Natural sample; [2]Sample annealed at 1273 K for 48 h; [3]Sample after the high-temperature in situ experiments.

* Distortion parameters calculated using the IVTON program (Balic´ Žunic´ and Vickovic´, 1996).

Table 3.a Site populations for donpeacorite crystal (DP N.1) untreated, annealed *ex situ* at1000°C and after the high temperature in situ experiment.

Site	Cations	Untreated	Annealed for 48h, 1273 K	After HT *in situ* experiment
T	Si	1.9973	1.9971	1.9972
	Al	0.0027	0.0029	0.0028
M1	Mg	0.9948(18)	0.9169(18)	0.9479(18)
	Fe^{3+}	0.0000	0.0000	0.0000
	Mn	0.0039(18)	0.0817(18)	0.0507(18)
	Cr	0.0000	0.0000	0.0000
	Ti	0.0014	0.0015	0.0014
M2	Mg	0.4361(21)	0.5078(20)	0.4764(21)
	Ca	0.0248	0.0249	0.0252
	Mn	0.5391(22)	0.4673(22)	0.4984(22)
	Na	0.0000	0.0000	0.0000
	X^{Mn}M1	0.0039	0.0818	0.0508
	X^{Mn}M2	0.5528	0.4792	0.5113
	k_D	0.0031	0.0968	0.0511
	m.a.n. M1+M2	31.27	31.35	31.35

$k_D = X_{Fe}^{M1}\,[1-X_{Fe}^{M2}] / X_{Fe}^{M2}\,[1-X_{Fe}^{M1}]$ m.a.n. = mean atomic number.

Table 3.b Site population for bronzite crystal (B22 N.60) untreated, annealed exsitu at1000°C and after the high temperature in situ experiment.

Site	Cations	Untreated	Annealed for 48h, 1273 K	After HT in situexperiment
T	Si	1.9860	1.9855	1.9856
	Al	0.0140	0.0145	0.0145
M1	Mg	0.9719(15)	0.8440(18)	0.8850(18)
	Fe^{3+}	0.0000	0.0000	0.0000
	Fe	0.0179(16)	0.1456(20)	0.1045(19)
	Cr	0.0064	0.0065	0.0065
	Ti	0.0038	0.0040	0.0039
M2	Mg	0.4148 (18)	0.5428(22)	0.4988(20)
	Ca	0.0239	0.0239	0.0241
	Mn	0.0123	0.0123	0.0127
	Fe	0.5490(24)	0.4210(26)	0.4644(25)
	X^{Fe}M1	0.0181	0.1471	0.1056
	X^{Fe}M2	0.5696	0.4368	0.4821
	kD	0.0139	0.2224	0.126
	M1+M2	32.40282	32.40188	32.44074

$k_D = X_{Fe}^{M1}\,[1-X_{Fe}^{M2}] / X_{Fe}^{M2}\,[1-X_{Fe}^{M1}]$ m.a.n. = mean atomic number.

Table 6.a Unit-cell parameters measured by single X-ray diffraction with increasing temperature for sample DP N.1.

T (K)	*a* (Å)	b (Å)	c (Å)	V (Å^3)
Before HT	18.3550(7)	8.8789(5)	5.2359(4)	853.31(9)
303	18.3561(6)	8.8803(4)	5.2357(3)	853.46(7)
323	18.3587(8)	8.8814(6)	5.2367(4)	853.85(10)
373	18.3647(8)	8.8868(6)	5.2394(4)	855.09(10)
423	18.3726(8)	8.8916(6)	5.2416(3)	856.28(8)
473	18.3788(6)	8.8979(5)	5.2449(3)	857.71(7)
523	18.3868(6)	8.9030(5)	5.2475(3)	859.00(7)
573	18.3938(9)	8.9081(7)	5.2512(4)	860.43(10)
623	18.4015(6)	8.9139(5)	5.2543(3)	861.86(7)
673	18.4118(6)	8.9199(4)	5.2577(3)	863.48(7)
723	18.4202(8)	8.9242(7)	5.2619(3)	864.98(9)
773	18.4312(8)	8.9293(6)	5.2645(4)	866.42(10)
823	18.4373(7)	8.9359(4)	5.2693(3)	868.14(7)
873	18.4495(8)	8.9401(7)	5.2720(4)	869.57(10)
923	18.4576(9)	8.9450(7)	5.2773(5)	871.30(12)
973	18.4672(8)	8.9473(6)	5.2820(4)	872.75(10)
1023	18.4771(8)	8.9507(5)	5.2873(4)	874.43(9)
1073	18.4871(8)	8.9560(6)	5.2901(4)	875.88(10)

Standard deviations are given in parenthesis.

Table 6.b Unit-cell parameters measured by single X-ray diffraction with increasing temperature for sample bronzite B22 N.60.

T (K)	*a* (Å)	b (Å)	c (Å)	V (Å^3)
Before HT	18.2864(6)	8.8782(4)	5.2057(3)	845.15(7)
303	18.2877(6)	8.8778(4)	5.2069(3)	845.36(7)
323	18.2907(8)	8.8804(6)	5.2078(3)	845.90(8)
373	18.2969(6)	8.8855(4)	5.2097(3)	846.98(7)
423	18.3012(8)	8.8916(5)	5.2133(3)	848.34(8)
473	18.3108(6)	8.8951(4)	5.2152(3)	849.43(7)
523	18.3183(7)	8.9024(5)	5.2183(3)	850.98(8)
573	18.3270(7)	8.9069(5)	5.2215(3)	852.34(8)
623	18.3340(7)	8.9127(6)	5.2246(3)	853.73(8)
673	18.3426(7)	8.9174(5)	5.2284(3)	855.2(8)
723	18.3519(6)	8.9234(4)	5.2308(3)	856.60(7)
773	18.3606(6)	8.9298(4)	5.2344(3)	858.21(7)
823	18.3692(6)	8.9356(5)	5.2381(3)	859.78(7)
873	18.3786(6)	8.9407(5)	5.2419(3)	861.34(7)
923	18.3881(7)	8.9465(5)	5.2457(3)	862.97(8)
973	18.3941(7)	8.9520(4)	5.2501(3)	864.50(7)
1023	18.4040(6)	8.9569(5)	5.2536(3)	866.02(7)
1073	18.4129(7)	8.9624(5)	5.2587(3)	867.81(8)

Standard deviations are given in parenthesis.

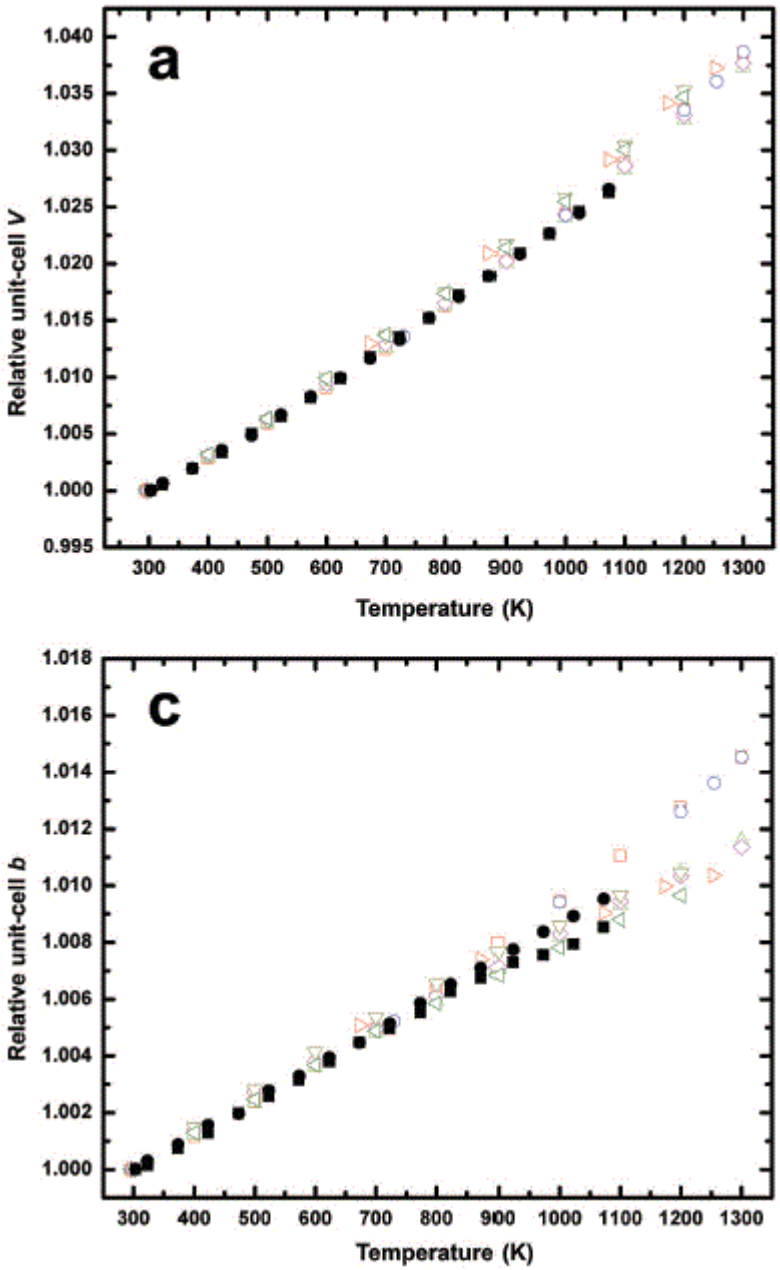

Fig. 1 (*this and facing page*). Relative unit-cell volume (a) and lattice parameters (b, c, d) as a function of temperature for all the samples analysed. Filled squares and circles, both fitted with a Fei-EoS (a2 were constrained and fixed to zero), represent DP N.1 and B22 N.60 samples, respectively. Open symbols represent data from Yang and Ghose (1994): blue circles for Fs0; red squares for Fs_{20}; green upwards-pointing triangles for Fs_{40}; magenta diamond for Fs_{50}; dark-yellow downwards-pointing triangles for Fs_{75}; olive-green left-pointing triangles for Fs_{83} and orange right-pointing triangles for Fs_{100}.

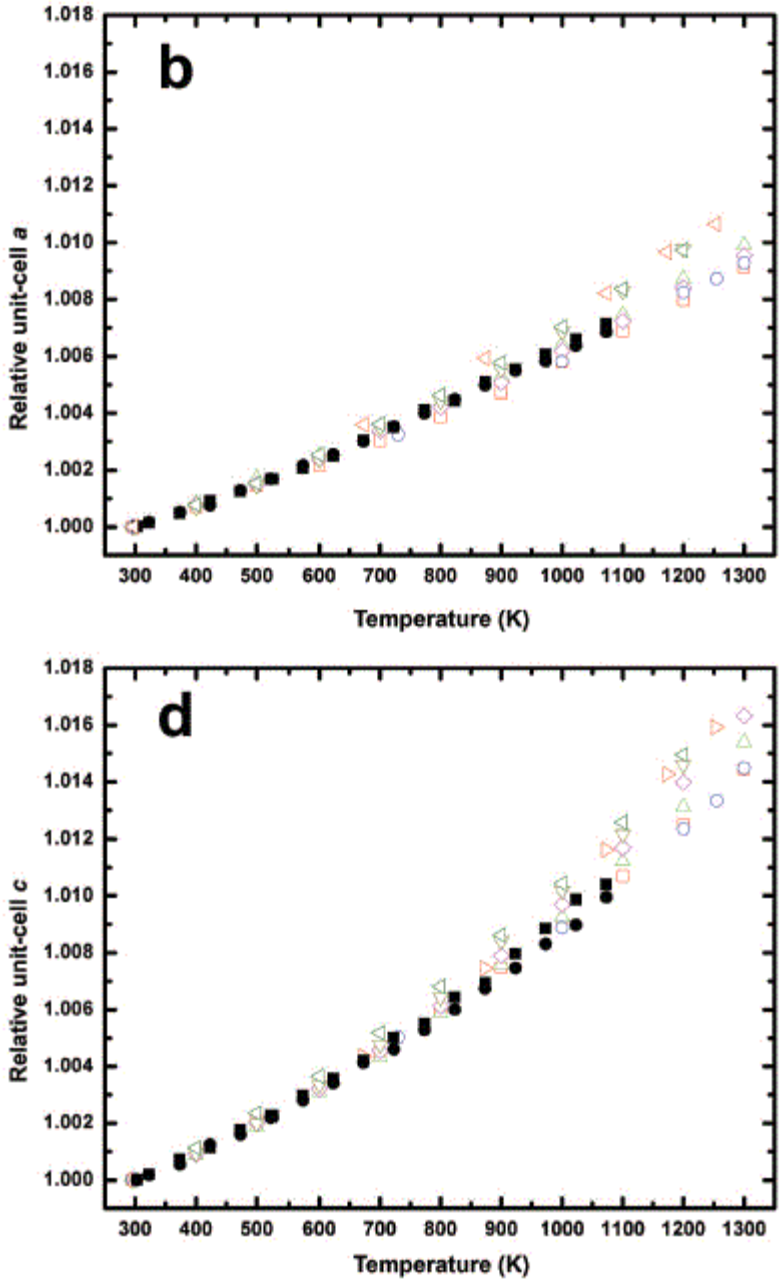
b
Relative unit-cell a
Temperature (K)
d
Relative unit-cell c
Temperature (K)

RESULTS AND DISCUSSION

Room-T structure and lattice parameters

In the orthopyroxene structure, the two crystallographically non-equivalent octahedral M1 and M2 sites (Smyth, 1973; Sueno et al., 1976) are mainly occupied by Mg and Fe for bronzite and Mg and Mn for donpeacorite. Both Fe and Mn have a stronger preference for the larger and more distorted M2 site (Hugh-Jones, 1997; Domeneghetti and Steffen, 1992; Tarantino et al., 2002; Stimpfl, 2005; and references therein). In the natural donpeacorite and bronzite crystals of this study, Mn and Fe are almost totally ordered at site M2 (see Table 3) due to the larger Mn (ionic radius = 0.83 Å) compared to Fe (ionic radius = 0.78 Å), the M2 site of donpeacorite is significantly larger and more distorted with respect to that of bronzite (see Table 3).

As shown in Table 2, the deformation of the M2 polyhedra decreases with decreasing Mn and Fe contents due to disordering (i.e. from 0.0852 to 0.084 and from 0.0778 to 0.0756 for DP N.1 and B22 N.60, respectively).

The structural changes occurring during the disordering process for the bronzite B22 N.60 sample are in perfect agreement with the observation reported by Domeneghetti et al. (1985) for Fe-Mg orthopyroxenes. In particular, the Fe exchange (0.128 atoms per formula unit (a.p.f.u.)) between the M2 and M1 site causes (1) an increase in the M1 polyhedra volume (by 0.076 $Å^3$) and the relevant bond lengths; (2) a decrease in the M2 polyhedra volume (by 0.069 $Å^3$) and bond lengths which in turns leads to a decrease of the O3–O3–O3 kinking angles (by 0.79º and 0.53º for the A-chain and the B-chain, respectively). Whereas the structural changes occurring during the disordering process at 1273 K for the donpeacorite sample are in perfect agreement with those reported by Stimpfl (2005) on a donpeacorite sample heated at 1253 K. In this present study of the DP N.1 sample the exchange of 0.0718 a.p.f.u. of Mn between the M2 and M1 site produces an increase in the polyhedral volume of 0.066 $Å^3$ for the M1 site, greater than the decrease (by 0.055 $Å^3$) for the M2 site. While for the M1 site the increase in the polyhedral volume occurs with the lengthening of all the M1-O bond distances, the smaller decrease in M2 volume occurs mainly because of the pronounced shortening of the M2-O1 and M2-O2 bond distances hampered by the lengthening of the M2-O3 bond distances (mostly the M2-O3B, see Table 2). Such differential shortening is the main cause of the greater distortion of the M2 polyhedron for DP with respect to B22 N.60 that contributes to a smaller decrease of both the A and B tetrahedral chain kinking angles during the disordering process.

Such deformation occurs mainly along [1 0 0] and [0 0 1] directions (i.e. a and c lattices, respectively). The deformation along [0 0 1] occurs mostly because of the polyhedral volume change that affects the kinking angle by straightening both the TB and TA chains of tetrahedral (see

above). Such a change is confirmed by the greater expansion of the c lattice parameter for the DP sample (0.6%, ~0.035 Å) which, at room T, is longer than that of bronzite B22 orthopyroxene (see Table 2). The deformation of the M2 polyhedron along [1 0 0] clearly affects the length of the a unit-cell parameter at room T, which is much longer when compared with that of bronzite (0.4%, ~0.07 Å).

On the other hand, the deformation occurring as a function of Mn content along [0 1 0] is nearly negligible as the structural changes (M1-O and M2-O bond lengths) are balanced by the change in the kinking angle of the TA and TB chain of tetrahedra. Therefore, the b lattice parameter is smaller for DP N.1 (Mn opx) than that of the equivalent orthopyroxene on the Fe_Mg series. The structural and the lattice parameters (mostly a and c) changes at room T are probably responsible for the differences in the room-T unit-cell volume as a function of composition (see Fig. 2 and Table 2). In Fig. 2, the unit-cell volume obtained on the samples in this present study are plotted together with all the available literature data for pure Fe-Mg synthetic orthopyroxenes by Yang and Ghose (1994) against the Fe/(Fe+Mg) and Mn/(Mn+Mg) ratio for Fe-Mg orthopyroxene and donpeacorite, respectively. The relationship between Fe-Mg substitution (i.e. Fe/Fe+Mg) and unit-cell volume at room P,T is not valid for Fe-poor orthopyroxenes (see Fig. 2). In fact, the 8.1 $Å^3$ (~1%) larger room-T unit-cell volume of DP N.1 [853.46(7) $Å^3$] compared to that of B22 N.60 [845.36(7) $Å^3$] reflects the larger ionic radius of Mn compared to Fe^{2+}. No further clear trend was found for any of the other room-T lattice parameters as a function of composition (see Table 6 and Fig. 2).

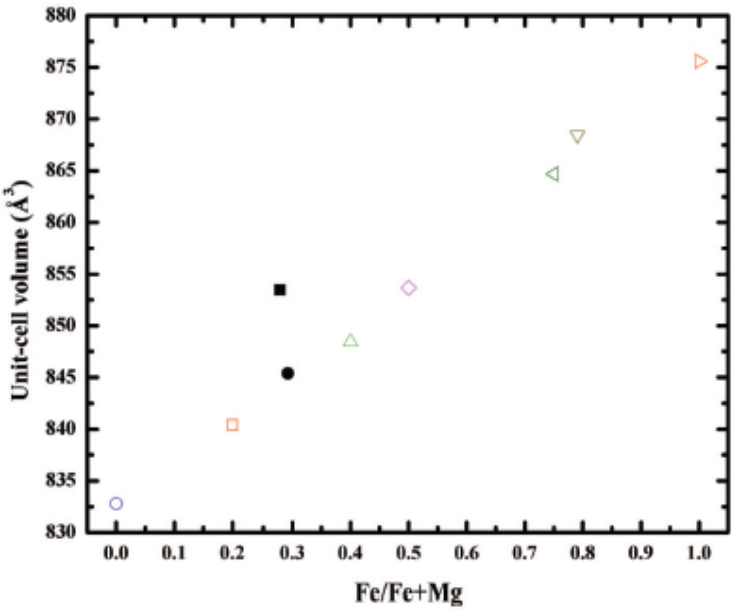

Fig. 2 Unit-cell volume as a function of Fe/(Fe+Mg) values for bronzite samples while Mn/(Mn+Mg) values were considered for the donpeacorite sample. Open symbols represent data for a synthetic sample from Yang and Ghose (1994); filled circles and filled squares are B22 N.60 and DP N.1, respectively.

Unit-cell parameters evolution with T

As shown in Fig. 1, the normalized unit-cell volume and lattice parameters increase almost linearly with temperature (T) for both the completely disordered donpeacorite (DP N.1) and bronzite (B22 N.60) samples. Between the two samples there is no difference in the unit-cell volume expansion as a function of temperature. However, such a volume behaviour is the result of different unit-cell parameter expansion schemes (i.e. the effect of differential thermal expansion behaviour along unit-cell directions). Over the entire T range investigated, the b lattice for DP N.1 shows a much smaller expansion (0.84%) than that of B22 N.60 (0.94%). Such a difference occurs mostly at a T >800 K. On the other hand, in the investigated T range, a and c lattice parameters for DP N.1 show larger expansion (0.71% and 1.03% for a and c, respectively) than that of B22 N.60 (0.68% and 0.98% for a and c, respectively).

In Fig. 3, the lattice parameters for the samples studied in this work are plotted together with those obtained by SC-XRD on the pure synthetic Fe-Mg orthopyroxenes by Yang and Ghose (1994). B22 N.60 lattice parameters behave as a function of temperature as expected for an intermediate composition (i.e. Fs_{20} and Fs_{40}), whereas the behaviour of DP N.1 is much closer to that of the Fs_{50} because of the Mn presence. Therefore, it seems that the Fe-Mn substitution controls the unit-cell volume expansion with T only by affecting the V_0 unit-cell volume at room T (see Fig. 3).

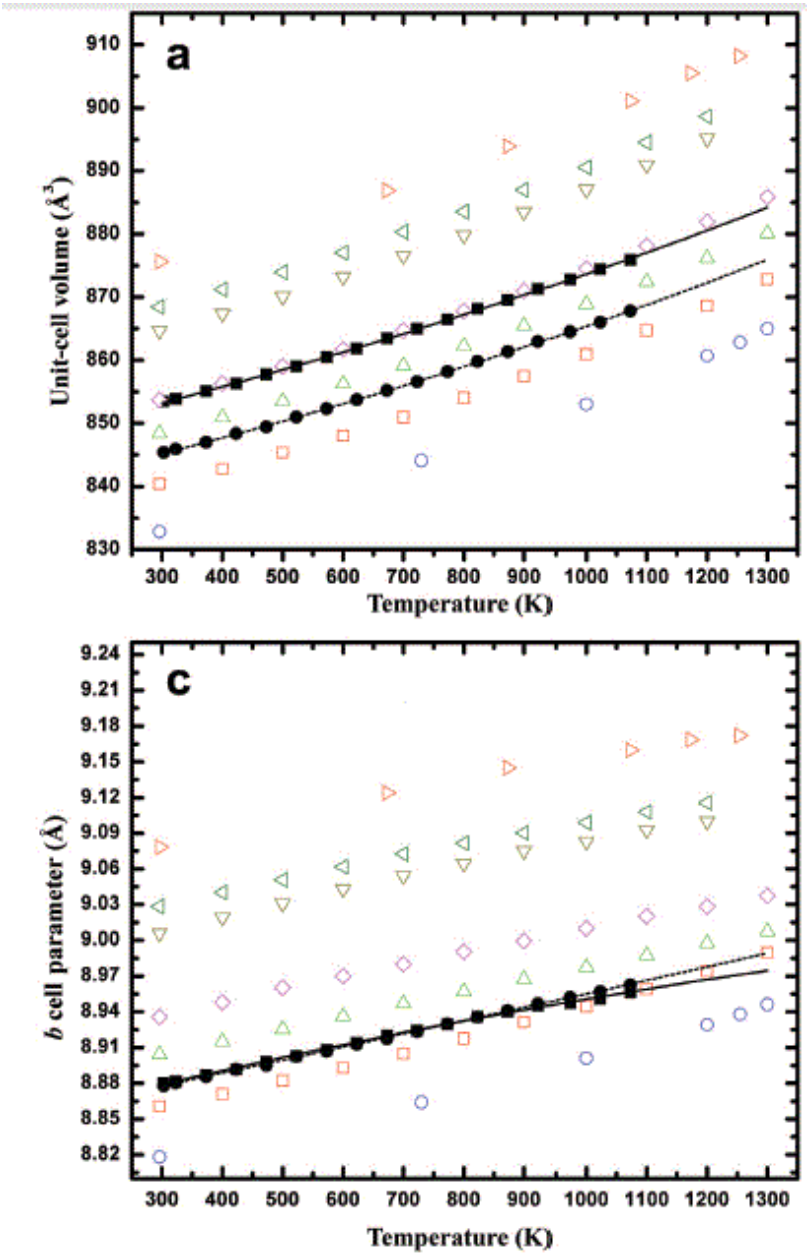

Fig. 3 (this and facing page). Unit-cell (b,c,d) and volume (a) parameters as a function of temperature for all the samples analyzed. Filled squares and circles both fitted with a Fei-EoS (α_2 were constrained and fixed to zero), represent DP N.1 and B22 N.60 samples, respectively. Open symbols represent data from Yang and Ghose (1994):
blue circles for Fs_0; red squares for Fs_{20}; green upwards-pointing triangles for Fs_{40}; magenta diamonds for Fs_{50}; dark-yellow downwards-pointing triangles for Fs_{75}; olive-green left-pointing triangles for Fs_{83} and orange right pointing triangles for Fs_{100}.

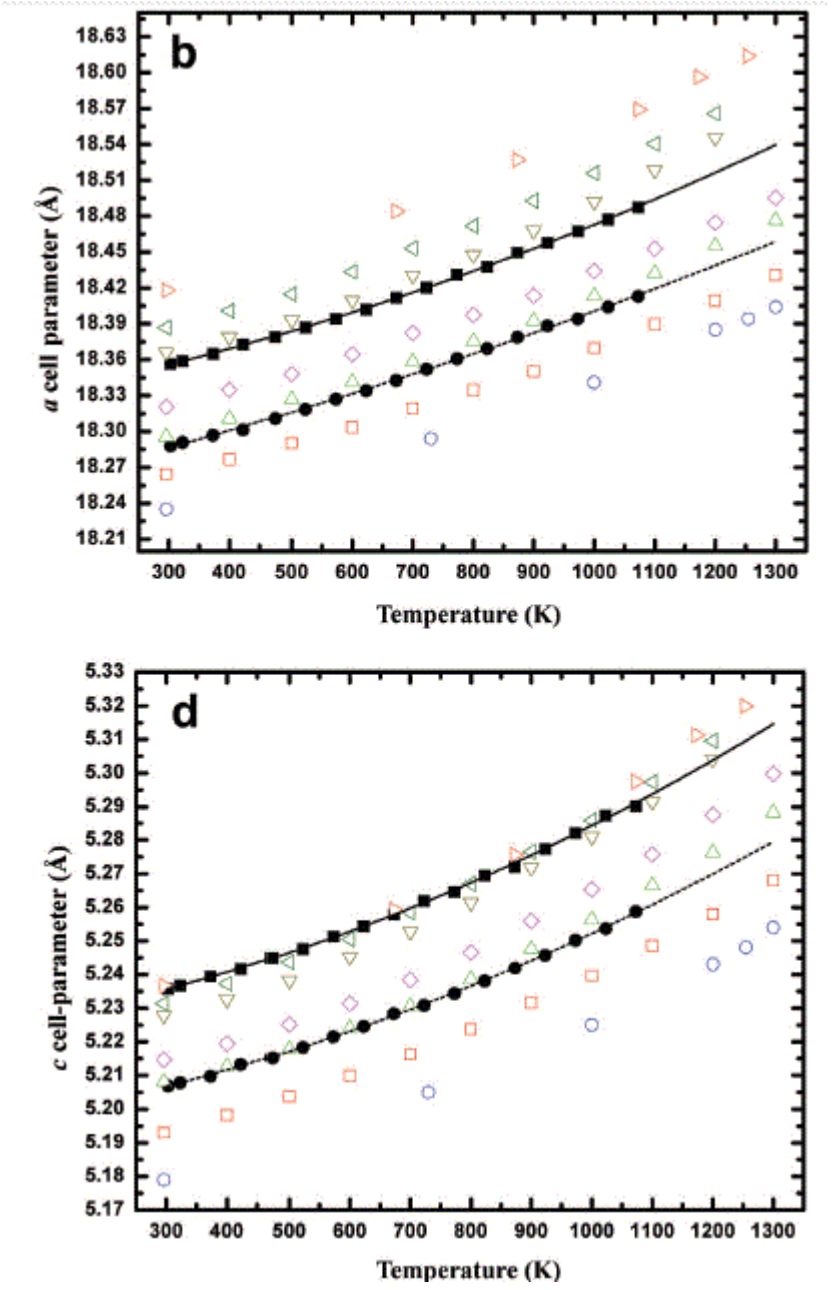

Unit-cell parameters thermal expansion

For the purpose of comparison all the unit-cell and volume thermal expansion values of both samples were fitted to a Berman-type (Berman, 1988) and Fei-type (Fei, 1995) Equation of State (EoS) using the Eosfit7c program (Angel et al., 2014a). In Table 7, all the fitting results obtained on the samples studied in this present work are shown together with those published and recalculated for available datasets in the literature (Yang and Ghose, 1994). In order to compare the results from this present study with those recalculated from the literature, the most reasonable fitting model was that obtained with the Fei-type EoS constraining the α_2 to 0 as those obtained refining the α_2 coefficient led to 'nonphysical' results for the lattice parameter thermal expansion coefficients (see Angel et al., 2014a for further details). Moreover, the results obtained with the Berman-type EoS

produced no improvement in the statistical parameters, such as, for instance, the $\omega\chi^2$ values (see Pandolfo et al., 2015 for further details). A higher order of the polynomial is not recommended, mainly because of the restricted range of T investigated and/or the small number of data points in the T interval.

At room temperature the relative magnitudes of unit-cell thermal expansion coefficients for both samples in this present study are in the order $\alpha_b > \alpha_c > \alpha_a$, in good agreement with the available literature data for Fe-Mg opx. However, subtle differences in the axial thermal expansion between the two samples are evident. The c lattice thermal expansion for both samples are nearly identical. On the other hand, the a lattice thermal expansion for DP N.1 is smaller than that of B22 N.60 ($\Delta\alpha a = 0.07610^{-5}K^{-1}$, see Table 7). Such a difference is compensated by a greater expansion of the b lattice for DP N.1 compared to B22 N.60, producing, therefore, a volume thermal expansion difference of only $0.0561010^{-5}K^{-1}$ (with DP N.1 being greater than B22 N.60, although such a difference is smaller than 1 e.s.d. (estimated standard deviation, see Table 7). It is clear therefore that, within the e.s.d., the room-T thermal expansion coefficient is not affected by Fe-Mn substitution. At high T, changes in the thermal expansion scheme were observed for all the lattice parameters in both samples ($\alpha_c > \alpha_b > \alpha_a$ for B22 N.60 and $\alpha_c > \alpha_b \geq \alpha_a$ for donpeacorite) demonstrating that at high T the two samples show different behaviour mainly because of the changes in the expansion mechanism.

At 1000 K the relationship between the lattice expansion of DP N.1 and B22 N.60 are completely changed with respect to that at 303 K, being $\alpha_{V(DP)} < \alpha_{V(B22)}$, $\alpha_{a(DP)} > \alpha_{a(B22)}$, $\alpha_{b(DP)} < \alpha_{b(B2)}$, $\alpha_{c(DP)} > \alpha_{c(B22)}$.

The negligible effect of the Fe-Mn substitution on the bulk thermal expansion finds its application when dealing with geothermobarometry based on the elastic host-inclusion approach (e.g. Nestola et al., 2011; Howell et al., 2010; Angel et al., 2014a,b, 2015). In fact, though the compressibility effect is still not known, the nearly identical thermal expansion coefficients will not affect the entrapment pressure (P_e). However, in future work, the different axial expansion scheme, due to Fe-Mn substitution, may suggest the possibility that the elastic anisotropy should be accounted for.

Table 7a. Volume thermal expansion fitting results for the samples in the present study together with those recalculated from the available literature data.

	Fei-type EoS			Fei-type EoS (with α_2=0)			Berman-type EoS		
	$\alpha_{V,303}$ ($\times 10^{-5}$ K^{-1})	V (Å^3)	χ^2	$\alpha_{V,303}$ ($\times 10^{-5}$ K^{-1})	V (Å^3)	χ^2	$\alpha_{V,303}$ ($\times 10^{-5}$ K^{-1})	V (Å^3)	χ^2
DP N.1	2.31(24)	853.35(4)	0.77	2.94(8)	853.34(6)	2.74	2.93(5)	853.34(6)	2.66
B22 N.60	2.51(25)	845.40(6)	0.93	2.89(7)	845.29(5)	1.52	2.88(4)	845.30(5)	1.47
Fs_0	2.77(24.36)	832.96(4.28)	0.00	2.62(3.11)	832.96(3.79)	0.00	2.60(2.04)	832.96(3.83)	0.00
Fs_{20}	2.64(36)	840.58(14)	0.04	2.64(10)	840.58(10)	0.03	2.62(6)	840.59(10)	0.04
Fs_{40}	2.71(30)	848.61(10)	0.04	2.75(8)	848.60(7)	0.04	2.74(5)	848.61(7)	0.04
Fs_{50}	-	-	0.10	2.83(8)	853.89(7)	0.20	2.82(5)	853.89(7)	0.24
Fs_{75}	2.76(42)	864.86(11)	0.30	2.97(11)	864.82(8)	0.41	2.95(7)	864.83(8)	0.38
Fs_{83}	3.04(40)	868.60(15)	0.35	2.98(10)	868.61(11)	0.31	2.96(7)	868.62(11)	0.33
Fs_{100}	2.67(178)	875.74(47)	9.10	3.18(27)	875.72(37)	6.74	3.17(18)	875.73(37)	6.61

Data for samples Fs_0, Fs_{20}, Fs_{40}, Fs_{50}, Fs_{75}, Fs_{83} and Fs_{100} are taken from Yang and Ghose (1994).
- Indicates that the results obtained from the fitting lead to non-physical a values (see Angel et al., 2014b for further details).

Table 7b. Lattice parameter, a, thermal expansion fitting results for the samples in the present study together withthose recalculated from the available literature data.

	Fei-type EoS			Fei-type EoS (with α_2=0)			Berman-type EoS		
	$\alpha_{a,303}$ ($\times 10^{-5}$ K^{-1})	a_0 (Å)	χ^2	$\alpha_{a,303}$ ($\times 10^{-5}$ K^{-1})	a_0 (Å)	χ^2	$\alpha_{a,303}$ ($\times 10^{-5}$ K^{-1})	a_0 (Å)	χ^2
DP N.1	0.59(13)	18.3562(5)	1.54	0.71(3)	18.3551(5)	1.85	0.70(2)	18.3552(5)	1.81
B22 N.60	0.49(13)	18.2877(6)	1.51	0.77(4)	18.2866(7)	3.23	0.77(2)	18.2859(7)	3.20
Fs_0	0.6(12.4)	18.24(3)	0.00	0.6(9)	18.24(3)	0.00	0.6(6)	18.24(3)	0.00
Fs_{20}	0.67(24)	18.2649(22)	0.10	0.62(7)	18.2652(16)	0.10	0.61(4)	18.2647(17)	0.10
Fs_{40}	-	-	-	-	18.2971(11)	0.18	-	18.2971(11)	0.19
Fs_{50}	0.70(23)	18.3213(20)	0.29	0.71(7)	18.3213(14)	0.26	0.71(4)	18.3206(14)	0.26
Fs_{75}	0.64(26)	18.3668(15)	0.43	0.64(7)	18.3668(11)	0.37	0.64(4)	18.3668(12)	0.38
Fs_{83}	0.67(25)	18.3875(20)	0.11	0.73(7)	18.3872(15)	0.12	0.72(4)	18.3873(15)	0.11
Fs_{100}	0.81(46)	18.4188(38)	3.43	0.87(8)	18.4186(28)	2.33	0.87(6)	18.4187(28)	2.32

Data for samples Fs_0, Fs_{20}, Fs_{40}, Fs_{50}, Fs_{75}, Fs_{83} and Fs_{100} are taken from Yang and Ghose (1994).
- Indicates that the results obtained from the fitting lead to non-physical a values (see Angel et al., 2014b for further details).

Table 7c. Lattice parameter, b, thermal expansion fitting results for the samples in the present study together with those recalculated from the available literature data.

	Fei-type EoS			Fei-type EoS (with α_2=0)			Berman-type EoS		
	$\alpha_{b,303}$ ($\times 10^{-5}$ K^{-1})	b_0 (Å)	χ^2	$\alpha_{b,303}$ ($\times 10^{-5}$ K^{-1})	b_0 (Å)	χ^2	$\alpha_{b,303}$ ($\times 10^{-5}$ K^{-1})	b_0 (Å)	χ^2
DP N.1	0.89(23)	8.8799(4)	1.66	1.32(7)	8.8792(5)	3.62	1.32(4)	8.8792(5)	3.67
B22 N.60	1.10(19)	8.8781(4)	1.70	1.22(5)	8.8773(4)	1.75	1.22(3)	8.8778(4)	1.75
Fs_0	0.82 (9.67)	8.819(12)	0.00	1.04(92)	8.8186(96)	0.00	1.03(59)	8.8186(97)	0.00
Fs_{20}	1.06(24)	8.8616(9)	0.07	1.10(7)	8.8615(7)	0.07	1.09(4)	8.8615(7)	0.06
Fs_{40}	1.14(20)	8.905(6)	0.11	1.19(5)	8.9049(5)	0.13	1.19(3)	8.9049(5)	0.13
Fs_{50}	1.46(20)	8.936(8)	0.50	1.28(6)	8.9372(6)	0.68	1.28(4)	8.9372(6)	0.67
Fs_{75}	1.43(24)	9.0067(6)	0.31	1.45(6)	9.0067(5)	0.27	1.46(4)	9.0066(5)	0.28
Fs_{83}	1.29(22)	9.0291(8)	0.24	1.27(6)	9.0292(6)	0.21	1.28(4)	9.0286(7)	0.20
Fs_{100}	1.54(6)	9.0787(11)	1.21	1.53(8)	9.0787(10)	1.18	1.54(6)	9.0787(11)	1.21

Data for samples Fs_0, Fs_{20}, Fs_{40}, Fs_{50}, Fs_{75}, Fs_{83} and Fs_{100} are taken from Yang and Ghose (1994).
- Indicates that the results obtained from the fitting lead to non-physical a values (see Angel et al., 2014b for further details).

Table 7d. Lattice parameter, c, thermal expansion fitting results for the samples in the present study together withthose recalculated from the available literature data.

	Fei-type EoS			Fei-type EoS (with α2=0)			Berman-type EoS		
	$\alpha_{b,303}$ ($\times 10^{-5}$ K^{-1})	b_0 (Å)	χ^2	$\alpha_{b,303}$ ($\times 10^{-5}$ K^{-1})	b_0 (Å)	χ^2	$\alpha_{b,303}$ ($\times 10^{-5}$ K^{-1})	b_0 (Å)	χ^2
DP N.1	0.85(28)	5.2356(3)	2.15	0.92(6)	5.2357(3)	2.04	0.91(3)	5.2357(3)	2.03
B22 N.60	0.93(20)	5.2068(3)	1.43	0.90(4)	5.2068(2)	1.34	0.90(3)	5.2068(2)	1.38
Fs_0	-	-	-	0.95(1.43)	5.1791(98)	-	0.94(92)	5.1794(97)	-
Fs_{20}	0.91(23)	5.1933(5)	0.04	0.92(6)	5.1933(4)	0.04	0.90(4)	5.1931(4)	0.04
Fs_{40}	0.71(20)	5.2084(4)	0.27	0.80(6)	5.2082(3)	0.34	0.78(4)	5.2081(3)	0.28
Fs_{50}	0.81(19)	5.215(5)	0.10	0.82(6)	5.215(3)	0.09	0.81(4)	5.215(3)	0.10
Fs_{75}	0.72(24)	5.2281(4)	0.58	0.87(7)	5.2279(3)	0.72	0.86(4)	5.2279(3)	0.65
Fs_{83}	1.08(23)	5.2318(5)	0.41	0.98(6)	5.2319(4)	0.41	0.97(4)	5.2319(4)	0.48
Fs_{100}	-	-	-	0.79(15)	5.2369(11)	8.50	0.76(10)	5.2368(11)	8.58

Data for samples Fs_0, Fs_{20}, Fs_{40}, Fs_{50}, Fs_{75}, Fs_{83} and Fs_{100} are taken from Yang and Ghose (1994).
- Indicates that the results obtained from the fitting lead to non-physical a values (see Angel et al., 2014b for further details).

Acknowledgements

This work was supported by the ERC starting grant #307322 to F. Nestola.

References

Alvaro, M., Cámara, F., Domeneghetti, M., Nestola, F.and Tazzoli, V. (2011) HT P21/c-C2/c phasetransition and kinetics of

Fe^{2+}-Mg order-disorder of an Fe-poor pigeonite: implications for the cooling history of ureilites. Contributions to Mineralogy and Petrology, 162, 599-613.

Alvaro, M., Domeneghetti, M.C., Fioretti, A.M., Cámara, F. and Marinangeli, L. (2015) A new calibration to determine the closure temperatures of Fe-Mg ordering in augite from nakhlites. Meteoritics & Planetary Science, DOI: 10.1111/maps.12436.

Angel, R.J. and Jackson, J.M. (2002) Elasticity and equation of state of orthoenstatite, MgSiO3. American Mineralogist, 87, 558-561.

Angel, R.J., Gonzalez-Platas, J. and Alvaro, M. (2014a) EosFit7c and a Fortran module (library) for equation of state calculations. Zeitschrift fu¨r Kristallographie, 229, 405-419.

Angel, R.J., Mazzucchelli, M.L., Alvaro, M., Nimis, P. and Nestola, F. (2014b) Geobarometry from hostinclusion systems: the role of elastic relaxation. American Mineralogist, 99, 2146-2149.

Angel, R.J., Alvaro, M., Nestola, F. and Mazzucchelli, M.L. (2015) Diamond thermoelastic properties and implications for determining the pressure of formation of diamond inclusion systems. Russian Geology and Geophysics Journal, 56, 211-220.

Balic-Žunic, T. and Vickovic, I. (1996) IVTON – a program for the calculation of geometrical aspects of crystal structures and some crystal chemical applications. Journal of Applied Crystallography, 29, 305-306.

Bass, J.D. and Anderson, D.L. (1984) Composition of the upper mantle: Geophysical tests of two petrological models. Geophysical Research Letters, 11, 229-232.

Berman, R.G. (1988) Internally-consistent thermodynamic data for minerals in the system Na2O–K2O–CaO–MgO–FeO- Fe2O3–Al2O3–SiO2–TiO2–H2O–CO2. Journal of Petrology, 29, 445-522.

Blessing, R.H. (1995) An empirical correction for absorption anisotropy. Acta Crystallographica Section A, 51, 33-38.

Brown, P.E., Essene, E.J. and Peacor, D.R. (1980) Phase relations inferred from field data for Mn pyroxenes and pyroxenoids. Contributions to Mineralogy and Petrology, 74, 417-425.

Domeneghetti, M.C. and Steffen, G. (1992) M1, M2 site populations and distortion parameters in synthetic Mg-Fe orthopyroxenes from Mo¨ssbauer spectra and X-ray structure refinements. Physics and Chemistry of Minerals, 19, 298-306.

Domeneghetti, M.C., Molin, G.M. and Tazzoli, V. (1985) Crystal-chemical implications of the Mg^{2+}- Fe^{2+} distribution in orthopyroxenes. American Mineralogist, 70, 987-995.

Domeneghetti, M.C., Molin, G.M. and Tazzoli, V. (1995) A crystal-chemical model for Pbca orthopyroxene. American Mineralogist, 80, 253-267.

Domeneghetti, M.C., Fioretti, A.M., Ca´mara, F., Molin, G. and Tazzoli, V. (2007) Thermal history of ALH 84001 meteorite by Fe^{2+}-Mg ordering in orthopyroxene. Meteoritics & Planetary Science, 42, 1703-1710.

Domeneghetti, M., Fioretti, A., Ca´mara, F., McCammon, C. and Alvaro, M. (2013) Thermal history of nakhlites: A comparison between MIL 03346 and its terrestrial analogue Theo's flow. Geochimica et Cosmochimica Acta, 121, 571-581.

Fei, Y. (1995) Thermal expansion. Pp. 29_44 in: Mineral Physics and Crystallography: a Handbook of Physical Constants (T.J. Ahrens, editor). AGU Reference Shelf, Vol. 2. American Geophysical Union, Washington, DC.

Fioretti, A.M., Domeneghetti, M.C., Molin, G., Camara, F. , Alvaro, M. and Agostini, L. (2007) Reclassification and thermal history of Trenzano chondrite. Meteoritics & Planetary Science, 42, 2055-2066.

Frisillo, A.L. and Barsch, G.R. (1972) Measurement of single-crystal elastic constants of bronzite as a function of pressure and temperature. Journal of Geophysical Research, 77, 6360-6384.

Frisillo, A.L. and Buljan, S.T. (1972) Linear thermal expansion coefficients of orthopyroxene to 1000ºC. Journal of Geophysical Research, 77, 7115-7117.

Ganguly, J. and Domeneghetti, M.C. (1996) Cation ordering of orthopyroxenes from the Skaergaard Intrusion: implications for the subsolidus cooling rates and permeabilities. Contributions to Mineralogy and Petrology, 122, 359-367.

Gatta, G., Rinaldi, R., Knight, K., Molin, G. and Artioli, G. (2007a) In-situ high-temperature thermo-elastic behavior and structural response of a mantle orthopyroxene by neutron powder diffraction up to 1200ºC. Proceedings of the VI Congress of the ''Federazione Italiana di Scienze della Terra'' (F.I.S.T) _ Rimini (Italy), 12_14 September 2007.

Gatta, G.D., Rinaldi, R., Knight, K., Molin, G. and Artioli, G. (2007b) High temperature structural and thermoelastic behaviour of mantle orthopyroxene: an in situ neutron powder diffraction study. Physics and Chemistry of Minerals, 34, 185-200.

Hawthorne, F.C., Ungaretti, L. and Oberti, R. (1995) Site populations in minerals; terminology and presentation of results of crystal-structure refinement. The Canadian Mineralogist, 33, 907-911.

Howell, D., Wood, I.G., Dobson, D.P., Jones, A.P., Nasdala, L. and Harris, J.W. (2010) Quantifying strain birefringence halos around inclusions in diamond. Contributions to Mineralogy and Petrology, 160, 705-717.

Howell, D., Wood, I.G., Nestola, F., Nimis, P. and Nasdala, L. (2012) Inclusions under remnant pressure in diamond: a multi-technique approach. European Journal of Mineralogy, 24, 563-573.

Hugh-Jones, D. (1997) Thermal expansion of MgSiO3 and FeSiO3 ortho- and clinopyroxenes. American Mineralogist, 82, 689-696.

Ibers, J. and Hamilton, W. (1970) International Tables for X-ray Crystallography. Kynoch Press, Birmingham, UK [pp. 99-101].

Kanzaki, M. (1991) Stability of hydrous magnesium silicates in the mantle transition zone. Physics of the Earth and Planetary Interiors, 66, 307-312.

Kustowski, B., Ekstro¨m, G. and Dziewon´ ski, A. (2008) Anisotropic shear–wave velocity structure of the Earth's mantle: A global model. Journal of Geophysical Research: Solid Earth (1978-2012), DOI: 10.1029/2007JB005169.

Milani, S., Nestola, F., Alvaro, M., Pasqual, D., Mazzucchelli, M.L., Domeneghetti, M.C. and Geiger, C.A. (2015) Diamond-garnet barometry: The role of garnet compressibility and expansivity. Lithos, DOI: 10.1016/j.lithos.2015.03.017.

Miyake, A., Shimobayashi, N. and Kitamura, M. (2004) Isosymmetric structural phase transition of orthoenstatite: Molecular dynamics simulation. American Mineralogist, 89, 1667-1672.

Nestola, F. (2015) The crucial role of crystallography in diamond research. Rendiconti Lincei, DOI: 10.1007/s12210-015-0398-1.

Nestola, F., Gatta, G.D. and Ballaran, T.B. (2006) The effect of Ca substitution on the elastic and structural behavior of orthoenstatite. American Mineralogist, 91, 809-815.

Nestola, F., Nimis, P., Ziberna, L., Longo, M., Marzoli, A., Harris, J.W., Manghnani, M.H. and Fedortchouk, Y. (2011) First crystal-structure determination of olivine in diamond: Composition and implications for provenance in the Earth's mantle. Earth and Planetary Science Letters, 305, 249-255.

Pacalo, R. and Gasparik, T. (1990) Reversals of the orthoenstatite–clinoenstatite transition at high pressures and high temperatures. Journal of Geophysical Research: Solid Earth (1978-2012), 95, 15853-15858.

Pandolfo, F., Ca´mara, F., Domeneghetti, M.C., Alvaro, M., Nestola, F., Karato, S.-I. and Amulele, G. (2015) Volume thermal expansion along the jadeite-diopside join. Physics and Chemistry of Minerals, 42, 1-14.

Panning, M. and Romanowicz, B. (2006) A three dimensional radially anisotropic model of shear velocity in the whole mantle. Geophysical Journal International, 167, 361-379.

Perrillat, J.-P., Nestola, F., Sinogeikin, S.V. and Bass, J.D. (2007) Single-crystal elastic properties of $Ca_{0.07}Mg_{1.93}Si_2O_6$ orthopyroxene. American Mineralogist, 92, 109-113.

Petersen, E.U., Anovitz, L.M. and Essene, E.J. (1984) Donpeacorite, (Mn,Mg)MgSi2O6, a new orthopyroxene and its proposed phase relations in the system MnSiO3-MgSiO3-FeSiO3. American Mineralogist, 69, 472_480.

Ringwood, A.E. (1975) Composition and Petrology of the Earth's Mantle. McGraw-Hill, New York. Saxena, S.K., Domeneghetti, M.C., Molin, G.M. and Tazzoli, V. (1989) X-ray diffraction study of Fe^{2+}-Mg order-disorder in orthopyroxene. Some kinetic results. Physics and Chemistry of Minerals, 16, 421-427.

Sheldrick, G.M. (1996) SADABS. University of Göttingen, Germany.

Sheldrick, G.M. (2008) A short history of SHELX. Acta Crystallographica Section A, 64, 112-122.

Smyth, J. (1973) Orthopyroxene structure up to 850ºC. American Mineralogist, 58, 636-648.

Stimpfl, M. (2005) The Mn, Mg-intracrystalline exchange reaction in donpeacorite (Mn0.54Ca0.03 Mg1.43Si2O6) and its relation to the fractionation behavior of Mn in Fe,Mg-orthopyroxene. American Mineralogist, 90, 155-161.

Stimpfl, M., Ganguly, J. and Molin, G. (1999) Fe^{2+}-Mg order-disorder in orthopyroxene: equilibrium fractionation between the octahedral sites and thermodynamic analysis. Contributions to Mineralogy and Petrology, 136, 297-309.

Sueno, S., Cameron, M. and Prewitt, C. (1976) Orthoferrosilite: high-temperature crystal chemistry. American Mineralogist, 61, 38-53.

Tarantino, S.C., Domeneghetti, M.C., Carpenter, M.A., Shaw, C.J.S. and Tazzoli, V. (2002) Mixing properties of the enstatite-ferrosilite solid solution: I. A macroscopic perspective. European Journal of Mineralogy, 14, 525.

Yang, H. and Ghose, S. (1994) Thermal expansion, Debye temperature and Gruneisen parameter of synthetic (Fe,Mg)SiO3 orthopyroxenes. Physics and Chemistry of Minerals, 20, 575-586.

4. Elastic behaviour of grossular garnets at high pressures and temperatures

S. Milani[1], R.J. Angel[1], L. Scandolo[2], M.L. Mazzucchelli[2], T. Boffa Ballaran[3], S. Klemme[4], M.C. Domeneghetti[2], R. Miletich[5], K. S. Scheidl[5], M. Derzsi[1,6], K. Tokár[7], M. Prencipe[8], M. Alvaro[2], F. Nestola[1]

[1]Department of Geosciences, University of Padova, Via Gradenigo, 6, I-35131, Padova, Italy
[2]Department of Earth and Environmental Sciences, University of Pavia, Via A. Ferrata, 1, I-27100 Pavia, Italy
[3]Bayerisches Geoinstitut, Universität Bayreuth, 95440 Bayreuth, Germany
[4]Institut für Mineralogie, Westfälische Wilhelms-Universität Münster, Corrensstraße 24 - 48149 Münster, Germany
[5]Institut für Mineralogie und Kristallographie, Universität Wien, Althanstrasse 14, A-1090 Wien, Austria
[6]Centre for New Technologies, University of Warsaw, Żwirki i Wigury 93, 02089 Warsaw, Poland
[7]Institute of Physics, CCMS, Slovak Academy of Sciences, Dúbravská cesta 9, 84511 Bratislava, Slovakia
[8]Department of Earth Sciences, Via Valperga Caluso 35, I-10125 Turin, Italy

Accepted in: American Mineralogist
Running title: P-V-T-K fit on grossular

ABSTRACT

The elastic behaviour of synthetic single crystals of grossular garnet ($Ca_3Al_2Si_3O_{12}$) has been studied *in situ* as a function of pressure and temperature separately. The same data collection protocol has been adopted to collect both the pressure-volume (*P*-*V*) and temperature-volume (*T*-*V*) datasets in order to make the measurements consistent with one another. The consistency between the two datasets allows simultaneous fitting to a single pressure-volume-temperature equation of state (EoS). Validation of the results has been carried out with a new fitting utility implemented in the latest version of the program EoSFit7c. The new utility performs fully weighted *simultaneous* fits of the *P-V-T and P-K-T* data using a thermal pressure Equation of State combined with any PV EoS. Simultaneous refinement of our *P-V-T* data combined with that of K^T as a function of *T* allowed us to produce a single *P-V-T-K*^{T} equation of state with the following coefficients:

V_0 = 1664.46(5) Å^3, K_{T0} = 166.57(17) GPa and $K`$ = 4.96(7) $\alpha_{(300K,\ 1bar)}$ = 2.09(2)×10^{-5} K^{-1} with a refined Einstein temperature (θ_E) of 512K for a Holland-Powell-type thermal pressure model and a Tait 3rd-order EoS. Additionally, thermodynamic properties of grossular have been for the first time calculated from crystal Helmholtz and Gibbs energies, including the contribution from phonons, using density functional theory within the framework of the quasi-harmonic approximation.

Keywords: grossular, high-pressure, high-temperature, diffraction, bulk modulus, P-V-T-K fit, EosFit

INTRODUCTION

Stable over a wide range of pressure and temperature conditions, garnets are among the most abundant phases in the Earth's upper mantle and transition zone. Yet coherent and homogeneous equation of state coefficients to reliably describe their behaviour at simultaneous high pressures and temperatures still have to be determined with sufficient accuracy and precision. Recent papers have shown the importance of a robust and valid description of the elastic behaviour of the most abundant mineral phases for the accurate calculation of host-inclusion entrapment pressures that in turn allow the growth conditions in the Earth to be inferred (e.g. Angel et al. 2014, 2015a, 2015b; Ashley et al., 2015; Milani et al., 2015). However, the determination of a full set of elastic coefficients of a mineral is always challenging because of the limitations in performing simultaneous high-pressure (P) and temperature (T) experiments on one side and because of the lack of consistent measurements performed separately at high-P and high-T. Therefore, a reliable description of the elastic behaviour of minerals at high-P,T with a single set of Equation of State (EoS) coefficients can be extremely challenging.

Pressure-volume EoS are well-developed and are capable of reproducing the isothermal volume or density changes of materials to within the experimental uncertainties. A natural approach to describing the *P-V-T* behaviour of a material is therefore to describe how the volume (V_{0T}), bulk moduli (K_{0T}[1]) and its pressure derivatives (K_{0T}') change with increasing temperature (at room pressure), and then use these parameters to calculate the isothermal compression at the temperature of interest. A potential limitation of this approach is that while the variation of K_{0T} with T can be measured, the variation of K_{0T}' with T has been measured very rarely, although it is obvious that it should increase slightly with increasing temperature. As Helffrich and Connolly (2009) pointed out, the common assumption that K_{0T}' does not change with temperature in combination with the approximation that $\partial K_{0T}/\partial T$ is constant, often leads to the prediction of non-physical negative thermal expansion coefficients at reasonably modest pressures for a large number of materials. An alternative approach is to employ the idea of thermal pressure (e.g. Anderson, 1995). Then the total pressure (P) at a given V and T can be expressed as the sum of two terms:

$$P(V,T) = P(V,T_{ref}) + Pth(T)$$

The function $P(V,T_{ref})$ is the isothermal equation of state for the material at the reference temperature, up to the volume at P and T. As shown in the Fig. 1, if T > Tref, then $P(V,T_{ref}) <$

[1] Notation: subscripts on K (e.g. $K_{P,T}$) indicate the reference pressure and temperature to which the bulk modulus is referred; superscripts S or T (e.g. K^S or K^T) stand for adiabatic or isothermal quantities.

$P(V,T)$. The thermal-pressure $Pth(T)$ is the pressure that would be created by increasing the temperature from Tref to T at constant volume, which is the isochor of the material passing through the final P,T point of interest. As shown in Fig. 1, the concept of thermal pressure is therefore essentially a way of calculating P(V,T) along a different path in P-T space. We can consider that the isothermal compression part that gives us $P(V,T_{ref})$ is well-defined. The slope of the isochor is given by $\left(\frac{\partial P}{\partial T}\right)_V = \frac{\alpha}{\beta} = \alpha K^T$, so the thermal pressure is $Pth = \int_{Tref}^{T} (\alpha K^T)_V \, dT$. In order to use a thermal-pressure EoS one then has to know, or to make an assumption, about how the product αK^T varies along the isochor. For many materials and P,T ranges of interest (e.g. Figure 1) the temperatures are in the region of the Debye temperature, so the isochor is linear and thus αK_T is a constant. In this case $Pth \sim (\alpha K^T)_V (T - Tref)$.

A number of other assumptions or models of the behavior of the material can be made, including the Debye and similar models which make assumptions about the vibrational and hence thermal behavior of materials. Holland and Powell (2011) noted that the form of αK^T against temperature should have the shape of a heat capacity function and developed an approximation for the integral of αK^T that involves an Einstein function, as follows:

$$Pth = \alpha_0 K_{00} \left(\frac{\theta_E}{\xi_0}\right)\left(\frac{1}{\exp(\theta_E/T)-1} - \frac{1}{\exp(\theta_E/T_{ref})-1}\right)$$

with ξ_0 being the same as in the thermal expansion equation of (Kroll et al. 2012). This thermal-pressure model has the physically-correct properties that the product αK^T becomes constant at high temperatures while it decreases to zero at low temperatures. This means that both the bulk modulus K0T and the thermal expansion become constant at low temperatures, and both have an approximately linear variation with temperature above θ_E. The exact expressions for thermal expansion and bulk modulus as a function of temperature depend on the choice of isothermal equation of state, but at T_{ref} and zero pressure $\alpha = \alpha_0$ Holland and Powell (2011). In this study we used the Holland and Powell (2011) model of thermal pressure in combination with the Tait isothermal EoS (so as to maintain compatibility with Thermocalc (Holland and Powell 2011) to determine the EoS of grossular ($Ca_3Al_2Si_3O_{12}$) garnet. We show that the thermal pressure approach allows the full *P-V-T* EoS to be determined by fitting simultaneously measurements of the volume and bulk modulus over a range of temperature but only at room pressure. Additional separate measurements of the volume compression curve at high-P can be used to provide either an independent test of the EoS parameters, or be used to further constrain them in simultaneous global fits of all available data. This approach has the advantage of not requiring data from simultaneous high-P, high-T measurements which remain challenging with respect to both the control and

accurate measurement of *P* and *T*, and with respect to the precision in volume measurements. A comparison with previous literature data (e.g. Skinner, 1956; Isaak et al., 1992; Thieblot et al., 1998; Kono et al., 2010; Gwanmesia et al., 2014; Du et al., 2015 etc..) is provided together with a further crosscheck of our experimental data against the results obtained by density functional theory (DFT) ab-initio simulation. Thermodynamic properties of grossular have been calculated for the first time from crystal Helmholtz and Gibbs energies, including the contribution from phonons, using density functional theory within the framework of the quasi-harmonic approximation.

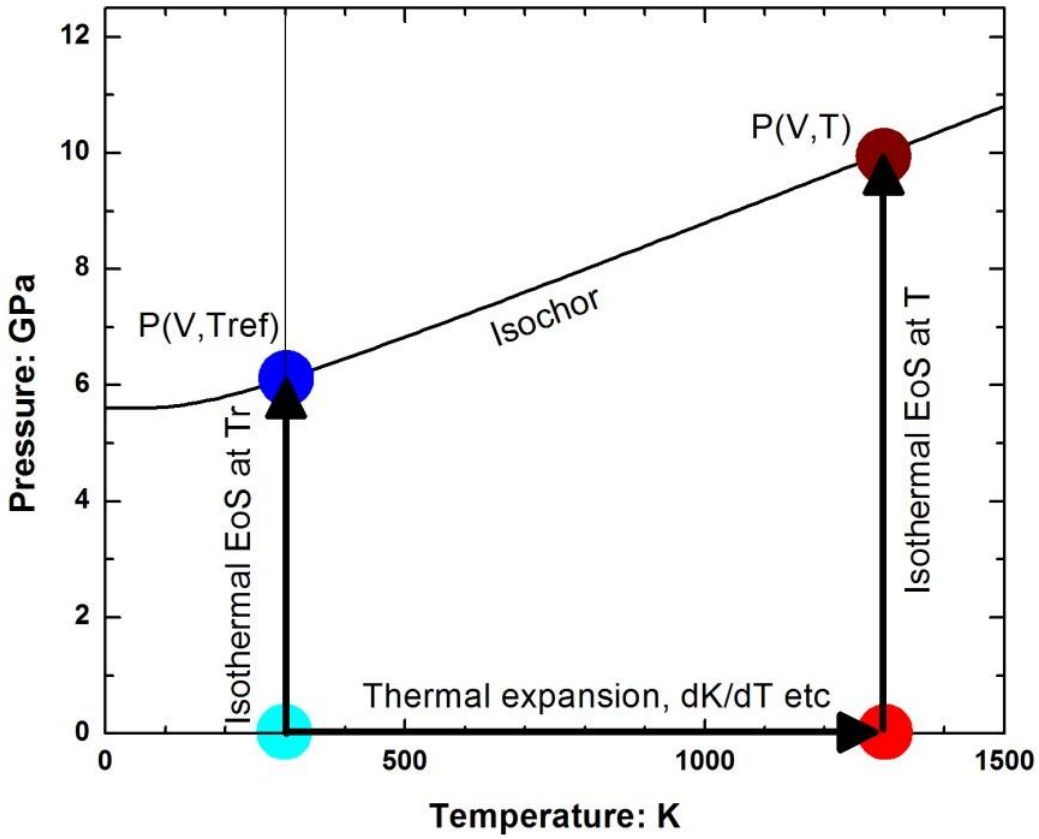

Fig. 1 Figure illustrating the two ways to calculate P-V-T properties.

Sample synthesis and characterization

Synthetic single crystals of pure end-member grossular (Gr_{100}) garnets were synthesized in at high pressures with a multi-anvil apparatus at the Bayerisches Geoinstitut. Stoichiometric mixtures of CaO (prepared by decarbonation of $CaCO_3$), $Al(OH)_3$ and SiO_2 were packed into platinum capsules of 3.5 mm length and 2 mm diameter. Samples were synthesized at 6 GPa and 1300°C. The experimental sample was heated in 23 mins and the temperature was kept at 1300°C for 40 mins. Each multi-anvil experiment was performed with Cr-doped MgO octahedra of 18 mm edge length combined with tungsten carbide cubes of 11 mm truncation-edge lengths. For all the experiments a graphite heater was employed. Experiments were quenched by cutting the electrical power supply to the furnace. Single-crystals of up to ca. 100 μm in diameter were recovered from the capsules. The compositions of the crystals have been determined by electron microprobe at the University of Padova using a Cameca CAMEBAX-micro operating at 15 nA and 15 kV with standards of andradite for Si, spinel for Al and diopside for Ca. Results from the chemical analyses are reported in Table 1. Two crystals (with size ca. 80 x 30 x 30 μm) were selected for the X-ray diffraction study based on the absence of twinning and visible inclusions and on the quality of their diffraction peak profiles (FWHM not greater than 0.15°).

Table 1 Averaged composition obtained from EMPA analyses on grossular synthetic single crystal garnets.

n. analyses		8	
	wt%		*a.p.f.u.*
SiO_2	40.13 (13)	Si	3.00(1)
Al_2O_3	22.33 (10)	Al	1.98(1)
CaO	37.83 (16)	Ca	3.04(1)
Total	100.32		8.01(1)

Standard deviations are given in parentheses.

Thermal expansion behaviour by single crystal X-ray diffraction experiments

The high-temperature single-crystal X-ray diffraction experiments were performed at the University of Pavia with a HUBER four-circle point detector diffractometer operating at 50 kV and 30 mA (Mo$K\alpha$ radiation) and equipped with a 0.8 mm short collimator and automated with the SINGLE software (Angel and Finger, 2011). This diffractometer is equipped with a newly designed micro-furnace controlled by a Eurotherm temperature regulator (Alvaro et al., 2015). For the high-T experiments, one single crystal of grossular was placed inside a thin-walled quartz vial (0.3 mm inner diameter and 26 mm long) and held in position by means of quartz wool. The vial was then mounted on a metal goniometer head on the diffractometer. During the high-temperature experiments the effects of the crystal offsets and the diffractometer aberrations were compensated by using the eight-position centring method (King and Finger, 1979) before starting the high-T measurement. The unit-cell parameters (Table 2 and Fig. 2) were determined at 23 different temperatures from room-T up to 1020 K using only 4-position centring because of the spatial restrictions described in Alvaro et al. (2015). A further 7 measurements were then made on cooling back to room temperature. Each individual measurement took about 12 hours, and the high-temperature experiment lasted for a total of 14 days. Unconstrained unit-cell parameters confirmed the cubic symmetry within 1 esd. Therefore only constrained unit-cell parameters obtained by vector least-squares fit (Ralph and Finger, 1982) are reported in Table 2. Unit-cell parameters determined on the heating and cooling cycles are indistinguishable.

The low-temperature single-crystal X-ray diffraction experiment was performed on the very same crystal used for the high-T experiment still mounted inside its quartz vial. The experiment was carried out at the Institut für Mineralogie und Kristallographie at the University of Wien using a Stoe StadiVari diffractometer equipped with an Incoatec IμS microsource (Mo-target, with multi-layer mirror optics, operating at 50KV and 0.1mA) and a Pilatus 300K area detector. The low-T was achieved using an Oxford Cryojet system that allows measurements to be performed between 100 and 500 K. Full intensity data collections up to 110° 2θ (with a coverage of 99% and redundancy higher than 4) were performed at 10 different temperatures from room-T down to 100 K. Correction of the crystal offsets from the goniometer center were made by first performing a short data collection and adjusting the crystal position to make the frame scale factors flat. Unconstrained unit-cell parameters confirmed the cubic symmetry within 1 e.s.d.; therefore, only constrained unit-cell parameters are reported in Table 2 and Fig. 2 together with those obtained at high-T.

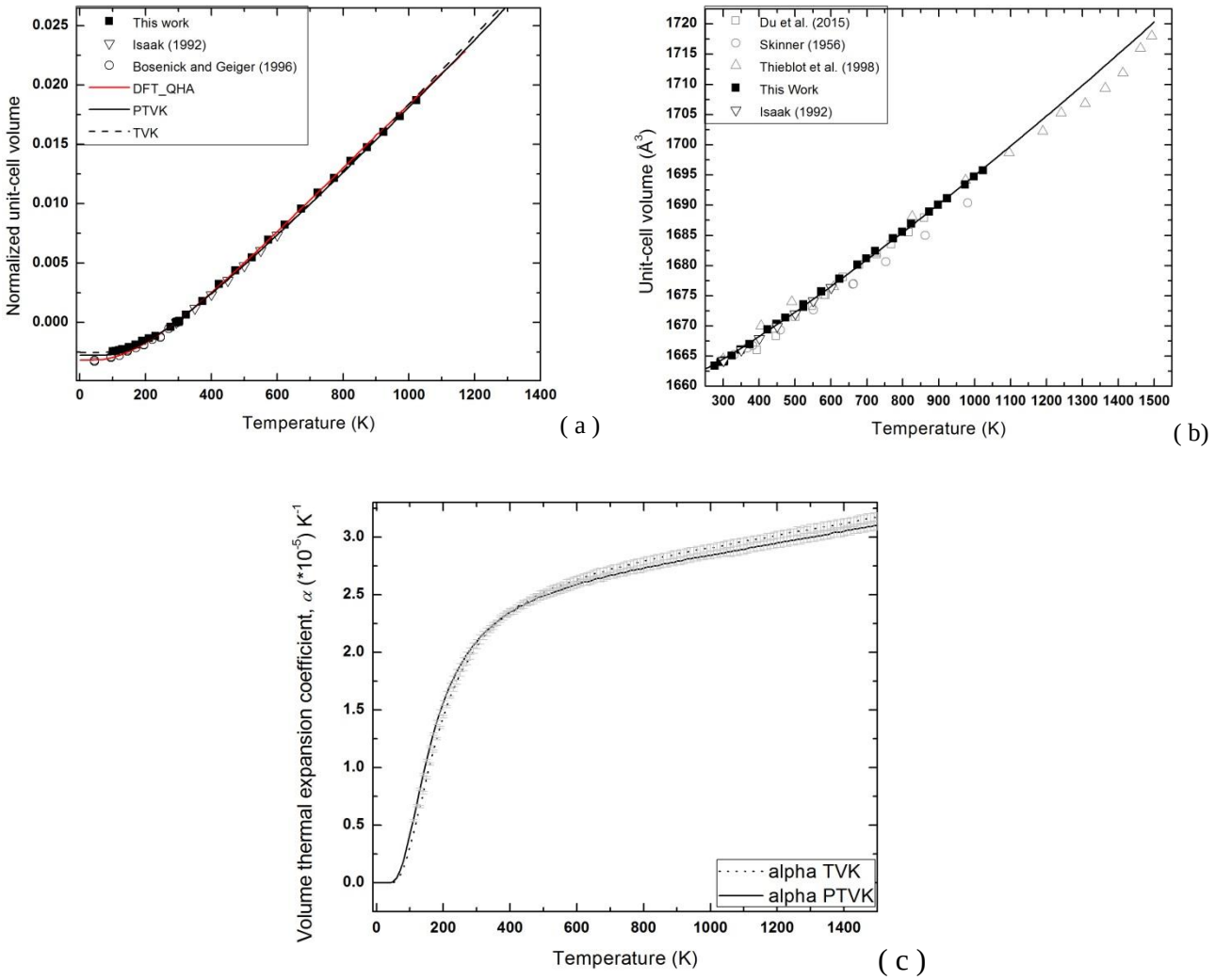

Fig. 2 Unit-cell volume and thermal expansion. In all graphs black solid line represent fitting results obtained on our data using the P-V-T-K approach, black dashed line those obtained from the T-V-K approach and red solid line those obtained from DFT calculations at 2GPa. The error bars are smaller than symbol size. (a) our data (solid symbol) together with the available low-T literature data (empty symbols); (b) Only the high-T regime (i.e. above room-T) for our data (solid symbol) together with the available high-T literature data (empty symbols); (c) Volume thermal expansion coefficient as a function of temperature obtained from the fitting of our data using P-V-T-K (solid line) and T-V-K (dashed line) fitting approach.

Table 2. Unit-cell edge and volume of grossular at different temperatures.

T (K)	*a* (Å)	V (Å^3)
100(2)	11.8403(13)	1659.92(33)
110(2)	11.8405(14)	1659.99(33)
120(2)	11.8407(13)	1660.10(32)
130(2)	11.841(13)	1660.20(33)
150(2)	11.8417(13)	1660.52(33)
170(2)	11.8425(14)	1660.84(34)
190(2)	11.8437(14)	1661.37(34)
210(2)	11.8446(14)	1661.75(34)
230(2)	11.8454(14)	1662.05(35)
276(2)	11.8485(15)	1663.36(37)
293(2)	11.8499(5)	1663.98(20)
301(2)	11.8500(12)	1664.01(29)
303(2)	11.8503(6)	1664.15(23)
323(2)	11.8525(6)	1665.04(25)
348(2)	11.8548(5)	1666.02(21)
373(2)	11.8570(6)	1666.95(24)
423(2)	11.8627(7)	1669.36(28)
448(2)	11.8648(5)	1670.26(22)
473(2)	11.8673(7)	1671.31(31)
523(2)	11.8716(12)	1673.12(49)
523(2)	11.8726(5)	1673.55(21)
573(2)	11.8776(6)	1675.65(26)
623(2)	11.8826(5)	1677.78(22)
673(2)	11.8880(5)	1680.08(22)
698(2)	11.8905(5)	1681.14(21)
723(2)	11.8934(5)	1682.38(23)
773(2)	11.8984(5)	1684.47(23)
798(2)	11.9009(5)	1685.53(22)
823(2)	11.9041(6)	1686.92(24)
873(2)	11.9088(6)	1688.90(25)
898(2)	11.9114(5)	1690.01(22)
923(2)	11.9139(5)	1691.09(23)
973(2)	11.9193(5)	1693.38(22)
998(2)	11.9224(5)	1694.69(21)
1023(2)	11.9248(5)	1695.71(22)

Note: Standard deviations are given in parentheses.

Compressibility behaviour by single crystal X-ray diffraction experiments

High-pressure single-crystal X-ray diffraction experiments for the grossular garnet were carried out with a Huber four-circle diffractometer at the Bayerisches Geoinstitut. The diffractometer operates at 50 kV and 40 mA (MoKα radiation), is equipped with a point detector and is automated by SINGLE software (Angel and Finger, 2011). The sample was loaded in a ETH-type diamond-anvil cell (DAC, Miletich et al., 2000) using a steel gasket, pre-indented to 100 μm thickness and with a hole diameter of 250 μm. Methanol:ethanol mixture 4:1 was used as pressure transmitting medium, which remains hydrostatic up to about ~ 9.5 GPa (Angel et al., 2007; Klotz et al., 2009). A single crystal of quartz was loaded in the DAC together with the sample and used as a pressure standard (Angel et al., 1997). During the centring procedure, the effects of crystal offsets and diffractometer aberrations were eliminated from the refined peak position by the eight-position centring method (King and Finger, 1979). Unconstrained unit-cell parameters were obtained by vector least-squares fit (Ralph and Finger, 1982) on not less than 20 reflections up to $2\theta = 29°$. The symmetry-unconstrained unit-cell edges show deviations smaller than 1 e.s.d. from the constrained ones thus confirming the cubic symmetry within 1 e.s.d.. Therefore, only the constrained unit-cell parameters have been reported in Table 3 and Fig. 3.

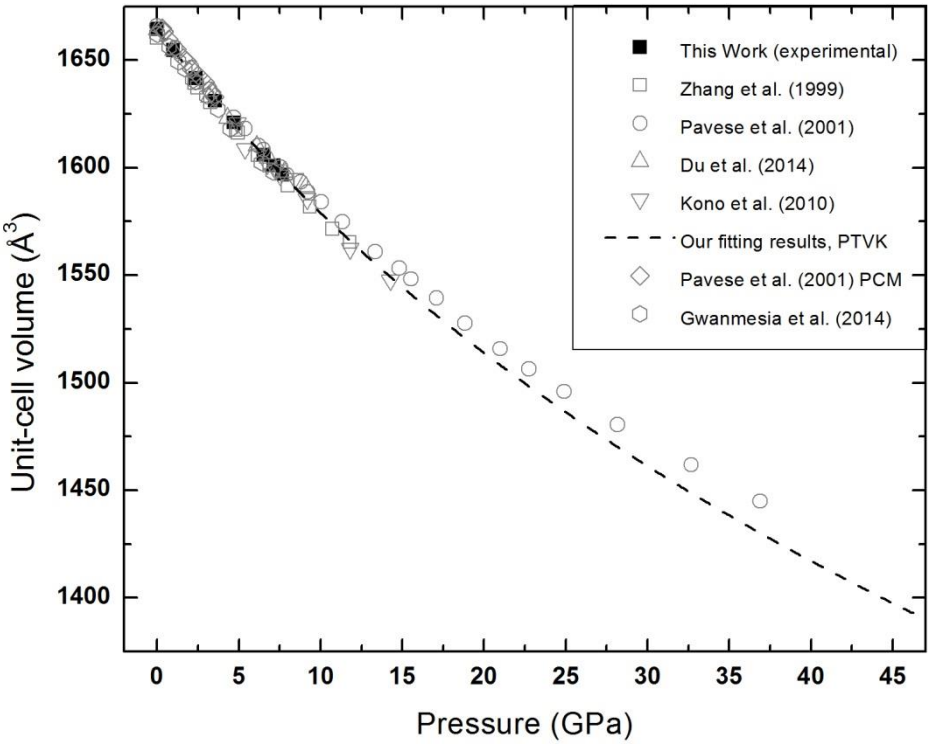

Fig. 3 Pressure-volume data for grossular available in literature (empty symbol) together with the data from this study (filled symbol). The dashed line epresents the fitting of our data to a 3rd – order Tait EoS. The error bars are smaller than the symbol size.

Table 3. Unit-cell edge and volume at different pressures.

P (GPa)	*a* (Å)	V (Å^3)
0.0001(1)	11.8508(3)	1664.34(14)
1.013(9)	11.8275(4)	1654.55(15)
2.392(10)	11.7963(4)	1641.47(15)
3.568(10)	11.7712(3)	1631.04(13)
4.715(11)	11.7469(3)	1620.95(13)
6.559(15)	11.7101(4)	1605.76(15)
7.149(12)	11.6986(3)	1601.05(14)
7.674(19)	11.6886(5)	1596.95(19)

Standard deviations are given in parentheses.

Fitting of the pressure-volume-temperature-modulus data using EoSFit7c

All fits described in this manuscript have been performed with the EosFit7c program (Angel et al., 2014). Previous versions of this program were able to fit isothermal EoS, thermal expansion models and the thermal-pressure EoS of Holland and Powell (2011) to *P-V*, *V-T* or *P-V-T* data, by the method of least-squares. We have now extended the capabilities of EosFit-7c to also fit all of these forms of EoS to bulk and linear moduli, either alone or in combination with volume or unit-cell parameter data. Fits are performed by weighted non-linear least squares to minimise the residuals P_{obs}-P_{calc}, using the effective variance method (Orear, 1982) to convert the experimental uncertainties in volume and bulk moduli, pressure and temperature of each datum into an effective uncertainty in *P* (Angel, 2000). Input bulk moduli can be either adiabatic (K^S) or isothermal values (K^T), but in either case they must be Reuss values, corresponding to the response of the material under hydrostatic pressure. The Voigt and Reuss bulk moduli of a material quantify its volume response to the application of uniform strain and uniform stress (hydrostatic pressure) respectively. When uniform stress is applied to a cubic material, it undergoes isotropic (i.e. uniform) strain. Therefore, the Voigt and Reuss bulk moduli of a cubic material are identical. We remind the reader that this is not true for materials of lower symmetry and therefore the use of Voigt values, or Voigt-Reuss-Hill averages, in Equations of state of crystals with symmetry lower than cubic is inconsistent with the theory underlying equations of state under hydrostatic conditions, and will lead to incorrect results (e.g. Angel et al., 2009).

If the input moduli to EosFit7c are isothermal, no further conversion is made, and the observational equations for such data in the least-squares are simply the expression for the bulk modulus in terms of pressure for each EoS. These expressions are direct for invertible EoS such as the Murnaghan or Tait EoS (Freund and Ingalls, 1989; Holland and Powell, 2011; Angel et al. 2014). For non-invertible EoS the procedure used is to calculate the compression ratio V/V_{00}

corresponding to the observed *K* and then use the *P*-*V* expression of the EoS to calculate the corresponding pressure. If adiabatic moduli are provided as input data, they are converted to isothermal values by $K^S = (1+\alpha_V \gamma T)K^T$ where the value of thermal expansion (α_V) is taken from the current EoS at the pressure and temperature of interest. The Grüneisen parameter γ can be expressed in terms of measurable quantities, such as for example $\gamma = \frac{\alpha_V K^S}{C_p} = \frac{\alpha_V K^T}{C_V}$. However, since heat capacity data is not available at elevated pressures, in EosFit7c we use the simple approximation (Anderson 1996) that $\gamma(P,T) = \gamma_0 \left(\frac{V(P,T))}{V_0} \right)^q$, with the value of *q* close to 1 for 'normal' solids under modest *P*,*T* conditions. Only Boehler and Ramakrishnan (1980) and Boehler (1982) appear to have attempted to measure the value of *q*, showing that it scales with volume. This means that the Grüneisen parameter scales with volume, increasing with increasing temperature and decreasing upon compression, which when considered as a measure of the pressure-dependence of the frequencies of vibrational modes, is reasonable. This will break down when the material becomes very anharmonic, near to structural phase transitions, but should not be a problem for materials such as the grossular garnet in this study. The value of γ_0 (i.e. γ value at the reference conditions) and of *q* can be set by the user in Eosfit7c.

For linear moduli that describe the variation of the unit-cell parameters with pressure as $M_i^T = -a_i \frac{\partial P}{\partial a_i}$, the procedure is analogous to that used for linear dimensions in EosFit7 (Angel et al., 2014). Internally the linear moduli are converted to volume-like bulk moduli as $K_i = \frac{M_i}{3}$ and treated with volume EoS. For the conversion of adiabatic to linear moduli, we use the relationship between isothermal and adiabatic compressibilities $\beta_i^T = \beta_i^S + \frac{\alpha_i \alpha_V T}{C_p}$ which can be derived from the fundamental relationship between isothermal and adiabatic elastic compliances $s_{ijkl}^T = s_{ijkl}^S + \frac{\alpha_{ij}\alpha_{kl}T}{C_p}$ with the C_p in units of $Jm^{-3}K^{-1}$ (Nye, 1985). The substitution $\frac{\gamma}{K^S} = \frac{\alpha_V}{C_p}$ gives $\beta_i^T = \beta_i^S + \frac{\alpha_i \gamma T}{K^S} = \beta_i^S \left(1 + \frac{\alpha_i \gamma T \beta_V^S}{\beta_i^S} \right)$ which can be rewritten in terms of moduli as $M_i^S = \left(1 + \alpha_i \gamma T \frac{M_i^S}{K^S} \right) M_i^T$. It is important to notice that for cubic materials $\alpha_i = \alpha_V / 3$ and $\frac{M_i^S}{K^S} = 3$

so that only for cubic materials this can be written as $M^S = (1+\alpha_v \gamma T) M^T$ which is the same relation as for the bulk moduli.

Ab-initio DFT (Density Functional Theory)

Ab-initio calculations have been performed in order to crosscheck our experimental results at simultaneous high-P and T. Thermodynamic properties of grossular have been calculated from crystal Helmholtz and Gibbs energies, including the contribution from phonons, using density functional theory (DFT) within the framework of the quasi-harmonic approximation (QHA). Periodic DFT calculations were performed with the plane-wave VASP package (Kresse and Furthmüller, 1996) within GGA approximation (Perdew et al., 1996), with projector-augmented waves (PAW, Blöchl, 1994) and the PBEsol functional (Perdew et al., 2008). A plane-wave cutoff of 520 eV and 2x2x2 k-mesh was used both for unit cell optimization and subsequent calculation of interatomic forces. The cell was optimized at several pressure points within the range [-8 to 8GPa]. Phonon frequencies at constant cell volumes were obtained by diagonalization of dynamical matrices whose elements were calculated using density functional perturbation theory (DFPT, Baroni et al., 2001). The matrices were constructed from interatomic force constants taking into account symmetries of the conventional body-centered cell of the garnet, containing 160 atoms. Phonon densities of states were determined by sampling the Brillouin zone (BZ) using Parlinski-Li-Kawazoe method (Parlinski et al., 1997) as implemented in the Phonopy code (Togo and Tanaka, 2015). The results obtained with DFT-GGA commonly overestimate cell volume values, and thus properties, with respect to experimental results. In our case, the DFT calculations yielded volume values of 1664.6 $Å^3$ (static DFT), 1681.9 $Å^3$ (zero-point vibration included) and 1687.3 $Å^3$ (T=290 K) which differ from experimental values of 1664.3 Å at room *P* and *T*, (0.0001 GPa and 300 K) within 0.0 %, 1.1% and 1.4% respectfully. This volume overestimation amounts to about -2 GPa, on the pressure scale, with respect to the experimental datum.

RESULTS

Temperature-volume data

The room-PT unit-cell volumes (V_{00}) of grossular as determined in this study, agree with one another to better than 1 e.s.d. thus confirming the reliability of the unit-cell lattice determination with different instruments and measurement protocols. Therefore, we combined the high-T measurements together with those at low-T in a single dataset without any normalization or re-scaling. The evolution of the unit-cell volume with temperature is reported in Fig. 2 and Table 2 where the low-T and the high-T data are reported together. A continuous increase of the unit-cell volume is observed as a function of temperature with no evidence of any irreversible change in the crystal occurred up to the maximum temperature reached in this study. Data collected both with increasing and decreasing temperature overlap within experimental error, thus indicating good experimental reproducibility. The temperature-volume data for the entire range of T studied were fit using the software EoSFit7c (Angel et al., 2014) using a Kroll-type EoS (Kroll et al., 2012) allowing for refinement of the Einstein temperature (θ_E) but not refining K′ value that was kept fixed to 5 (i.e. value from compressibility data, see the following sections). The thermal expansion coefficients obtained were $\alpha_{(298K,\ 1bar)}$ = 2.08(2)×10^{-5} K^{-1}, V_{00} = 1664.45(7) Å^3 with θ_E= 515(20) K. We compared our T-V for grossular with those from Isaak (1992) determined by dilatometry. Isaak et al. (1992) measured physical expansions, and converted such values to volume expansions Yv(obs). Conversion of Isaak et al. (1992) data (taken from their Table 2 reported in their paper) to unit-cell volumes has been performed according to $V = V_0(1 + Y_V obs)$. In order to ensure that our measurements and those by Isaak et al. (1992) were on the same volume scale we used our V_{00} at the same reference temperature of 293K used by Isaak et al. (1992). A plot of the two datasets (see Fig. 2) shows that they agree within their mutual uncertainties.

Temperature-volume-bulk modulus data

Isaak et al. (1992) also determined the adiabatic bulk modulus of grossular by RUS measurements and then used measured heat capacity data and his own thermal expansion data to also calculate the isothermal bulk modulus at each measurement temperature by means of $K^S = (1 + \alpha_V \gamma T)K^T$, using the value of the Grüneisen parameter $\gamma = \frac{\alpha_V K^S}{C_p}$. The reliability of the heat capacity (C_p) data by Isaak et al. (1992) has been confirmed by comparison with the more recent data by Bosenick et al. (1996) (see Fig. 4). The C_p values determined by Isaak et al. (1992)

fall well within the scatter of the data determined by Bosenick et al. (1996) and are also in good agreement with those we have obtained from the DFT calculations.

Using K and V data as a function of T it is obviously possible to refine V_{00}, α_0, θ_E and K_{00} . But in addition it is possible and required to refine K' because this affects the results when using the thermal pressure model as it appears in the isothermal EoS $P(V,T_{ref})$, and at room pressure $P(V,T_{ref})=-Pth(T)$. Simultaneous refinement of our T-V data and the T-K^S data from Isaak et al. (1992) for grossular using γ_0=1.22 and q=0 (i.e. γ=γ0) yielded identical results as to those obtained from fitting the T-V-K^T data (see Table 4[2]). This shows that the assumption that γ is constant is a reasonable approximation for grossular. This observation is also in agreement with Isaak et al. (1992) who calculated that γ drops by 0.1(± 0.05) over the temperature range from 300K to 1200K and with our results from DFT calculations as shown in Fig. 4 according to which γ drops to 1.24 at 650K and then it assumes constant values (e.g. changes of about 2 at the 3rd decimal place) above 650K.

[2] The Equation of State coefficients reported in Table 4c representing the best fit of our data have been deposited as supplementary material in the form of .eos files (that can be read with EoSFit7c). They are also available directly from the authors.

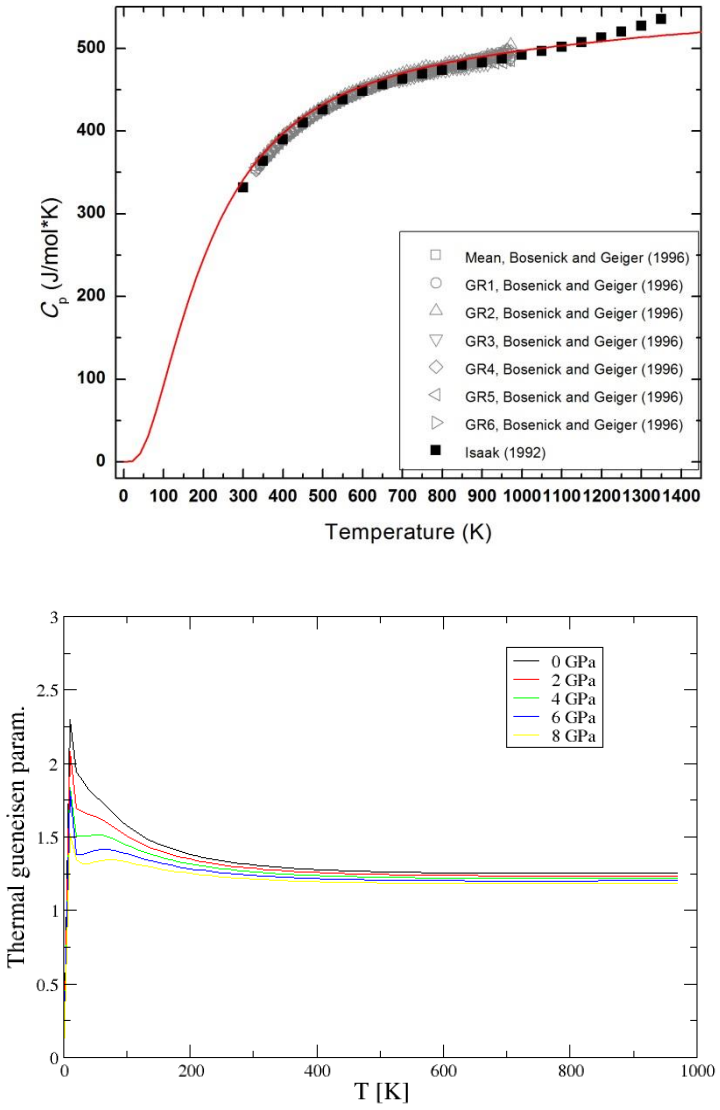

Fig. 4 (a) Heat capacity (Cp) values used in this work as determined by Isaak (1992) compared with the recent data by Bosenick and Geiger (1996). Also data obtained from DFT calculations are shown with the red solid line. (b) Gruneisen parameter as a function of temperature for different pressures as obtained from the DFT calculations.

Pressure-volume data

The unit-cell volume decreases smoothly with increasing pressure, as shown in Fig. 3 and reported in Table 2, up to the maximum hydrostatic pressure reached in this study of ~7.5 GPa. Such pressure covers the stability pressure range for upper mantle garnets. Fit of the *P-V* data alone using a 3rd order Tait EoS yielded the following coefficients: V_{00} = 1664.36(7) Å^3, K_{00} = 167.45(1.04) GPa and K_{00}` = 4.93(31) also reported in Table 4a. The goodness of the fit results was confirmed by the low ΔP_{max} value (calculated as $|P_{obs} - P_{calc}|$) of 0.010 GPa. The equation of state coefficients obtained with this method agree with those obtained by *T-V-K* fitting to better than 1 e.s.d. thus confirming the reliability of the results from the two fitting approaches.

Table 4a. Literature bulk moduli for grossular. The K_{0T} obtained by DFT have been extrapolated from 0 K to room temperature conditions (see text).

	Expermental method	V_0 (Å^3)	K_{T0} (GPa)	K'	Pressure medium	P_{max}(GPa)	Synthesis Method
Isaak (1992)	RUS	-	166.4(0.7)	-	-	-	
Zhang et al., 1999	X-ray single crystal diffraction	1660.218(337)	170(4)	5.2(6)	Ne	11.8	synthesized hydrothermally at high pressure and temperature in a piston cylinder device (Armbruster et al., 1992)
Akhmatskaya et al., 1999	DFT	1667.0	166(2)	4.26(11)	-	-	-
Nobes et al., 2000	DFT	1666.96	166	4.3	-	100	-
Mittal et al., 2001	lattice dynamic calculation	1665.18	170.41	-	-	-	-
Kono et al., 2010	Ultrasonic wave velocity	-	170.3(8)	4.43(7)	MgO+NaCl sleves	17	Hot-pressed glass with grossular composition at ~7 GPa and ~1 673 K for 2 h using a 3 000-ton high-pressure apparatus
Kawai et al., 2012	DFT	-	176.5	4.43	-	30	-
Erba et al., 2014	DFT	-	169.3	-	-	-	-
Pavese et al. (2001)	Powder diffraction	1666.3(3)	168.2(1.7)	5.9(2)		37	Pressure calibrant NaCl
Du et al. (2014)	Synchrotron X-ray powder diffraction	1664.3(3)	163.4(1)	5.92*	4:1 mixture of methanol:ethanol		anhydrous glass starting material in a multi-anvil (MA) 6GPa and 1400±2°C for 0.5h

Gwanmesia et al. (2014)	transfer-function ultrasonic interferometry plus energy-dispersive synchrotron X-ray in MA apparatus		169.5(2)	4.47(1)			Polycrystals hot-pressed in a 2000-ton uniaxial split-sphere apparatus at 15 kbar and nominal temperature 1000–1040°C for 7 h.
This study	X-ray single crystal diffraction	1664.36(7)	167.45(1.04)	4.93(31)	methanol:ethanol (4 : 1)	7.7	Oxide mixture at 6 GPa and 1300°C in a multi-anvil press

Note: * value not refined

Table 4b. Thermal expansion behaviour of the grossular garnet fitted by a Fei-type EoS at 300 K.

$V_{303\ K}$ calculated (Å^3)	$\alpha_{298K,1bar}$ x10^{-5} (K^{-1})	a_0 x10^5 (K^{-1})	a_1 x10^{10} (K^{-2})	a_2 (K)	EoS formalism	Reference
1664.2(1)	2.3(3)	2.84(32)	-0.2(3)	-0.4(3)		This work
1664.3(1)	1.7(4)	1.9(5)	0.8(5)	-0.4(4)	Fei-type[4]	Skinner (1956)[1]
1505.2(9)	1.7(6)	2.5(6)	30(50)	-0.9(10)		Thieblot et al., (1998)[2]
1664.3(3)	0.7(1.7)	6.60(18)	-4(2)	-4.1(15)		Du et al., (2015)[3]
1664.45(7)	2.08(2)[5]				Kroll-type	This work[6]

Note: [1]data have been fitted to the entire range of temperature (284 K to 980 K); [2]data have been fitted to the range of temperature between 300K-1453K not considering 3 outliers; [3] data have been fitted to the entire temperature range (296 K – 859 K) excluding two outliers. [4]Fei-type coefficients reported are calculated using as T_{ref} the first experimental temperature collected for each dataset; [5]θ_E=515(20) has been refined during fit; [6]EoS coefficients file (.eos) readable from EoSFit7c has been deposited as a supplementary material and is also available from the authors.

Table 4c. Equation of State (EoS) cofficients obtained from simultaneous fitting of the P-V-T-K data. For all the datasets here reported a themal pressure EoS has been combined to a 3rd order Tait EoS.

Fitting type	V_0 (Å^3)	K_{T0} (GPa)	K'	α	T_E	Reference
T-V-K^S	1664.18(3)	166.0(3)	4.73(15)	2.043(19)	567(13)	This study
T-V-K^T	1664.18(3)	166.0(3)	4.60(14)	2.043(19)	569(13)	This study
P-V-T-K^T	1664.46(5)	166.57(17)	4.96(7)	2.09(2)	512(19)	This study
P-V-T	1664.44(6)	166.1(1.1)	5.2(3)	2.09(2)	512*	
P-V-T-K^T	1667(6)	153(24)	6(3)	2.2(4)	512*	Kono et al., (2010)
P-V-T-K^T	1658.3(1.0)	167(2)	4.8(4)	1.58(13)	512*	Gwanmesia et al., (2014)

Note: *Value fixed in the refinement; γ and *q* values fixed as described in the text.

P-V-T-K and PVT Equation of State

The remarkably good agreement between the lattice parameters as determined with different experimental settings and that of the EoS coefficients obtained with different procedures allowed us to perform a simultaneous refinement of the entire set of EoS coefficients by combining our pressure-volume and temperature-volume data together with those of temperature-bulk modulus (Isaak et al. 1992) into a single dataset. Fully weighted simultaneous fit of the *P-V-T-K* data has been performed using a thermal pressure Equation of State with a 3rd order Tait EoS, allowing simultaneous refinement of V_{00}, K_{00}, K_{00}', α_0 and θ_E. As expected, the resulting coefficients V_{00} = 1664.46(5) Å^3; K_{00}=166.57(17) GPa; K_{00}'=4.96(7); $\alpha_{(298K,\ 1bar)}$ = 2.09(2)×10^{-5} K^{-1}, with θ_E= 512(19)K (γ_0=γ=1.22) agrees within 2 σ to those from *P-V* and *T-V-K* separately (see Table 4). At this point it is important to point out that the main difference between the *P-V-T-K* and *T-V-K* fits can be seen in the description of the bulk moduli as a function of *T* (Fig. 5a). It should be clear from Fig. 5a that while in the thermal regime between room-T and the maximum temperature reached with the experiments the bulk moduli calculated from the *T-V-K* and *P-V-T-K* Equations of State agree within mutual uncertainties, in the low-T regime much larger discrepancy are observed. These discrepancies are due to the different values of θ_E in the two EoS.

Simultaneous refinement of the *P-V-T* data alone yielded the following coefficients V_{00} = 1664.44(6) Å^3; K_{00}=166.19(1.25) GPa; K_{00}'=5.14(40); $\alpha_{(298K,\ 1bar)}$ = 2.09(2)×10^{-5} K^{-1}, with θ_E= 512K (not refined). Standard deviations on the bulk modulus (K_{0T}) and its first derivative (K') obtained from the *P-V-T* fitting are 6-8 times larger than those from the *P-V-T-K* ones and, when considered, the resulting coefficients from the *P-V-T* fit agree within 1 sigmas with those obtained from the *P-V-T-K* fits. The *P-V-T* results are not showed in Fig. 5a for sake of clarity, however, the resulting bulk moduli as a function of *T* agrees with the experimental data within 1σ.

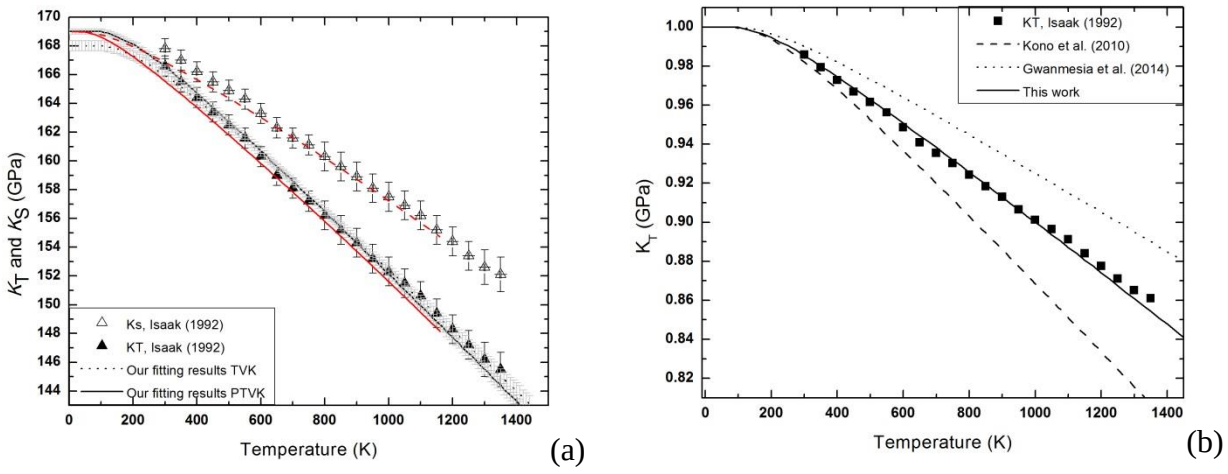

Fig 5. Bulk modulus evolution with temperature. (a) Isothermal (KT) and adiabatic (Ks) bulk moduli from Isaak (1992) together with those from T-V-K and P-T-V-K fitting of our data and the DFT obtained as described in the text; (b) normalized experimental isothermal bulk modulus (KT, solid symbols) together with the extrapolation of our fitting results (obtained from P-T-V-K fit, solid line) and those obtained with the same method from the data from Kono et al. (2010) and Gwanmesia et al. (2014) (dashed and dotted line, respectively). Agreement between the extrapolation of our at high-T and the experimental data by Isaak (1992) is remarkable whereas there are large differences between our data and those obtained with the same fitting approach on the data buy Kono et al (2010) and Gwanmesia et al. (2014).

DISCUSSION

Thermal expansion: comparison with literature data

The measured room temperature-pressure volumes (V_{00}) reported in this study are in good agreement with those previously reported in literature by several authors (see Table 4a and b). So far, only few x-ray diffraction thermal expansion data are available for grossular garnet (e.g. Skinner, 1956; Bosenick and Geiger, 1997; Thieblot et al., 1998; Du et al., 2015) and most of them have been obtained by means of powder X-ray diffraction. Data from Du et al. (2015) and those by Skinner (1956) have been re-fitted to their entire temperature range 296 K - 859 K (excluding two outliers at 393 K and 477 K) and 284 K-980 K, respectively. On the other hand, data from Thieblot et al. (1998) have been fitted from 300 K to 1453 K (i.e. well below the decomposition temperature) excluding a few outliers at 607 K, 724 K, and 1241 K. The results of all the extrapolations at 300 K are reported in Table 4b and shown Fig. 2. As shown in Table 4b, there are considerable differences between our data and those available in literature. These can be most likely ascribed to the compositional differences between the various samples and/or to the uncertainties given by the different experimental methods. For example, both Skinner (1956) and Thieblot et al. (1998) used grossular-rich samples for their investigation. For sake of

comparison, regardless the compositional differences, these literature data have been re-fitted to Fei-type EoS (Fei, 1995). Results from the fitting are reported in Table 4b, and Fig. 2.

As shown in Fig. 2, our data for the low-T regime are in good agreement with those reported by Bosenick and Geiger (1997) if their most scattered data (e.g. 195, 220 and 295 K) are not considered and with our results obtained by DFT simulation (red line in Fig. 2a).

The thermal expansion coefficients at 300 K from both Skinner (1956) and Du et al. (2015) are smaller than those calculated from our fitting. The discrepancies between our dataset and that by Skinner (1956) could be ascribed to the differences in composition as their sample referred to as a 'grossularite' has not been properly characterized. The thermal coefficient value obtained fitting the data by Du et al. (2015) is not reliable as demonstrated by the negative thermal expansion coefficients at high-T (regardless the Equation of State model chosen). The same is true also for the data reported by Thieblot et al. (1998), where the thermal expansion value decreases with increasing temperature. Our datasets, ranging from 100 K to about 1000 K, allowed performing fit to a Kroll-type EoS (Kroll et al. 2012), leading to a much more reliable description of the thermal behaviour of grossular. The reliability of the Einstein temperatures used (θ_E=569(13) K) have been confirmed by comparison with the saturation temperature (where $T_{sat} \approx \theta_E/2$) obtained from the fitting of the low-*T* data alone (T_{sat}=270(6) K) using a Salje-type EoS (Salje et al. 1991). The agreement within 1 sigma is also achieved when comparing with the θ_E from the *P-V-T-K* fit [θ_E=512(19) K, see Table 4c]

Compressibility: comparison with literature data

The elastic coefficients for grossular have been determined in several studies using different methods (e.g. ultrasonic wave velocity, static compression experiments in diamond-anvil cell, ab-initio calculations) as summarised in Table 4a. For purpose of comparison with the literature data, the adiabatic bulk modulii (K^S) obtained by means of ultrasonic wave velocity techniques have been converted to K^T.

DFT calculations of a P(V) curve, fitted by a third order Birch-Murnaghan EoS, provide a value of 156 GPa for the bulk modulus K^T at 300K, and a K' of 4.22. The *static* (no zero point and thermal effects included) and the *athermal* (zero point corrected and a temperature of 0K) values are respectively 163.9 and 160.1 GPa (K' fixed at 4.22: the value we obtained at 300K). These results are in line with the *standard* performances of DFT-GGA Hamiltonians like PBEsol, as they generally underestimate bulk moduli by about 10 GPa at room temperature. Another DFT study from the literature (Erba et al., 2014) provided a somewhat higher bulk

modulus (171 GPa), but that was a result from a static calculation and the Hamiltonian employed was an hybrid HF/DFT one (B3LYP) which includes an Hartree-Fock correction to the DFT-GGA electronic exchange functional. Indeed, such correction proved to be crucial to compute bulk moduli (and vibrational frequencies) very close to the experimental data (Prencipe et al. 2009, 2011, 2012, 2014), but it is computationally very costly if a plane-wave basis set is used, as in the present case, and therefore it cannot be afforded. The largest discrepancy in grossular bulk modulus value is with respect to the lattice dynamical calculation results published by Kawai and Tsuchiya (2012). Furthermore, the first derivative of the bulk modulus (K′) which we could now reliably refine clearly demonstrate that the correct value must be very close to 5 in agreement with some of the previous studies (see Table 4a).

Full elastic behaviour (P-V-T-K): comparison with literature data

The new utility available in EoSFit7c allowed us to also apply the same method described in the sections above (*P-V-T-K* fitting) to the available literature data obtained from independent elastic measurements and PVT datasets (Kono et al., 2010; Gwanmesia et al., 2014). It is remarkable the extra constraint given by the simultaneous weighted fit of the *K* data (see results in Table 4c) which however applied to the literature dataset does not allow to obtain the same quality as for our elastic coefficients due to the lack of data in the low-temperature regime. This combined with the much lower accuracy and precision that in most cases arises by the limitation of the *P-V-T* simultaneous measurements (i.e. pressure calibrant, pressure transmitting media etc..) give rise to discrepancies such as those showed in Fig. 5b. In this case the discrepancies in bulk modulus values at high-T reach up to 4% (more than 6 GPa at 1400 K). Furthermore, the low-T behaviour described using our *P-V-T-K* coefficients is reasonably confirmed by cross-check with the DFT results

CONCLUSIONS AND IMPLICATIONS

It is obvious that pressure-volume or temperature-volume measurements alone do not provide strong constraints on the cross-terms in *P-T* space (e.g. $\partial K/\partial T$ or $\partial \alpha/\partial P$) which are fundamental for the description of the elastic properties of a material at simultaneous high-P and high-T. Limitation in experimental measurements and/or in the description of the pressure-volume-temperature data (e.g. incorrect Equations of State, erroneous mis-use of Voigt, Reuss isothermal or adiabatic bulk moduli) has often in the past lead to inaccurate unreliable or even completely wrong results (e.g. negative thermal expansion, erroneous $\partial K/\partial T$ etc…) specially when the Eos are subsequently extrapolated to high-P,T.

Pressure-volume EoS are well-developed and, if correctly used, are capable of reproducing the isothermal volume or density changes of materials to within the experimental uncertainties. Previous versions of the EoSFit program were able to fit isothermal EoS, thermal expansion models and the thermal-pressure (Holland and Powell, 2011) to *P-V*, *V-T* or *P-V-T* data, by the method of least-squares. We have now extended the capabilities of EosFit-7c to also fit all of these forms of EoS to bulk and linear moduli, either alone or in combination with volume or unit-cell parameter data. With this approach we can now provide a reliable description of the variation of K' with T thus avoiding mistaken extrapolations leading to non-physical behaviour as often occurs for several materials (Helffrich and Connolly, 2009).

The consistency of the results obtained with this new fitting procedure has been shown by comparison of results from using adiabatic and isothermal moduli. It has also been demonstrated the importance of performing fitting with this procedure in terms of both accuracy and precision of the thermoelastic coefficients when the PT cross-terms ($\partial K/\partial T$ or $\partial \alpha/\partial P$) are extrapolated in PT space (see Fig. 5b). Additionally, thermodynamic functions were calculated for grossular using DFT approach within QHA. The obtained results are in fairly good agreement with experiment, when allowing for the known short-comings of the functionals employed in the DFT.

Acknowledgment

This work has been supported by the ERC Starting Grant (n° 307322) to F. Nestola. MA has been supported by the SIR-MIUR grant MILE DEEp (n° RBSI140351) to M. Alvaro. MD acknowledges computational grant G62-24 at Interdisciplinary Centre for Mathematical and Computational Modelling (ICM) of the University of Warsaw. RM and KSS acknowledge support through grant BE532003 of the University of Vienna. We thank Tom Duffy (Princeton) for advice and discussions.

References

Alvaro, M., Angel, R.J., Marciano, C., Milani, S., Scandolo, L., Mazzucchelli, M.L., Zaffiro, G., Rustioni, G., Briccola, M., Domeneghetti, M.C., and others (2015) A new micro-furnace for in situ high-temperature single-crystal X-ray diffraction measurements. Journal of Applied Crystallography, 48, 1192–1200.

Anderson, D.L. (1995) Equations of State of Solids for Geophysics and Ceramic Science. Oxford University Press. Oxford, UK.

Anderson, O.L. (1996) Anharmonicity of forsterite and the thermal pressure of insulators. Geophysical Research Letters, 23, 3031–3034.

Angel, R.J. (2000) Equations of state. In R.M. Hazen and R.T. Downs, Eds., Reviews in Mineralogy: High temperature and high pressure crystal chemistry. Mineralogical Society of America, Washington, D.C.

Angel, R.J., and Finger, L.W. (2011) SINGLE: a program to control single-crystal diffractometers. Journal of Applied Crystallography, 44, 247–251.

Angel, R.J., Allan, D.R., Milletich, R., and Finger, L.W. (1997) The use of quartz as an internal pressure standard in high-pressure crystallography. Journal of Applied Crystallography, 30, 461–466.

Angel, R.J., Bujak, M., Zhao, J., Gatta, G.D., and Jacobsen, S.D. (2007) Effective hydrostatic limits of pressure media for high-pressure crystallographic studies. Journal of Applied Crystallography, 40, 26–32.

Angel, R.J., Jackson, J.M., Reichmann, H.J., and Speziale, S. (2009) Elasticity measurements on minerals: a review. European Journal of Mineralogy, 21, 525–550.

Angel, R.J., Gonzalez-Platas, J., and Alvaro, M. (2014) EosFit7c and a Fortran module (library) for equation of state calculations. Zeitschrift fur Kristallographie, 229, 405–419.

Angel, R.J., Nimis, P., Mazzucchelli, M.L., Alvaro, M., and Nestola, F. (2015a) How large are departures from lithostatic pressure? Constraints from host-inclusion elasticity. Journal of Metamorphic Geology, 33, 801–813.

Angel, R.J., Nimis, P., Mazzucchelli, M.L., Alvaro, M., and Nestola, F. (2015b) How large are departures from lithostatic pressure? Constraints from host–inclusion elasticity. Journal of Metamorphic Geology, 33, 801–813.

Ashley, K.T., Darling, R.S., Bodnar, R.J., and Law, R.D. (2015) Significance of “stretched” mineral inclusions for reconstructing P–T exhumation history. Contributions to

Mineralogy and Petrology, 169, 1–9.

Baroni, S., De Gironcoli, S., Dal Corso, A., and Giannozzi, P. (2001) Phonons and related crystal properties from density-functional perturbation theory. Reviews of Modern Physics, 73, 515–562.

Blöchl, P.E. (1994) Projector augmented-wave method. Physical Review B, 50, 17953–17979.

Boehler, R. (1982) Adiabats of quartz, coesite, olivine, and magnesium oxide to 50 kbar and 1000 K, and the adiabatic gradient in the Earth's mantle. Journal of Geophysical Research: Solid Earth, 87, 5501–5506.

Boehler, R., and Ramakrishnan, J. (1980) Experimental results on the pressure dependence of the Gruneisen parameter: a review. Journal of Geophysical Research, 85, 6996–7002.

Bosenick, A., and Geiger, C.A. (1997) Powder X ray diffraction study of synthetic pyrope-grossular garnets between 20 and 295 K. Journal of Geophysical Research-All Series, 102, 22.

Bosenick, A., Geiger, C.A., and Cemič, L. (1996) Heat capacity measurements of synthetic pyrope-grossular garnets between 320 and 1000 K by differential scanning calorimetry. Geochimica et Cosmochimica Acta, 60, 3215–3227.

Du, W., Clark, S.M., and Walker, D. (2015) Thermo-compression of pyrope-grossular garnet solid solutions: Non-linear compositional dependence. American Mineralogist, 100, 215–222.

Erba, A., Mahmoud, A., Orlando, R., and Dovesi, R. (2014) Elastic properties of six silicate garnet end members from accurate ab initio simulations. Physics and Chemistry of Minerals, 41, 151–160.

Fei, Y. (1995) Thermal Expansion. In Mineral Physics & Crystallography: A Handbook of Physical Constants pp. 29–44. American Geophysical Union.

Freund, J., and Ingalls, R. (1989) Inverted isothermal equations of state and determination of B0, B'0 and B0. Journal of Physics and Chemistry of Solids, 50, 263–268.

Gwanmesia, G.D., Wang, L., Heady, A., and Liebermann, R.C. (2014) Elasticity and sound velocities of polycrystalline grossular garnet (Ca3Al2Si3O12) at simultaneous high pressures and high temperatures. Physics of the Earth and Planetary Interiors, 228, 80–87.

Helffrich, G., and Connolly, J.A.D. (2009) Physical contradictions and remedies using simple polythermal equations of state. American Mineralogist, 94, 1616–1619.

Holland, T.J.B., and Powell, R. (2011) An improved and extended internally consistent

thermodynamic dataset for phases of petrological interest, involving a new equation of state for solids. Journal of Metamorphic Geology, 29, 333–383.

Isaak, D.G., Anderson, O.L., and Oda, H. (1992) High-temperature thermal expansion and elasticity of calcium-rich garnets. Physics and Chemistry of Minerals, 19, 106–120.

Kawai, K., and Tsuchiya, T. (2012) First principles investigations on the elasticity and phase stability of grossular garnet. Journal of Geophysical Research: Solid Earth, 117, 1–8.

King, H.E., and Finger, L.W. (1979) Diffracted Beam Crystal Centering and Its Application to High-Pressure Crystallography. Journal of Applied Crystallography, 12, 374–378.

Klotz, S., Chervin, J.C., Munsch, P., and Marchand, G. Le (2009) Hydrostatic limits of 11 pressure transmitting media. Journal of Physics D: Applied Physics, 42, 75413.

Kono, Y., Gréaux, S., Higo, Y., Ohfuji, H., and Irifune, T. (2010) Pressure and temperature dependences of elastic properties of grossular garnet up to 17 GPa and 1 650 K. Journal of Earth Science, 21, 782–791.

Kresse, G., and Furthmüller, J. (1996) Efficient iterative schemes for ab initio total-energy calculations using a plane-wave basis set. Physical Review B, 54, 11169–11186.

Kroll, H., Kirfel, A., Heinemann, R., and Barbier, B. (2012) Volume thermal expansion and related thermophysical parameters in the Mg, Fe olivine solid-solution series. European Journal of Mineralogy, 24, 935–956.

Milani, S., Nestola, F., Alvaro, M., Pasqual, D., Mazzucchelli, M.L., Domeneghetti, M.C., and Geiger, C.A. (2015) Diamond-garnet geobarometry: The role of garnet compressibility and expansivity. Lithos, 227, 140–147.

Miletich, R., Allan, D.R., and Kuhs, W.F. (2000) High-pressure single-crystal techniques. High-Temperature and High-Pressure Crystal Chemistry, 41, 445–519.

Nye, J.F. (1985) Physical Properties of Cristals: Their Representation by Tensors and Matrices. Oxford University Press.

Orear, J. (1982) Least squares when both variables have uncertainties. American Journal of Physics, 50, 912.

Parlinski, K., Li, Z., and Kawazoe, Y. (1997) First-Principles Determination of the Soft Mode in Cubic ZrO2. Physical Review Letters, 78, 4063–4066.

Perdew, J., Ruzsinszky, A., Csonka, G., Vydrov, O., Scuseria, G., Constantin, L., Zhou, X., and Burke, K. (2008) Restoring the Density-Gradient Expansion for Exchange in Solids and Surfaces. Physical Review Letters, 100, 136406.

Perdew, J.P., Burke, K., and Ernzerhof, M. (1996) Generalized Gradient Approximation Made

Simple. Physical Review Letters, 77, 3865–3868.

Prencipe, M., Noel, Y., Bruno, M., and Dovesi, R. (2009) The vibrational spectrum of lizardite-1T [Mg3Si 2O5(OH)4] at the Γ point: A contribution from an ab initio periodic B3LYP calculation. American Mineralogist, 94, 986–994.

Prencipe, M., Scanavino, I., Nestola, F., Merlini, M., Civalleri, B., Bruno, M., and Dovesi, R. (2011) High-pressure thermo-elastic properties of beryl (Al4Be6Si12O36) from ab initio calculations, and observations about the source of thermal expansion. Physics and Chemistry of Minerals, 38, 223–239.

Prencipe, M., Mantovani, L., Tribaudino, M., Bersani, D., and Lottici, P.P. (2012) The Raman spectrum of diopside: a comparison between ab initio calculated and experimentally measured frequencies. European Journal of Mineralogy, 24, 457–464.

Prencipe, M., Bruno, M., Nestola, F., De La Pierre, M., and Nimis, P. (2014) Toward an accurate ab initio estimation of compressibility and thermal expansion of diamond in the [0, 3000 K] temperature and [0, 30 GPa] pressures ranges, at the hybrid HF/DFT theoretical level. American Mineralogist, 99, 1147–1154.

Ralph, R.L., and Finger, L.W. (1982) A Computer-Program for Refinement of Crystal Orientation Matrix and Lattice-Constants from Diffractometer Data with Lattice Symmetry Constraints. Journal of Applied Crystallography, 15, 537–539.

Salje, E.K.H., Wruck, B., and Thomas, H. (1991) Order-parameter saturation and low-temperature extension of Landau theory. Zeitschrift für Physik B Condensed Matter, 82, 399–404.

Skinner, B.J. (1956) Physical properties of end-members of the garnet group. American Mineralogist, 41, 428–436.

Thieblot, L., Roux, J., and Richet, P. (1998) High-temperature thermal expansion and decomposition of garnets. European Journal of Mineralogy, 10, 7.

Togo, A., and Tanaka, I. (2015) First principles phonon calculations in materials science. Scripta Materialia, 108, 1–5.

5. Thermal expansion of natural almandine garnet under controlled oxygen fugacity conditions

Scandolo L.[1], Milani S.[2,a], Di Prima M.[1], McCammon C.[3], Heidelbach F.[3], Nestola F.[2], Domeneghetti M.C.[1], Alvaro M.[1]

[1]Dept. Of Earth and Environmental Sciences, University of Pavia, Italy
[2]Dept. Of Geosciences, University of Padua, Italy
[3]Bayerisches Geoinstitut, Bayreuth, Germany
[a]Current affiliation Dept. of Earth Sciences, University of Bristol, United Kingdom

Corresponding author e-mail: **lorenzo.scandolo01@universitadipavia.it**
For submission to: **American Mineralogist**
Article type: **Article**
Running Title: **iron oxidation and thermal expansion of almandine**

ABSTRACT

As oxygen fugacity (fO_2) changes with temperature it is fundamental to understand its possible influence on lattice parameters expansion. Therefore, in order to evaluate any possible role of iron oxidation on the thermal expansion behavior, two Fe-rich almandine ($Alm_{94}Py_4Gr_1Sp_1$) natural crystals from a single rock sample have been investigated at high-temperature *in situ* by means of single-crystal X-ray diffraction under different fO_2 conditions. The first crystal has been heated in a vial prepared under vacuum (3×10^{-2}mbar) whereas the second one has been held into an identically vacuumed vial together with an iron-wustite buffer to control the fO_2 conditions. The lattice parameters changes for both crystals have been determined in a range of T between 298K and 1100K.

The oxidation state of the two garnets recovered after the high-T experiments has been evaluated using single-crystal Mössbauer spectroscopy. For purpose of comparison the Fe^{2+}/Fe^{3+} has been determined also on one untreated (not annealed) crystal from the same hand sample. The thermal expansion data obtained using a Fei-EoS for the two experiments on the two crystals are in good agreement with one another being respectively $2.4(2)\times10^{-5}$ (K^{-1}) for the vacuum sample and $2.0(3)\times10^{-5}$ (K^{-1}) for iron-wustite sample.

Furthermore, Mössbauer data, $Fe^{3+}/\Sigma Fe = 0.04 \pm 0.02$ and 0.01 ± 0.01 for the crystal heated under vacuum and with iron-wustite buffer respectively, indicate that no oxidation occurs for none of the two Fe-rich garnets samples at least for temperature lower than 1100 K and annealing times not greater than two weeks.

This evidence seems to point out that there is no evident effect of the different fO_2 conditions on the lattice parameters evolution as a function of temperature at least for a stiff structure such as almandine in a range of temperature that does not exceed 1100 K.

Keywords: iron oxidation; almandine; thermal expansion; high-temperature; single crystal X-ray diffraction

INTRODUCTION

The study of mineral inclusions still trapped in other mineral phases provides information about the Earth's interior and its active geodynamics (Stachel et al., 2005; Shirey et al., 2004; Kopylova et al., 2010). Determination of the pressures at which mineral inclusions were entrapped is hence fundamental for constraining the chemico-physical environment in which they formed. An alternative method to conventional chemical geothermobarometry is based on the residual pressure (P_{inc}) on the inclusion still trapped in the host at room temperature and pressure as recently developed by Angel et al. 2015a; Angel et al. 2014b; Angel et al. 2015b. This method can be potentially applied to any single mineral inclusion trapped inside a host mineral such as for instance garnets in diamond, coesite and quartz in diamond and/or garnet; olivine in diamond (see Angel et al., 2015a). For the application of the elastic geobarometry, knowledge of the thermoelastic properties for both host and inclusion are a fundamental pre-requisite (Angel et al., 2014b). Among garnets naturally occurring in the Earth's crust and upper mantle (Duffy and Anderson, 1989) and those retrieved as inclusions entrapped in diamonds (Stachel and Harris, 2008), almandine (the iron-rich end-member of aluminum silicate garnets), and pyrope (the Mg-rich member) represent the most abundant phases. However, because of the broad chemical variability within the solid solution, for aluminosilicate garnets investigating the dependence of the thermoelastic properties upon composition is extremely challenging. Recently, an application of elastic geobarometry for garnets inclusion entrapped in diamonds has been published by Milani et al. 2015. The authors clearly showed that the elastic properties of pyrope and almandine members alone have the strongest control on the resulting elastic behavior of the common eclogitic and peridotitic garnet compositions. However, while the thermoelastic properties of diamond are well known (Angel et al., 2015a) the few available thermal expansion data on almandine, did not allow Milani et al. (2015) to perform a complete evaluation of the behavior for the diamond-almandine pair as a function of pressure and temperature. Furthermore, because of the lack of data evaluating the role of oxygen fugacity (fO_2) on the lattice parameters with temperature, an accurate determination of the thermal expansion coefficients for Fe-rich aluminosilicate garnets (e.g. almandine) is even more difficult and requires knowledge of the effect of Fe oxidation state on the lattice thermal expansion.

The pioneer work of Levy et al 2004 firstly highlighted the dependence of the lattice parameters thermal expansion (α) on oxygen fugacity (fO_2) conditions at least for the case of magnetite. In their work Levy et al 2004 determined the lattice thermal expansion on magnetite

performing two X-ray powder diffraction experiments at different vacuum conditions (P=10-4 mbar and P=10-6 mbar) concluding that the Fe oxidation increases the expansion rate almost doubling the α(T) values in the oxidized samples. However, the complexity of the oxidation reaction for almandine that involves Fe^{3+} substitution for Al in the six-fold coordination accompanied by decomposition (Malaspina et al., 2009 JPet, 2010) is thermodynamically much less favorable than that of magnetite or other oxides (Woodland et al.,1999). Despite some high and low temperature experiments that have been already performed on almandine (e.g. (Lager, 1992; Skinner, 1956; Thieblot et al., 1998) the effect of iron oxidation (Fe^{2+} vs Fe^{3+}) on the lattice parameters behavior it still not clear.

Therefore, the aim of this study is to ascertain the role of oxygen fugacity (fO_2) on the thermal expansion behavior of almandine by combining single crystal X-ray diffraction experiments at high-temperature (conducted at different fO_2) with Mössbauer spectroscopy.

EXPERIMENTAL

Samples

Single crystals of the natural garnets from Monte Cistella, Verbania, Italy have been chosen by SCXRD because of the very good agreement of their unit cell parameters with those obtained for a synthetic pure composition almandine end member (i.e. $Fe_3Al_2Si_3O_{12}$). For the high-temperature study two single crystals of almandine (ca. 100-150 μm radius) have been selected based on the absence of twinning and visible inclusions and on the quality of their diffraction peak profiles (FWHM typically smaller than 0.1°). The two single crystals have been mounted separately in two different polycrystalline quartz vials (0.3 mm inner diameter) closed at the top with an oxy-methane flame and held in place with quartz wool in order to avoid mechanical stresses. One vial was kept open at the bottom in order to allow exchanges between the crystal and the external environment while performing the high-temperature experiment. The second vial was prepared with an "iron-wüstite" powder as buffer added together with the crystal as showed in Fig.1. The vial containing crystal and buffer was further washed with argon and vacuumed down to about 2.5×10^{-2} mbar and then sealed at the bottom with oxy-methane flame.

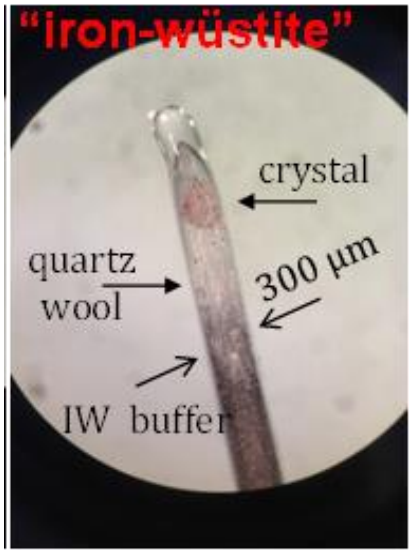

Fig. 1 Sample preparation for the iron-wustite buffered sample. The sample is located at the top of the vial, held in place by quartz wool. The IW buffer has been added in the vial right below the sample (no in contact with the crystal). The vial containing the sample and buffer has been subsequently vacuumed with a rotary pump to 3×10^{-2} mbar and then sealed at the bottom with oxy-methane flame.

X-ray diffraction at high temperature

The high-temperature single-crystal X-ray diffraction experiments were performed at the University of Pavia with a HUBER four-circle point detector diffractometer operating at 40 kV and 30 mA (Mo$K\alpha$ radiation) and equipped with a 0.8 mm short collimator automated with SINGLE software (Angel and Finger, 2011). The high temperature experiments were performed using a newly designed micro-furnace (see Alvaro et al., 2015 for further details and Fig. 4.1) controlled by a Eurotherm temperature regulator.

During the high temperature experiments the effects of the crystal offsets and the diffractometer aberrations were removed by using the eight-position centering method (King and Finger, 1979) before starting the high-temperature measurements. For the two samples the unit-cell parameters (Table 1 and 2) have been determined upon heating and cooling from room-T up to 1113 and 1088 K respectively and using not less than 25 reflections measured with the eight-positions method (King and Finger, 1979). Unconstrained unit-cell parameters confirmed the cubic symmetry within 1 e.s.d. therefore only constrained unit-cell parameters obtained by vector least-squares fit (Ralph and Finger, 1982) are reported in Table 1-2.

Table 1. Unit-cell parameters of natural almandine at different temperature, vial sealed with vacuum

T (°C)	*a* (Å)	V (Å^3)
28	11.5301(6)	1532.85(25)
55	11.5323(6)	1533.72(24)
122	11.5379(6)	1535.97(24)
188	11.5440(6)	1538.41(24)
252	11.5496(6)	1540.66(24)
315	11.5556(6)	1543.04(24)
376	11.5613(6)	1545.31(24)
438	11.5671(6)	1547.67(24)
496	11.5726(6)	1549.87(24)
555	11.5782(6)	1552.12(24)
612	11.5835(6)	1554.24(24)
667	11.5887(6)	1556.36(24)
724	11.5943(7)	1558.59(29)
777	11.5995(6)	1560.68(25)
832	11.6047(6)	1562.79(25)
884	11.6097(6)	1564.83(26)
858	11.6072(6)	1563.82(26)
750	11.5964(7)	1559.45(27)
640	11.5854(6)	1555.00(26)
525	11.5745(6)	1550.62(23)
406	11.5631(6)	1546.05(25)
283	11.5515(6)	1541.41(26)
155	11.5402(6)	1536.87(25)
55	11.5312(6)	1533.28(26)

Note: standard deviations are given in parenthesis

Table 2. Unit-cell parameters of natural almandine at different temperature, vial prepared with IW buffer

T(°C)	*a* (Å)	V (Å^3)
28	11.5293(4)	1532.51(16)
55	11.5315(4)	1533.39(16)
122	11.5378(4)	1535.93(16)
188	11.5440(4)	1538.41(14)
252	11.5499(4)	1540.77(15)
315	11.5558(4)	1543.10(16)
376	11.5616(4)	1545.45(15)
438	11.5674(4)	1547.75(15)
496	11.5729(4)	1549.98(15)
555	11.5785(4)	1552.22(15)
612	11.5839(4)	1554.40(15)
667	11.5892(4)	1556.54(14)
724	11.5946(4)	1558.73(15)
777	11.5997(4)	1560.78(15)
832	11.6047(4)	1562.81(15)
884	11.6098(4)	1564.83(15)
858	11.6074(4)	1563.88(15)
750	11.5971(5)	1559.74(19)
640	11.5861(4)	1555.30(17)
525	11.5754(4)	1550.99(16)
406	11.5641(4)	1546.45(15)
283	11.5525(4)	1541.80(17)
155	11.5409(4)	1537.15(16)
88	11.5345(4)	1534.59(16)

Note: standard deviations are given in parenthesis

Mössbauer spectroscopy

In order to evaluate the oxidation state (i.e. Fe^{2+}- Fe^{3+} ratios) the two single-crystals recovered after the annealing have been investigated by means of Mössbauer spectroscopy at BGI- Bayerisches Geoinsitut. For purpose of comparison one natural (never heated) crystal from the same fragment has been also analyzed in order to provide the initial oxidation state. While determination of Fe^{3+} concentration from relative areas is straightforward in polycrystalline samples because the areas of component doublets can be assumed to be equal, it is more challenging for single crystals because the component doublet areas are orientation dependent. Therefore, Mössbauer spectra of the crystals at two different orientations were recorded and fitted simultaneously with the hyperfine parameters of each subspectrum (center shift, quadrupole splitting, line width) constrained to be equal between different orientations. Each was mounted between plastic sheets and covered with a piece of 25 μm thick Ta foil (absorbs 99% of 14.4 keV gamma rays) drilled with a 400 μm diameter hole. Images of the grains are shown in Fig 2. Mössbauer spectra were recorded at room temperature (293 K) in transmission mode on a constant acceleration Mössbauer spectrometer with a nominal 370 MBq 57Co high specific activity source in a 12 μm thick Rh matrix. The velocity scale was calibrated relative to 25 μm thick α-Fe foil using the positions certified for (former) National Bureau of Standards standard reference material no. 1541; line widths of 0.36 mm/s for the outer lines of α-Fe were obtained at room temperature. Each Mössbauer spectrum was collected for between 2 and 11 days and all spectra were fitted using the program MossA (Prescher et al., 2012).

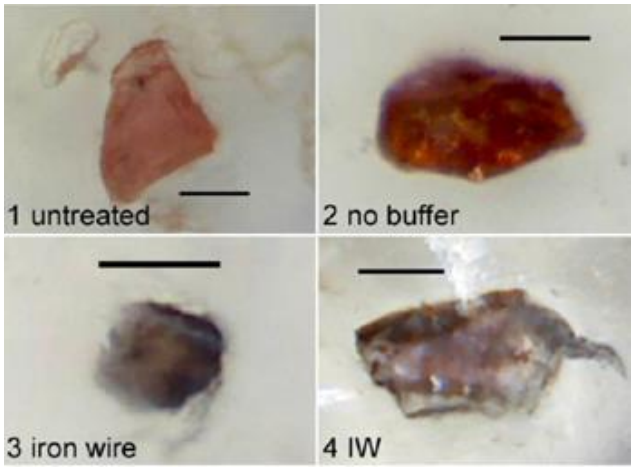

Fig. 2 Single crystals used for the high temperature experiments (2, 3, 4) and the untreated crystal (1). All the samples have been analyzed by Mössbauer spectroscopy to determine the Fe^{3+}/Fe_{tot} content.

RESULTS AND DISCUSSION

Room temperature X-ray diffraction

The unit-cell volume determined on our two samples are 1532.8(3) and 1532.5(2) $Å^3$ for the vacuumed and the iron-wustite samples respectively (see Table 1 and Table 2). Thieblot et al. (1998) reported a unit-cell volume for the natural almandine of 1533.8(4) $Å^3$ at 27°C , while Skinner (1956) described a synthetic sample not characterized with a unit-cell volume of 1531.1(5) $Å^3$ at 21°C. Geiger et al. (1988) gave a best estimate for the unit-cell volume of end-member almandine of 1530.81 $Å^3$ that can increase for the presence of Fe^{3+} in the octahedral site structural OH^- ("hydro-garnet substitution"), even if in literature different values, mainly due to the difficulty to crystallize pure end-members, are reported. Ottonello et al. (1996) reported a range for the unit-cell parameters at room temperature between 11.521 and 11.529 Å which correspond to a unit-cell volume ranging from 1529.2 to 1532.4 $Å^3$. The discrepancy in unit-cell volume of about 1.7$Å^3$ with respect to the values reported by Geiger et al., (1988), might be ascribed to a small difference in composition whereas those with respect to Ottonello et al., (1996) lie in less than 1-2 sigmas. Our unit-cell volume appears to be slighlty higher compared to those reported at room temperature [1530.8(4) $Å^3$] by Armbruster et al. (1992) whereas are in very good agreement with the those by Galkin et al. (2015) [1531.9(2) $Å^3$]. The comparison with the other room temperature unit cell volume is reported in Fig.3

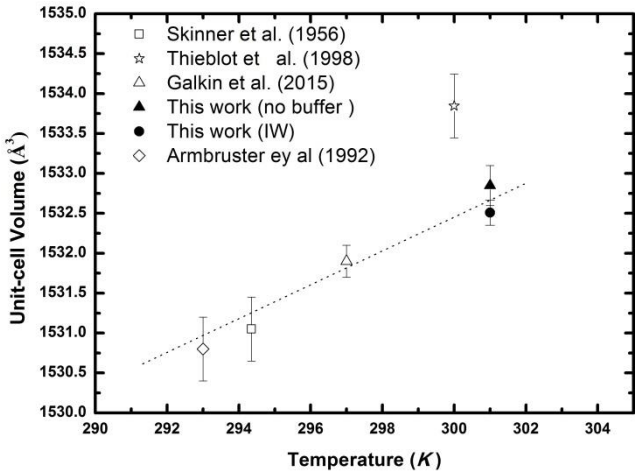

Fig 3. Room-T unit-cell volumes of almandine for all the literature study here considered (Skinner et al., 1986, Armbruster et al., 1992, Thieblot et al., 1998, Galkin et al., 2015). The slightly different temperatures reported could results from the slightly different reference temperature calibration used in the various data collections. Dashed line represents the linear correlation between unit cell volume and reference temperature. Data by Thieblot et al (1998) do not fall within the trend line because of the significantly different composition of their sample (see the text for further details).

Thermal expansion for almandine

The unit-cell parameters for the two almandine samples determined at different fO_2 conditions and different temperature are reported in Table 1 and 2. The unit-cell volume for both samples increase smoothly (about 2%) with increasing temperature up to the maximum temperature reached (i.e. 1110 K), showing no sign of deviation from linearity. The measurements performed upon heating and cooling for both samples vacuumed and with the iron wustite buffer agree one to another within 1 standard deviation thus confirming that no irreversible change occurred in the crystal and indicating good experimental reproducibility. A comparison of calculated unit-cell volumes, using the fitted coefficients, and the experimentally measured unit-cell volumes in the high temperature regime (see Pandolfo et al., 2015 for a discussion of δV and statistical parameters from the fitting] confirms that the model equation provides a good fit over the whole temperature range (below 1 e.s.d for whole experimental data).

For purpose of comparison with the literature the lattice parameters determined from both experiments have been reported in Fig. 4. Fit of the lattice parameters to the entire range of temperature have been performed using EosFit7c software (Angel et al. 2014a) with a Fei-type EoS (Fei 1995) yielding the following thermal expansion coefficients: 2.4(2) and 2.0(3) (full elastic coefficients, α_0, α_1 and α_2 are reported in Table 3). As our two dataset agree to better than one e.s.d.'s we combined them into a single dataset. From the weighted fitting of the new unique dataset we obtained a thermal expansion coefficient [2.26(17) $10^{-5}K^{-1}$] that, as expected, falls in between those obtained on the two datasets separately.

This value is in very good agreement (better than 2 e.s.d.'s) with the data from Skinner (1956); Galkin et al. (2015); Armbruster et al. (1992) as expected from the overlap between the unit-cell volume for the entire range of T (see Fig. 4).

On the contrary larger discrepancies have been found between our data and those of Thieblot et al. (1998) which could be ascribed to difference in the experimental technique (i.e. powder diffraction vs. single-crystal diffraction) and composition. The natural almandine used by Thieblot et al., (1998) does contain some Ca and Mn (see Alm83%Py11%Sp3%Gr2%And1% Table 1 in Thieblot et al., 1998). Regardless the composition of the sample used by Thieblot et al. (1998) fitting of their data using Fei-EoS, even excluding the two measurements above 1300 K (temperature at which the sample has already undergone decomposition), lead to an unphysical behavior of the thermal expansion coefficient that decreases with increasing temperature. Our thermal expansion coefficients significantly exceed those reported by Skinner

(1956) (see Table 3). However, the composition for the almandine garnet investigated by Skinner (1956) was not determined.

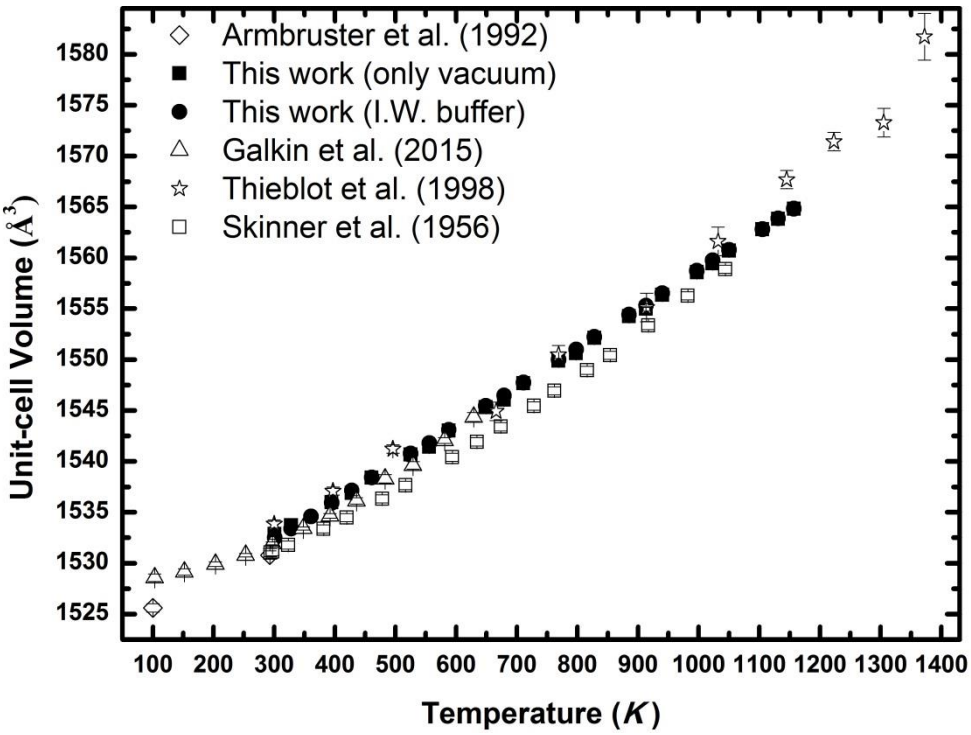

Fig. 4 High temperature unit cell volume for our two experiments on almandine together with all the available literature datasets (Skinner et al., 1986, Armbruster et al., 1992, Thieblot et al., 1998, Galkin et al., 2015).

Table 3. Volume of almandine at 303 K and 1073 K and thermal expansion behavior given by Fei-type and Kroll-type EoS.

$V_{298\ K}$ calculated ($Å^3$)	$V_{1073\ K}$ calculated ($Å^3$)	$\alpha_{298\ K}$ x10^{-5} (K^{-1})	α_0 x10^5 (K^{-1})	α_1 x10^8 (K^{-2})	α_2	EoS formalism	Reference
1532.35(12)	1561.6(2.5)	**2.4(2)**	2.4(2)	0.04(19)	-0.1(2)	Fei-type[3]	IW this work
1532.7(2)	1651.5(4.1)	**2.0(3)**	2.5(3)	0.0(3)	-0.5(4)		no buffer this work
1532.63(9)	1561.6(2.1)	**2.26(17)**	2.46(17)	0.04(16)	-0.2(2)		This work (both)
1531.3(2)	1560.3(9.1)	**1.6(7)**	1.9(8)	1.0(8)	-0.6(8)		Skinner (1956)[1]
1533.9(4)	1563(15)	**3.2(1.2)**	-0.5(12)	3.3(1.2)	2.2(1.3)		Thieblot et al. (1998)[2]
		1.965				Empirical calculations	Saxena et al. (1993)
		1.9					Ottonello et al. (1996)
V_{298K}	V_{0K}	$\alpha_{298\ K}$ x10^{-5} (K^{-1})	p1 (0 K)	T_{sat} (0 K)			
1531.9(5)	1528.8(3)	**1.78(5)**	10.6(9)	347(37)		Salje-type	Galkin (2015)
1531.0(9)	1525.4(5)	**2.45(9)**	11.5(1.3)	232(53)			Geiger (1992)
Data set measurement are below refinements parameters and can't be fitted into a EoS							Chaplot (2002)
1539.2(2)		**3.1(7)**				PVT data set	Fan (2009)
normalizing data set in order to avoid slight difference in the V0 and difference attributed to sample preparation and temperature calibration							
		$\alpha_{298\ K}$ x10^{-5} (K^{-1})	K'	T_E			
1.00014(6)	1.0189(1)	**1.768(9)**	5.8(5)	614		Kroll-type(Galking 2015 for LT)	no buffer this work
1.00033(7)	1.0192(1)	**1.865(10)**	5.8(5)	550			IW this work
1.00030(6)	1.0191(1)	**1.859(8)**	5.8(5)	550			This work (both)
1.00001(7)		**1.76(2)**	5.8(5)	614			Skinner (1956)[1]
1.00000(9)		**2.103(14)**	5.8(5)	340		Kroll-type(Geiger 1992 for LT)	no buffer this work
1.00027(6)		**2.113(9)**	5.8(5)	340			IW this work
1.00013(5)		**2.111(8)**	5.8(5)	340			This work (both)
1		**2.08(3)**	5.8(5)	360			Skinner (1956)[1]

Note: [3]Fei-type coefficients reported are calculated using as T_{ref} the first experimental temperature collected for each dataset.

Fe^{2+}/Fe^{3+} ratios from Mossbauer spectroscopy

Mössbauer experiments were performed for the two crystals recovered after the heating experiment, together with an untreated (i.e. never annealed) crystal to be used for assessing the initial oxidation state (Fig. 2). For what concerns the untreated crystal, the Mössbauer spectrum is dominated by a Fe^{2+} doublet with a slight asymmetry as expected due to the Gol'danskii–Karyagin effect (see Bull et al., 2012 and references therein). If the spectrum is fit to a single quadrupole doublet with unequal component areas, there is a slight deviation of the residual around 0.5 mm/s. This is likely due to Fe^{3+}, therefore a second quadrupole doublet was added. Conventional constraints were applied during the fitting (equal component areas and widths for the Fe^{3+} doublet and equal component widths for the Fe^{2+} doublet) and the final fit accounted for all absorption (Fig. 5). The hyperfine parameters of both Fe^{2+} and Fe^{3+} are consistent with literature values (Amthauer et al., 1976).

The Mössbauer spectrum for the crystal heated without buffering system, is similar to the one for the previous sample (i.e. untreated), but the absorption around 0.5 mm/s is less well defined. To obtain a realistic estimate of Fe^{3+}, the hyperfine parameters (centre shift, quadrupole splitting and full width at half maximum) of the Fe^{3+} doublet were constrained to the values obtained for the first crystal. The fitting model accounts for all absorption within the data scatter.

Lastly, the Mössbauer spectrum for the crystal heated using the "iron-wüstite" buffer was collected over a much longer period (11 days) to improve statistics. There is no deviation in the residual when a single quadrupole doublet is fitted to the spectrum, and addition of a second doublet corresponding to Fe^{3+} with hyperfine parameters fixed to the values from the first crystal, does not yield an intensity greater than the detection limit.

In summary, the amount of Fe^{3+} in the untreated and heated ("no buffer") crystals appears to be small but measurable based on (i) the higher χ^2 values when only Fe^{2+} is fit to the spectrum, and (ii) the visible deviation in the residual when only Fe^{2+} is fit to the spectrum. In contrast, the amount of Fe^{3+} in the heated (I.W.) crystal appears to be at or lower than the detection limit (0.01) (see results in Table 4).

Table 4. Summary of results of Mössbauer measurements

sample	Fe3+/∑Fe	±
1 untreated	0.04	0.02
2 no buffer	0.02	0.01
3 I.W.	0.01	0.01

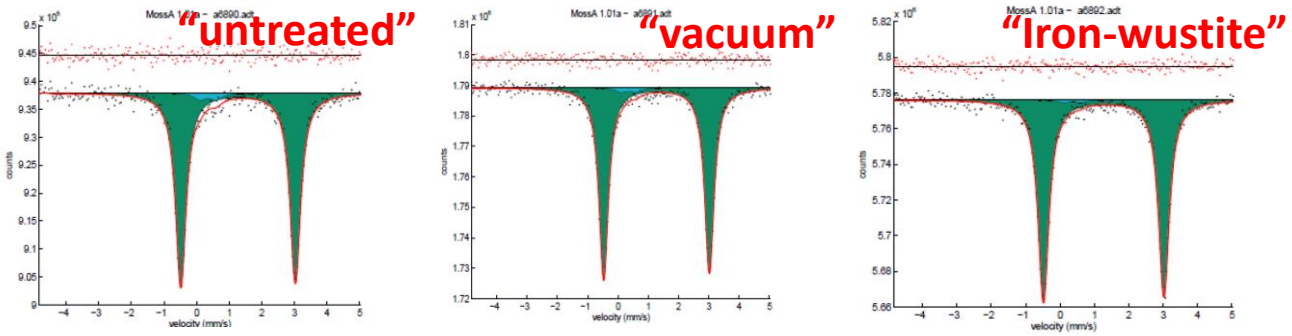

Fig. 5 Mossbauer spectra for the three analyzed crystals (see text for details) from the untreated one (left) to the iron-buffered (right). The absorption at 0.5 mm/s becomes less defined going from the untreated to the "iron-wustite" crystal. The very poor difference could be ascribed to small compositional variations of the starting samples together with the very low content of Fe^{3+}.

Single equation of state for almandine at different fO_2

As we have showed that the effect of fO_2 on the thermal expansion of almandine is negligible we can determine one single equation of state for our two almandine single crystals. For geobarometric purposes it has been demonstrated (Angel et al., 2015b) that thermal pressure-type EoS (or Kroll-type) gives more reliable results with respect to other equation of state formalisms as it avoids the needs to determine cross-terms (e.g. $\partial K/\partial T$). Thermal-pressure and/or Kroll-type EoS require high-T data to be fit together with those in the low T regime. However, the majority of the datasets available for the low-T behavior of almandine (e.g. Armbruster et al., 1992; Chaplot et al., 2002; Sumino et al., 1978) are focused on the study of the structural changes at low temperature. Therefore, in most of the literature work only few volume-temperature data are reported and thus cannot be used for fitting purposes (i.e. small ratio of data versus parameters to be refined). The only dataset with a relatively large number of temperature-volume data points is that by Galkin et al. (2015).

In order to minimize the discrepancies between the different datasets all the unit cell volume data have been normalized to their value at 298K (see Fig. 6). Normalized unit-cell volume data from Galkin et al. (2015) have combined with our dataset produced by merging the iron-wustite and the no buffer dataset. This unique dataset have been fit to a Kroll-type EoS using EoS-fit7 (Angel et al., 2014c). The K'=5.8(5) which is required for the Kroll-type EoS has been taken from Milani et al. (2013). The T_E obtained minimizing $\omega\chi^2$ is in good agreement with the values reported in literature (Babuska et al., 1978; Stixrude and Lightgow-Bertelloni, 2005; Galkin et al.2015).

The thermal expansion coefficient at room temperature [$\alpha_0=1.859(8)\times10^{-5}K^{-1}$] obtained with this method significantly improved the description of the thermal expansion of almandine in both

the low-T and high-T regimes with respect to the one obtained using a Fei-type approach (see Fig. 6).

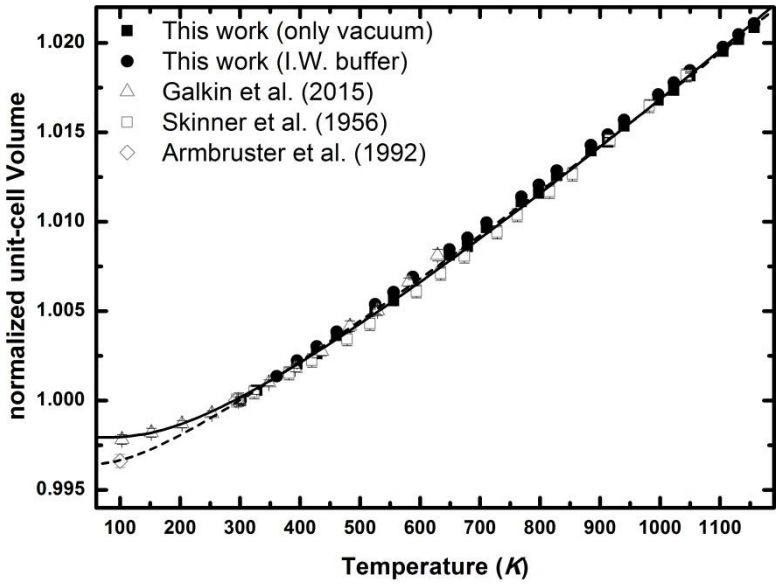

Fig. 6 Normalized unit-cell volume (V_0=1532.51(16) Å^3, this work). The two different curves represent the fitting results obtained on our merged dataset ("vacuum" sample plus IW buffer sample) together with the dataset at low temperature by Galkin et al., (2015) straight line and Armbruster et al. (1992), dotted line obtained using a Kroll EoS.

IMPLICATIONS

Oxygen is a highly reactive gas locked up permanently within the crystal structure, therefore maintains a degree of reactivity with its environment. A commonly used measure of this reactivity is the oxygen fugacity (fO_2). As clearly demonstrated in several manuscripts (Frost, 1991), oxygen fugacity strongly changes upon temperature variations, therefore it is crucial to understand the oxygen reactivity while performing experiments with iron bearing samples.

Many xenolith samples record oxygen fugacity close to the Fe-Ni precipitation curve that represent the fO_2 conditions at which Ni-rich Fe alloy will start to precipitate out of the mantle silicates as a consequence of reduction of the iron buffer (O'Neill and Wood, 1979). The curve has a fO_2 close to that of iron wüstite buffer (IW): $2Fe+O_2=2FeO$ which is considered an effective lower bound in the mantle fugacity (fO_2). This means that at pressure (i.e. depth) where diamond is stable in the cratonic lithosphere the surrounding environment is likely to have an fO_2 that is reducing enough so that carbon can exist as diamond (Stagno and Frost, 2010). Our results

clearly showed that no matter what the fO_2 conditions are, the thermal expansion of almandine does not change!

Therefore, we can consider our merged equation of state sufficiently reliable to be used for geobarometric estimate involving Fe-rich almandine garnets. The two nearly identical thermal expansion coefficients would lead to differences in the entrapment pressures calculated using elastic geobarometry methods (Nimis, 2002, Nimis and Taylor, 2000; Grütter et al., 2006; Simakov, 2006) of about 0.3GPa. Such difference, that correspond to about 10 km depth, is geologically negligible.

References

Alvaro, M., Angel, R.J., Marciano, C., Zaffiro, G., Scandolo, L., Mazzucchelli, M.L., Milani, S., Rustioni, G., Domeneghetti, M.C., and Nestola, F. (2015) Development of a new micro-furnace for. EGU General Assembly Conference Abstracts, 17, p. 12423.

Amthauer, G., Annerste, H., and Hafner, S. (1976) The Mössbauer spectrum of 57Fe in silicate garnets*. Zeitschrift für Kristallographie-Crystalline Materials, 143(JG), 14-55.

Angel, R., Alvaro, M., Nestola, F., and Mazzucchelli, M. (2015a) Diamond thermoelastic properties and implications for determining the pressure of formation of diamond-inclusion systems. Russian Geology and Geophysics, 56(1-2), 211-220.

Angel, R., Nimis, P., Mazzucchelli, M., Alvaro, M., and Nestola, F. (2015b) How large are departures from lithostatic pressure? Constraints from host–inclusion elasticity. Journal of Metamorphic Geology.

Angel, R.J., Mazzucchelli, M.L., Alvaro, M., Nimis, P., and Nestola, F. (2014b) Letter. Geobarometry from host-inclusion systems: The role of elastic relaxation.

Angel, R.J., Gonzalez-Platas, J., Alvaro, M., (2014)c. EosFit-7c and a Fortran module (library) for equation of state calculations. Zeit Kristall 229: 405-419.

Armbruster, T., Geiger, C., and Lager, G. (1992) Single crystal X-ray refinement of almandine-pyrope garnets at 298 and 100 K. American Mineralogist, 77, 512-523.

Babuška, V., Fiala, J., Kumazawa, M., Ohno, I., and Sumino, Y. (1978) Elastic properties of garnet solid-solution series. Physics of the Earth and Planetary Interiors, 16(2), 157-176.

Bull, J., Tennant, W., Ballaran, T.B., Nestola, F., and McCammon, C. (2012) Anisotropic mean-squared-displacement tensor in cubic almandine garnet: a single crystal 57 Fe Mössbauer study. Physics and Chemistry of Minerals, 1-15.

Chaplot, S., Mittal, R., Busetto, E., and Lausi, A. (2002) Thermal expansion in zircon and almandine: Synchrotron x-ray diffraction and lattice dynamical study. Physical Review B, 66(6), 064302.

Duffy, T.S., and Anderson, D.L. (1989) Seismic Velocities in Mantle Minerals and the Mineralogy of the Upper Mantle. J. Geophys. Res., 94(B2), 1895-1912.

Frost, B.R. (1991) Introduction to oxygen fugacity and its petrologic importance. Reviews in Mineralogy and Geochemistry, 25(1), 1-9.

Galkin, V., and Gartvich, Y. (2015) Thermal expansion and evaluation of almandine heat capacity. Journal of Thermal Analysis and Calorimetry, 122(3), 1239-1244.

Geiger, C., Langer, K., Winkler, B., and Cemic, L. (1988) The synthesis, characterization and physical properties of end-member garnets in the system (Fe, Mg, Ca, Mn) 3Al2 (SiO4) 3. High pressure geosciences and material synthesis, 193-198.

Geiger, C. (1999) Thermodynamics of (Fe^{2+}, Mn^{2+}, Mg, Ca) 3- $Al_2Si_3O_{12}$ garnet: a review and analysis. Mineralogy and Petrology, 66(4), 271-299.

Grütter, H., Latti, D., and Menzies, A. (2006) Cr-saturation arrays in concentrate garnet compositions from kimberlite and their use in mantle barometry. Journal of Petrology, 47(4), 801-820.

King, H.E., and Finger, L.W. (1979) Diffracted Beam Crystal Centering and Its Application to High-Pressure Crystallography. Journal of Applied Crystallography, 12(Aug), 374-378.

Kopylova M, Navon O, Dubrovinsky L, Khachatryan G (2010) Carbonatitic mineralogy of natural diamondforming fluids. Earth Planet Sci Lett 291:126-137.

Lager, G.A. (1992) Single-crystal X-ray structure study of synthetic pyrope almandine garnets at 100 and 293 K. American Mineralogist, 77, 512-521.

Levy, D., Artioli, G., and Dapiaggi, M. (2004) The effect of oxidation and reduction on thermal expansion of magnetite from 298 to 1173K at different vacuum conditions. Journal of Solid State Chemistry, 177(4), 1713-1716.

Malaspina, N., Poli, S., and Fumagalli, P. (2009) The oxidation state of metasomatized mantle wedge: insights from C–O–H-bearing garnet peridotite. Journal of Petrology, egp040.

Malaspina, N., Scambelluri, M., Poli, S., Van Roermund, H., and Langenhorst, F. (2010) The oxidation state of mantle wedge majoritic garnet websterites metasomatised by C-bearing subduction fluids. Earth and Planetary Science Letters, 298(3), 417-426.

Milani, S., Mazzucchelli, M., Nestola, F., Alvaro, M., Angel, R.J., Geiger, C.A., and Domeneghetti, C. (2013) The PT conditions of garnet inclusion formation in diamond:

thermal expansion of synthetic end-member pyrope. EGU General Assembly Conference Abstracts, 15, p. 13133.

Milani, S., Nestola, F., Alvaro, M., Pasqual, D., Mazzucchelli, M., Domeneghetti, M., and Geiger, C. (2015) Diamond–garnet geobarometry: The role of garnet compressibility and expansivity. Lithos, 227, 140-147.

Nimis P, Taylor WR (2000) Single clinopyroxene thermobarometry for garnet peridotites. Part I. Calibration and testing of a Cr-in-Cpx barometer and an enstatite-in-Cpx thermometer. Contrib Mineral Petrol 139: 541-554.

Nimis, P. (2002) The pressures and temperatures of formation of diamond based on thermobarometry of chromian diopside inclusions. The Canadian Mineralogist, 40(3), 871-884.

O'Neill, H.S.C., and Wood, B. (1979) An experimental study of Fe-Mg partitioning between garnet and olivine and its calibration as a geothermometer. Contributions to Mineralogy and Petrology, 70(1), 59-70.

Ottonello, G., Bokreta, M., and Sciuto, P. (1996) Parameterization of energy and interactions in garnets: End-member properties. American Mineralogist, 81(3-4), 429-447.

Pandolfo, F., Cámara, F., Domeneghetti, M.C., Alvaro, M., Nestola, F., Karato, S.-I., and Amulele, G. (2015) Volume thermal expansion along the jadeite–diopside join. Physics and Chemistry of Minerals, 42(1), 1-14.

Prescher, C., McCammon, C., and Dubrovinsky, L. (2012) MossA: a program for analyzing energy-domain Mössbauer spectra from conventional and synchrotron sources. Journal of Applied Crystallography, 45(2), 329-331.

Ralph, R.L., and Finger, L.W. (1982) A Computer-Program for Refinement of Crystal Orientation Matrix and Lattice-Constants from Diffractometer Data with Lattice Symmetry Constraints. Journal of Applied Crystallography, 15(Oct), 537-539.

Shirey, S.B., Richardson, S.H., Harris, J.W., (2004) Integrated models of diamond formation and craton evolution. Lithos 77, 923-944.

Simakov, S. (2006) Redox state of eclogites and peridotites from sub-cratonic upper mantle and a connection with diamond genesis. Contributions to Mineralogy and Petrology, 151(3), 282-296.

Skinner, B.J. (1956) Physical properties of end-members of the garnet group. American Mineralogist, 41, 428-436.

Stachel, T., and Harris, J. (2008) The origin of cratonic diamonds—constraints from mineral inclusions. Ore Geology Reviews, 34(1), 5-32.

Stagno, V., and Frost, D.J. (2010) Carbon speciation in the asthenosphere: Experimental measurements of the redox conditions at which carbonate-bearing melts coexist with graphite or diamond in peridotite assemblages. Earth and Planetary Science Letters, 300(1), 72-84.

Stixrude, L., and Lithgow-Bertelloni, C. (2005) Thermodynamics of mantle minerals—I. Physical properties. Geophysical Journal International, 162(2), 610-632.

Sumino, Y., and Nishizawa, O. (1978) Temperature variation of elastic constants of pyrope-almandine garnets. Journal of Physics of the Earth, 26(3), 239-252.

Thieblot, L., Roux, J., and Richet, P. (1998) High-temperature thermal expansion and decomposition of garnets. European Journal of Mineralogy, 10(1), 7.

Woodland, A.B., Angel, R.J., Koch, M., Kunz, M., and Miletich, R. (1999) Equations of state for $Fe_3^{2+}Fe_2^{3+}Si_3O_{12}$ "skiagite" garnet and Fe_2SiO_4-Fe_3O_4 spinel solid solutions. Journal of Geophysical Research-Solid Earth, 104(B9), 20049-20058.

6. Conclusions

Inclusions in diamonds represent the sole carrier of pristine samples from the Earth's mantle which can provide fundamental information on the physical and chemical environment of growth for diamond. This Ph.D thesis was focused on the experimental measurement of thermoelastic properties of synthetic phases analogous of mineral inclusions commonly occurring in diamonds. Knowledge of thermoelastic properties is a fundamental requirement for the application of the recently developed method of non-linear elasticity barometry (Angel et al.,2014a, 2015).

Elastic thermobarometry can be applied to any inclusions-host system, however, the diamond-inclusion system represents the ideal case and the starting point for the application of this method. The main advantages and simplifications which are obtained from the application of the elastic method at this system, are mainly related to: i) the extreme contrast between the thermo-elastic properties of the diamond compared to any inclusion, this difference is tied to the unique properties of diamond (very low compressibility and thermal expansion); ii) the thermoelastic parameters of diamonds have been widely analyzed in literature and are well known; iii) the thermoelastic parameters change with compositions for a single phase, while in the case of diamonds the composition can be considered fixed and therefore also the thermoelastic parameters, thus resulting in a reduction in the number of variables in the system; iv) for the application of this method in the natural samples, the diamonds are particularly optical transparent which allow to locate the inclusion from simple optical microscope analysis, and further, diamonds show an recognizable diffraction patterns which can be easily distinguished and separated from the diffraction pattern of the inclusions allowing to verify if the inclusion are correctly centered whit respect to the X-ray beam.

Main results of this thesis concern on one side the technical development of a new apparatus for the high-temperature in situ single crystal X-ray diffraction experiments (manuscript #1). The new resistance micro-furnace installed on Huber single-crystal diffractometer allows performing high temperature measurements while maintaining great thermal stability at the hot spot, where is located the sample, and preserving the micro-furnace from component melting. Combining this new diffractometer instrument with a new version of Single software (Angel and Finger, 2011) allows determining the individual unit-cell edges of good-quality single crystals to better than 1 part in 30 000, identical to that achieved for high-

pressure measurements. The same measurements protocol for both high-P and high-T experiments, that guarantees a coherent level of precision and accuracy, allows us for a reliable description of the HP-HT behavior of mineral phases by combining separated datasets in a unique thermal pressure EoS.

The first study (manuscript #2) on thermal expansion for minerals occurring as inclusions in diamonds has been carried out on two disordered pyroxene end-members: donpeacorite [DP N.1] $Mn_{0.54}Ca_{0.03}Mg_{1.43}Si_2O_6$ and bronzite [B22 N.60] $Fe_{0.54}Ca_{0.03}Mg_{1.43}Si_2O_6$. Dataset measured have been fitted with a Fei Equation of State (EoS) obtaining the following coefficients respectively: V_0 = 853.35(4) Å^3, $\boldsymbol{\alpha_{V,303K} = 2.31(24)610^{-5}\ K^{-1}}$ and V_0 = 845.40(6) Å^3, $\boldsymbol{\alpha_{V,303K} = 2.51(25)\times10^{-5}\ K^{-1}}$. While there is no difference in the volume thermal expansion coefficient as a function of composition and the expansion along the *b* direction is nearly identical for both samples, slight differences have been observed along *a* and *c* lattice directions, which reflect the response in difference expansion mechanisms above 1000 K. The negligible effect of the Fe-Mn substitution on the bulk thermal expansion simplifies the application to elastic geobarometry approach (e.g. Nestola et al., 2011; Howell et al., 2010; Angel et al., 2014a,b, 2015). In fact, though the compressibility effect is still not known, the nearly identical thermal expansion coefficients will not affect the entrapment pressure (Pe).

However, for the future applications, the different thermal anisotropy of these minerals at high temperature must be taken into account if we will able to measure the differential stresses occuring at depth in the Earth, while minerals are still forming.

The second part of the thesis (manuscripts #3,4) is focused on allumino-silicate garnets as they represent one of the main mineral inclusion occurring in diamonds (38% of the entire inclusions retrieved nowadays). We have determined the thermal expansion coefficients and compressibility behavior for grossular (ms. #3), almandine (ms. #4) and one synthetic aluminosilicate garnet with eclogitic composition ($Py_{51}Alm_{22}Gr_{27}$ ms in prep., see appendix I).

Furthermore, in manuscript number 4 we have considered that many xenolith samples record oxygen fugacity close to the Fe-Ni (O'Neill and Wood, 1979) which means that at pressure (i.e. depth) where diamond is stable in the cratonic lithosphere the surrounding environment is likely to have an fO_2 that is reducing enough so that carbon can exist as diamond (Stagno and Frost, 2010). Since oxygen fugacity strongly changes upon temperature variations (e.g. Frost, 1991) it is crucial to understand the oxygen reactivity while performing experiments with iron bearing samples as in the case of almandine. Our results clearly showed that no matter what the fO_2 conditions are, the thermal expansion of almandine does not change below 1100K.

The thermoelastic parameters were also obtained for a uvarovite sample using the same protocol adopted for the others allumino-silicate garnets end-members. The datasets were not included in any articles mainly because there have been problems related to the size of the sample that did not allow us to investigate the behavior of the sample up to the temperatures reached for the others end-members. However, our uvarovite dataset at high temperature (from 290 to 700 K) is the only one available obtained by single crystal X-ray diffraction experiments on pure synthetic uvarovite; no other work is available in literature; the combined high pressure, low temperature and high temperature datasets into a unique thermal-pressure EoS allowed us to retrieve the following parameters:

$$\mathbf{Uv_{100}}: V_0 = \mathbf{1729.96(7)}\ \text{Å}^3,\ K_0' = \mathbf{5.4(5)},\ \alpha = \mathbf{2.16(3)} * 10^{-5}\text{K}^{-1},\ T_E = 450(2)$$

The thermoelastic parameters used for the pyrope end-members were taken as reported by Milani et al. (2015):

$$\mathbf{Py_{100}}: V_0 = \mathbf{1506.15(16)}\ \text{Å}^3,\ K_0' = \mathbf{6.4(4)},\ \alpha = \mathbf{2.543(5)} * 10^{-5}\text{K}^{-1},\ T_E = 320$$

For a complete and detailed description and revision of thermoelastic parameters for diamonds which have been used within EoSFit7c for calculating the entrapment pressure see Angel et al. (2015), in which the following thermoelastic parameters are reported:

$$\mathbf{Dia}: V_0 = \mathbf{45.4094(45)}\ \text{Å}^3,\ K_0' = \mathbf{4.0},\ \alpha = \mathbf{0.2672(3)} * 10^{-5}\text{K}^{-1},\ T_E = 1500$$

The resulting thermal expansion coefficients and bulk moduli have been combined for each composition into a single pressure-volume-temperature equation of state that allowed us to compare the thermoelastic properties measured on the eclogitic garnet (Appendix I) with those calculated from the endmembers EoS. The resulting EoS coefficients are reported here below:

$$\mathbf{Py_{51}Alm_{22}Gr_{27}}: V_0 = \mathbf{1555.56(12)}\ \text{Å}^3,\ K_0' = \mathbf{5.7(5)},\ \alpha = \mathbf{2.32(1)} * 10^{-5}\text{K}^{-1},\ T_E = 420.8(1.2)$$

[measured]

$$\mathbf{Py_{51}Alm_{22}Gr_{27}}: V_0 = \mathbf{1554.90(24)}\ \text{Å}^3,\ K_0' = \mathbf{5.9(4)},\ \alpha = \mathbf{2.26(1)} * 10^{-5}\text{K}^{-1},\ T_E = 422$$

[calculated, see appendix. I]

The remarkable agreement between the calculated and measured thermoelastic coefficients will enable us to calculate EoS coefficients and in turn entrapment pressures for virtually any aluminosilicate garnet occurring in diamonds.

References

Angel, R.J., and Finger, L.W. (2011) SINGLE: a program to control single-crystal diffractometers. Journal of Applied Crystallography, 44(1), 247-251.

Angel RJ, Mazzucchelli M, Alvaro M, Nimis P, Nestola F (2014a) Geobarometry from host-inclusion systems: the role of elastic relaxation. Am Mineral 99, 2146-2149.

Angel, R.J., Gonzalez-Platas, J., Alvaro, M., (2014b). EosFit-7c and a Fortran module (library) for equation of state calculations. Zeit Kristall 229, 405-419.

Angel, R., Alvaro, M., Nestola, F., and Mazzucchelli, M. (2015) Diamond thermoelastic properties and implications for determining the pressure of formation of diamond-inclusion systems. Russian Geology and Geophysics, 56(1), 211-220.

Frost, B.R. (1991) Introduction to oxygen fugacity and its petrologic importance. Reviews in Mineralogy and Geochemistry, 25(1), 1-9

Howell D, Wood IG, Dobson DP, Jones AP, Nasdala L, Harris JW (2010) Quantifying strain birefringence halos around inclusions in diamond. Contrib Mineral Petrol 160, 705-717.

Nestola, F., Nimis, P., Ziberna, L., Longo, M., Marzoli, A., Harris, J.W., Manghnani, M.H., Fedortchouk, Y., (2011). First crystal-structure determination of olivine in diamond: Composition and implications for provenance in the Earth's mantle. Earth and Planetary Science Letters 305, 249-255.

O'Neill, H.S.C., and Wood, B. (1979) An experimental study of Fe-Mg partitioning between garnet and olivine and its calibration as a geothermometer. Contributions to Mineralogy and Petrology, 70(1), 59-70.

Stagno, V., and Frost, D.J. (2010) Carbon speciation in the asthenosphere: Experimental measurements of the redox conditions at which carbonate-bearing melts coexist with graphite or diamond in peridotite assemblages. Earth and Planetary Science Letters, 300(1), 72-84

Appendix I. Synthetic eclogitic garnet

Alluminosilicate garnet with an eclogitic composition has been synthesized by Vincenzo Stagno using a multi-anvil press at Bayerisches Geoinstitut. The chemical composition has been determined using a Jeol electron microprobe at the Bayerisches Geoinsitut to be $Py_{51}Al_{22}Gr_{27}$. One single crystal has been selected for the high-P and high-T experiments based on the crystalline and diffraction quality.

The high temperature X-ray diffraction experiments have been performed using a Huber diffractometer equipped with the micro-furnace described whose description and calibration are reported in chapter 2. The high pressure experiments have been carried out using a StoeStadi4 diffractometer equipped with point detector and an ETH-type diamond anvil cell (Miletich et al 2009)

The unit-cell edge has been determined by centering not less than 35 reflection for each temperature step, in the 2θ range of 14°-29° and χ range of 1°-90°.

The unit-cell volume increases linearly with temperature (Fig. 1) up to the maximum T reached in our experiments (1073 K).

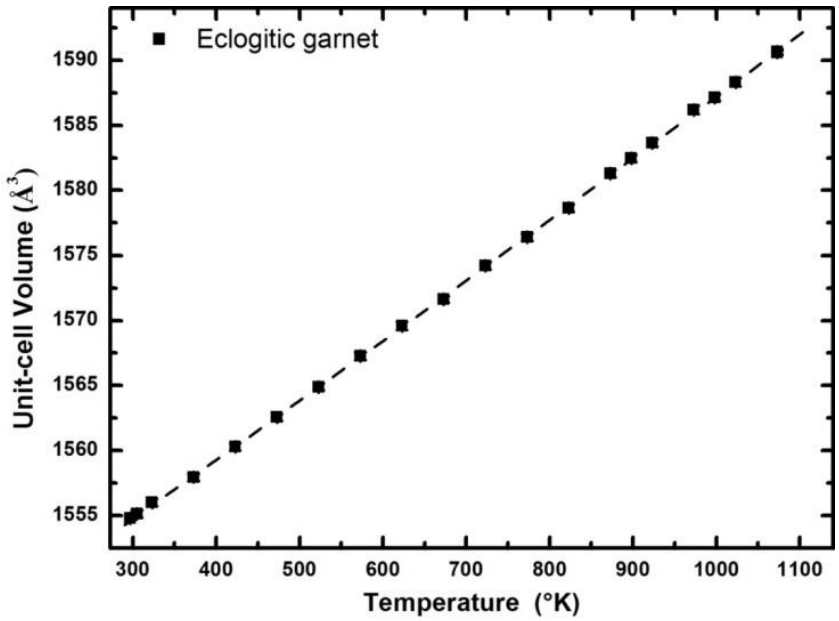

Fig. 1 Unit cell volume as a function of temperature for the synthetic garnet with eclogitic composition. The high temperature dataset has been fitted using a Kroll EoS (Kroll et al., 2012) using EosFit7c which allows us to refine also T_E.

Table 1. Unit-cell edge and volume synthetic eclogitic garnet different temperatures.

T(K)	*a*(Å)		V(Å^3)	
305	11.5857	(7)	1555.1	(3)
305	11.5857	(7)	1555.1	(3)
323	11.5879	(7)	1556.0	(3)
373	11.5927	(7)	1558.0	(3)
423	11.5985	(7)	1560.3	(3)
473	11.6041	(7)	1562.6	(3)
523	11.6099	(6)	1564.9	(3)
573	11.6157	(7)	1567.3	(3)
623	11.6215	(8)	1569.6	(3)
673	11.6265	(6)	1571.6	(3)
723	11.6329	(7)	1574.2	(3)
773	11.6383	(7)	1576.4	(3)
823	11.6438	(7)	1578.6	(3)
873	11.6503	(7)	1581.3	(3)
923	11.6561	(7)	1583.6	(3)
973	11.6623	(8)	1586.2	(3)
1023	11.6675	(8)	1588.3	(3)
1073	11.6731	(4)	1590.6	0.2
1073	11.6733	(5)	1590.7	0.2
998	11.6646	(6)	1587.1	(3)
898	11.6532	(7)	1582.5	(3)

Note: Standard deviations are given in parentheses.

References

Miletich, R., Cinato, D., and Johänntgen, S. (2009) An internally heated composite gasket for diamond-anvil cells using the pressure-chamber wall as the heating element. High Pressure Research, 29(2), 290-305.

Kroll, H., Kirfel, A., Heinemann, R., and Barbier, B. (2012) Volume thermal expansion and related thermophysical parameters in the Mg, Fe olivine solid-solution series. European Journal of Mineralogy, 24(6), 935-956.

Acknowledgments

This PhD thesis has been developed within the framework of the "INDIMEDEA" project funded by the ERC to F. Nestola and the SIR-MIU number RBSI140351 "MILE DEEp" granted to M. Alvaro.